NNT : NNNNNNNNNN

THÈSE DE DOCTORAT
DE
L'UNIVERSITÉ PARIS-SACLAY
PRÉPARÉE À
L'UNIVERSITÉ PARIS-SUD

ECOLE DOCTORALE N° 564
Physique de l'Ile-de-France

Spécialité de doctorat : Physique

Par

Mme. Olesia DMYTRUK

Quantum transport in a correlated nanostructure coupled to a microwave cavity

Thèse présentée et soutenue Orsay, le 17 Octobre 2016.

Composition du Jury :

M. AGUADO Ramón	Directeur de Recherche à Instituto de Ciencia de Materiales de Madrid	Rapporteur
M. HOUZET Manuel	Directeur de Recherche au CEA Grenoble	Rapporteur
Mme. BOUCHIAT Hélène	Directeur de Recherche au CNRS	Examinatrice
M. CAYSSOL Jérôme	Professeur à l'Université de Bordeaux	Examinateur
Mme. LE HUR Karyn	Directeur de Recherche au CNRS	Examinatrice
M. SIMON Pascal	Professeur à l'Université Paris-Sud	Directeur de thèse
M. TRIF Mircea	Professeur Assistant à l'Université de Tsinghua	Invité

université PARIS-SACLAY

ÉCOLE DOCTORALE
Physique en île-de-France (EDPIF)

Titre : Transport quantique dans une nanostructure corrélée, couplée à une cavité micro-ondes
Mots-clés : transport quantique, électrodynamique quantique des cavités, fermion de Majorana

Dans cette thèse, nous étudions d'un point de vue théorique les propriétés physiques de nanostructures couplées à des cavités micro-ondes. L'électrodynamique quantique (QED) en cavité en présence d'une boîte quantique s'est révélée être une technique expérimentale puissante, permettant d'étudier cette dernière par des mesures photoniques en plus des mesures de transport électronique conventionnelles. Dans cette thèse, nous proposons d'utiliser le champ micro-ondes de la cavité afin d'extraire des informations supplémentaires sur les propriétés des conducteurs quantiques : le coefficient de transmission optique est directement lié à la susceptibilité électronique de ces conducteurs quantiques. Nous appliquons ce cadre général à différents systèmes mésoscopiques couplés à une cavité supraconductrice micro-ondes comme une jonction tunnel, une boîte quantique couplée à des réservoirs, un fil topologique et un anneau supraconducteur. La QED en cavité peut être utilisée pour sonder, par l'intermédiaire de mesures photoniques, la dépendance en fréquence de l'admittance du puits quantique couplé à la cavité micro-ondes. En ce qui concerne le fil topologique, nous avons montré que la cavité permet de caractériser la transition de phase topologique, l'émergence de fermions de Majorana, ainsi que la parité de l'état fondamental. Pour l'anneau supraconducteur, nous étudions par l'intermédiaire de la réponse optique de la cavité l'effet Josephson et le passage à l'effet Josephson fractionnaire, qui est associé à l'apparition de fermions de Majorana dans le système. Le cadre théorique proposé dans cette permet de sonder de manière non-invasive un large éventail de nanostructures, des boîtes quantiques aux supraconducteurs topologiques. En outre, il donne de nouvelles informations sur les propriétés de ces conducteurs quantiques, informations non accessibles via des expériences de transport.

Title: Quantum Transport in a Correlated Nanostructure Coupled to a Microwave Cavity
Keywords: quantum transport, cavity QED, Majorana fermion

In this thesis, we study theoretically various physical properties of nanostructures that are coupled to microwave cavities. Cavity quantum electrodynamics (QED) with a quantum dot has been proven to be a powerful experimental technique that allows to study the latter by photonic measurements in addition to electronic transport measurements. In this thesis, we propose to use the cavity microwave field to extract additional information on the properties of quantum conductors: optical transmission coefficient gives direct access to electronic susceptibilities of these quantum conductors. We apply this general framework to different mesoscopic systems coupled to a superconducting microwave cavity, such as a tunnel junction, a quantum dot coupled to the leads, a topological wire and a superconducting ring. Cavity QED can be used to probe the finite frequency admittance of the quantum dot coupled to the microwave cavity via photonic measurements. Concerning the topological wire, we found that the cavity allows for determining the topological phase transition, the emergence of Majorana fermions, and also the parity of the ground state. For the superconducting ring, we propose to study the Josephson effect and the transition from the latter to the fractional Josephson effect, which is associated with the emergence of the Majorana fermions in the system, via the optical response of the cavity. The proposed framework allows to probe a broad range of nanostructures, including quantum dots and topological superconductors, in a non-invasive manner. Furthermore, it gives new information on the properties of these quantum conductors, which was not available in transport experiments.

CONTENTS

1

INTRODUCTION

Light-matter interaction is one of the fundamental physics phenomena that has seen a major research interest recently. Discovery of the photoelectric effect by Einstein and the breakthrough of quantum mechanics with its further rapid development considerably improved our understanding of light-matter interaction. This interaction is the cornerstone of the entire field of quantum electrodynamics (QED). At the most elementary level, the interaction between light and matter takes place when a single photon interacts with a single atom. Serge Haroche et.al. and David Wineland et.al. independently performed experiments on atom-photon coupling in their strive to prove quantum decoherence. Both of them were jointly awarded the Nobel Prize in Physics for "ground-breaking experimental methods that enable measuring and manipulation of individual quantum systems" related to these experiments. Haroche et.al. studied properties of photons trapped in a 3D cavity by sending Rydberg atoms through the cavity [78]. On the other hand, David Wineland et.al. used an opposite approach and studied trapped ions by sending photons through the cavity [54]. However, the main idea of these experiments remains the same: studying the interaction between a single atom, or an ion, and a photon. These experiments allowed to confirm quantum decoherence effects and demonstrated a possibility to create non-classical states of light. Also, Ref.[78] provides a first implementation of a qubit — a two-level system can be used as a building block for a quantum computer — that can be probed in atomic QED experiments. However, in these pioneering experiments, the coupling constant between the atom and cavity photons is fixed by the dipole moment of the atom, restricting the potential application area in quantum computing. Moreover, Rydberg atoms in a 3D cavity are not scalable to many-qubit architecture required for implementing quantum information protocols.

The idea of a tunable atom-cavity coupling constant as well as the need for implementing scalable qubits led to the theoretical proposal of circuit cavity QED. A real atom was

substituted with an arificial one and a 3D cavity was replaced by a 1D transmission line resonator to enable large coupling constant and ensure scalability. In [11], an artificial atom, or a two-level system, was proposed to be implemented as a Cooper pair box. It was achieved experimentally by the same authors in [101]. In circuit QED experiments, qubit-cavity coupling constant depends on the parameters of the superconducting circuit and the resonator, and the geometry of a 1D transmission line resonator allows for embedding many qubits in the cavity. Having multiple qubits implies entanglement, which is essential for implementing the quantum computing.

However, further progress in qubit implementation requires these qubits to be situated far away from each other and being highly tunable. This can be achieved in mesoscopic cavity QED [18] by using quantum dots as qubits. Quantum dots can be tuned by coupling them to gate electrodes. The electrons in quantum dots are not paired, allowing access to the electron spin. Also quantum dots can be tunnel coupled to leads and studied by transport measurement in addition to photonic probe in a microwave cavity.

Another direction for application of mesoscopic cavity QED is to use it to probe properties of the nanostructures embedded in microwave resonator. One of the systems that has been largely studied by transport measurements is a topological wire that can host Majorana fermions. Majorana fermions, which are particles that are their own antiparticles, have been first predicted by Ettore Majorana in 1937 as a real solution to Dirac equation. It was shown later that Majorana fermions can also appear in condensed matter physics, for example, in superconductors [49]. Due to its degenerate ground state and protection against local perturbation, Majorana fermions can be also used as qubits. In this thesis, we demonstrate that the methods of cavity QED can be used to probe Majorana fermions in topological superconductors coupled to a microwave cavity.

IN THIS THESIS

In this thesis, we apply the methods of cavity QED to study quantum conductors and topological wires coupled to a microwave cavity. We start with a theoretical description of the nanostructure-cavity coupling. Then we derive the cavity transmission in a weak

electron-photon coupling limit and its relation to the electronic susceptibility of the quantum conductor (see chapter 2). This susceptibility gives information about the nanostructure embedded in a microwave cavity. We apply cavity QED approach to study theoretically four specific mesoscopic conductors: a tunnel junction, a quantum dot coupled to the leads, a one-dimensional topological wire and a superconducting ring.

In chapter 4, we use the photonic response of the cavity to study a tunnel junction and a quantum dot tunnel coupled to metallic leads. We consider both capacitive coupling of the quantum dot to the cavity as well as coupling of the metallic leads to the cavity. We demonstrate that these two types of couplings result in a totally different cavity response and thus probe different observables associated with the quantum conductor. We find some relations between optical observables, such as the cavity transmission, and transport quantities, such as the differential conductance $\mathrm{d}I/\mathrm{d}V$. These relations are valid up to high frequency and voltage (therefore in the out-of-equilibrium regime) for quantum conductors far from resonance and hold only at low frequency and voltage for the quantum dot near resonance. Beyond these regimes, measurements of the cavity photonic field provide new information about the quantum conductor.

In chapter 5, we apply the cavity QED approach to find signatures of Majorana fermions in topological wires. We consider a p-wave superconductor capacitively coupled to a microwave cavity. The phase shift and frequency broadening due to the presence of the p-wave superconductor in the cavity are proportional to the electronic susceptibility of the wire. Photonic observables can be used to obtain signatures of the Majorana fermions, such as a topological phase transition and oscillations of the electronic susceptibility in the topological phase. Moreover, cavity QED experiments should allow to probe the parity of the Majorana state, which is not accessible in transport experiments.

In chapter 6, we study a topological wire that can host multiple Majorana fermions at its ends by coupling it to a microwave cavity. This situation is possible when there is long-range hopping in the wire. We demonstrate that the photonic field of the cavity allows to probe the topological phase transition between phases with different number of Majorana fermions as well as oscillations of the susceptibility. The period of the oscillations is dif-

ferent when there are two or one Majorana fermion at each end of the chain, while these oscillations are absent in the trivial phase.

In chapter 7, we apply methods of cavity QED to study the fractional Josephson effect associated with Majorana fermions physics. We consider a superconducting ring with a weak link threaded by a dc magnetic flux. An ac flux created by the microwave cavity induces the coupling between the ring and the cavity photonic field. We propose to study the Josephson effect and the transition from the latter to the fractional Josephson effect, which is associated with the emergence of the Majorana fermions in the system, via the response of the cavity. We take fully into account the interplay between the low-energy Majorana modes and the gaped bulks states, which we demonstrate is crucial for visualizing the evolution of the Josephson effect during the transition from the topological to the trivial phase.

2

CAVITY QUANTUM ELECTRODYNAMICS

In this chapter, we discuss the field of cavity quantum electrodynamics (QED). We start with atomic cavity QED that studies properties of atoms or ions coupled to discrete modes of the electromagnetic field [54, 78]. In [78] the interaction between a single photon and a single atom was observed by measuring the latter as it has passed through a 3D optical cavity. Also these experiments allowed to analyze decoherence effects as well as to demonstrate the implementation of quantum gates required for quantum computation. But atomic cavity QED with real atoms is characterized by a constant atom-cavity coupling and is not scalable to multiple qubits architecture. In order to overcome these constraints, a real atom was substituted with an artificial atom and a 3D cavity was substituted with a 1D transmission line resonator, which led to the development of circuit quantum electrodynamics [11, 101]. Circuit version of cavity quantum electrodynamics ensures tuning the coupling between an artificial atom and a superconducting resonator and implementing multiple qubits on a single chip, thus allowing for their entanglement and future application in solid-state quantum computation [45]. Moreover, in mesoscopic version of circuit QED connecting metallic leads to a mesoscopic conductor allows to study the latter by transport measurement in addition to optical probe. The combination of the different techniques allows to probe all properties of the mesoscopic system. Coupling closed systems to superconducting stripline resonators was first performed in [80] as a probe of the ac conductance related to the susceptibility. In section 2.4, we derive the relation between the transmission of the superconducting resonator and charge susceptibility of the electronic system embedded in the resonator.

2.1 FROM OPTICAL CAVITY TO TRANSMISSION LINE RESONATOR

2.1.1 *Single atom coupled to a single photon*

Interaction between light and matter at the level of coupling a single atom or ion to a single photon has been first experimentally studied in [54, 78]. In the first set of experiments[78], photons trapped in a cavity have been controled and measured by sending prepared atoms through the cavity. While in the second set of experiments [54], electrically charged atoms, or ions, have been measured and manipulated with light. These experiments are studying the same quantum systems such as a single atom and a single photon, but using opposite approaches. Coupling atoms with photons in a cavity allows to study entanglement of the combined system, and thus to scrutinize decoherence effects. Entanglement of qubits is also essential for implementation of quantum information protocols required for building a quantum computer in the future.

Atomic cavity quantum electrodynamics studies the properties of atoms coupled to the quantized electromagnetic modes in a cavity. In [78], Rydberg atoms are sent through the cavity in order to probe the properties of a photon trapped in this cavity. Rydberg atom is an excited atom with one or more electrons that has a large electric dipole moment d (due to the large separation between the electron and ion-core). That is why such atoms have a large response to an electric field and consequently are suitable for studying light-atom interaction. The cavity in these experiments is an open Fabry-Perot resonator, made of two mirrors. The geometry of such resonator allows to apply an electric field along the cavity axis.

A two-level atom could be used as a qubit with two states $|0\rangle$ and $|1\rangle$. It allows to perform logic operations required for implementing quantum information protocols. When the state of the atom-cavity system changes from $|0, e\rangle$, in which the atom is in the excited state and there is no photon in the cavity to $|1, g\rangle$, in which the atom is in the ground state and there is one photon in the cavity, the phase of the atom changes. The photonic field is coupled to Rydberg atom by dipole interaction. Measurement of the state of the atom after it has passed through the cavity allows to obtain information about the properties of

the photon trapped inside the cavity. Two-level systems, such as Rydberg atoms, coupled to the photonic modes of the cavity can be described by Jaynes-Cummings Hamiltonian

$$H = \hbar\omega_{eg}\sigma_z + \hbar\omega_c\left(a^\dagger a + 1/2\right) + \hbar g\left(a^\dagger\sigma_- + a\sigma_+\right), \tag{2.1}$$

where ω_{eg} is the transition frequency between the excited and ground state of the atom, ω_c is the cavity frequency, which in resonant cavity is tuned to be equal to ω_{eg}, g denotes the atom-photonic field coupling constant, σ_z, σ_+ and σ_- are the Pauli matrices of the atomic pseudospin, $a(a^\dagger)$ is the photon annihilation (creation) operator. The coupling constant $g = \epsilon_{rms}d/\hbar$, where ϵ_{rms} is the root mean square (r.m.s.) vacuum field at the cavity center and d is the dipole matrix element for the excited to ground state transition in the atom. The dipole moment of the atom is fixed for a given atom, that is why the atom-photon coupling cannot be tuned in cavity QED with nature-given atoms.

It was shown [78] that Rydberg atoms, coupled to a superconducting cavity containing a few photons, could be used to test quantum decoherence and realize quantum logic operations necessary for building a quantum computer.

Though Ref.[78] were the first experiments to demonstrate the atom-photon interaction and implementation of qubits based on two-level atoms, further refinements of the setup were required. In cavity QED with real atoms, the coupling between an atom and a photon is fixed by the dipole moment of the atom, as well as the resonant cavity frequency is fixed by the transition frequency between excited and ground states of the atom. Moreover, nature-given atoms coupled to a 3D cavity are not scalable to many qubit setups required for implementation of quantum computer.

2.1.2 *Cavity QED with superconducting circuits*

Realization of cavity QED that allows to overcome the fixed atom-photon coupling and scalability issues using superconducting circuits has been proposed in [11]. In this theoretical proposal, the cavity is implemented as a 1D transmission line resonator consisting of a full-wave section of superconducting coplanar waveguide and an atom is implemented

as a superconducting qubit, or more precisely a Cooper pair box. Scheme of the proposed implementation of cavity QED based on transmission line resonator is presented in Fig.2.1. Already at that time, lithographic technique allowed to create a Cooper pair box coupled to a 1D transmission line resonator on a single solid-state chip. Cooper pair box, which is a mesoscopic superconducting island which is coupled via two Josephson tunnel junctions to a superconducting reservoir, plays a role of a qubit in this proposal. In the proposed geometry, this qubit can be isolated from the electromagnetic environment in controllable manner thus being suitable for solid-state quantum computing. Since in this case the cavity is a 1D transmission line resonator, and not a 3D cavity as in [78], the zeropoint energy ϵ_{rms} is distributed over a very small effective volume ($< 10^{-5}$ cubic wavelengths) leading to large rms voltage $V_{rms} \approx \sqrt{\frac{\hbar\omega_c}{cL}}$ between the center conductor and the adjacent ground plane at the antinodal positions, where L is the length of the resonator and c is the capacitance per unit length of the transmission line. Resonant frequency of the transmission line resonator is determined by a fixed geometry thus allowing to perform reproducable experiments. Also, the artificial atom could be controled by external fields, for example, by threading a flux Φ_{ext} in the loop formed by the pair of junctions and changing the gate voltage V_g (see Fig.2.1). By tuning the capacitance and the Josephson energy of the superconducting circuit, one can obtain an effective two-level system, similar to Rydberg atom studied in [78]. Moreover, it was demonstrated that such a two-level system could be described by the Jaynes-Cummings Hamiltonian [11] with the atom-cavity coupling constant $g = \frac{eC_g}{\hbar(C_g + C_J)} V_{rms}$, where C_g is the the capacitance between the center conductor of the resonator and the Cooper pair box and C_J is capacitance of the Josephson junction. Considering the cavity resonance frequency $\omega_c = 10$ GHz leads to the coupling constant $g \approx 100$ MHz, which is three orders of magnitude larger than in atomic cavity QED experiments with Rydberg atoms. Moreover, the position of the Cooper pair box in transmission line resonator is fixed thus ensuring that the coupling constant g does not depend on position of the atom as in 3D cavities with Rydberg atoms. Thus, cavity QED with superconducting circuits should allow to reach easily the strong-coupling limit (the coupling between the qubit and the cavity is larger than both the damping rates of the qubit and the cavity). As for the practical application, two

or more qubits can be placed along the length of the transmission line resonator. In case of two qubits, they can be separated by the length of the resonator $\propto$ 1cm and tuned by capacitive coupling to the left and right center conductors of the transmission line. Thus, a 1D transmission line resonator allows for entanglement of qubits, making it a suitable platform for quantum computation.

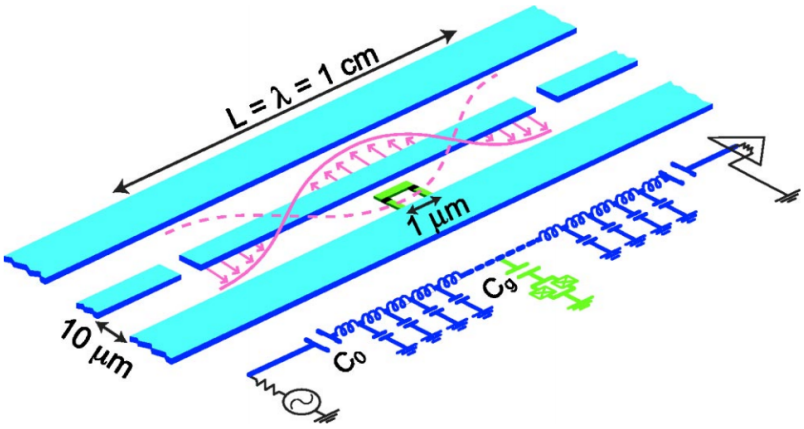

Figure 2.1: Scheme and equivalent lumped circuit representation of implementation of cavity QED using superconducting circuits. The 1D transmission line resonator consists of a full-wave section of superconducting coplanar waveguide. A Cooper-pair box qubit is placed between the superconducting lines and is capacitively coupled to the center conductor at a maximum of the voltage standing wave, yielding a strong electric dipole interaction between the qubit and a single photon in the cavity. The Cooper pair box consists of two small Josephson junctions, configured in a loop to permit tuning of the effective Josephson energy by an external flux Φ_{ext}. Input and output signals are coupled to the resonator, via the capacitive gaps in the center conductor, from transmission lines which allow measurements of the amplitude and phase of the cavity transmission. Reproduced from [11].

The theoretical proposal [11] of a 1D transmission line resonator with an artificial atom has been experimentally implemented by the same authors in [101]. This work [101] also demonstrates the first experimental observation of a strong coupling between a two-level system and a single photon in a cavity. A two-level system in this experiment has been implemented as a Cooper pair box as was suggested in [11], since its dipole moment is at least one order of magnitude larger than in Rydberg atoms [78]. As for the transmission line resonator that consists of a narrow center conductor and two nearby lateral ground

planes (see Fig.2.3), it provides a large electric field between the center conductor and the ground plane which is hundred times larger than in 3D microwave resonators. Combination of large dipole moment and the large vacuum field strength ensures the possibility of entering a strong-coupling limit in superconducting circuit QED. The resonator is coupled to the transmission lines (see Fig.2.3, b) thus allowing to probe the phase and the amplitude of the microwave probe beam transmitted through the resonator. The transmission of the cavity is changed due to the presence of the Cooper pair box inside the cavity. Thus, the properties of the qubit can be obtained by performing photonic measurements of the cavity.

But superconducting stripline resonators were first coupled to isolated mesoscopic systems such as sets of isolated rings [80] as a probe to investigate the susceptibility of these systems without any connection to an invasive probe. The magnetic susceptibility of the rings $\chi(\omega)$ is connected to ac conductance $Y(\omega)$ as $\chi(\omega) \approx i\omega Y(\omega)$. The measure of the modification of the resonance frequency f_n and the quality factor Q_n due to the presence of the rings in the superconducting resonator gives access to the complex ac conductance of the rings [27, 28, 80]

$$\frac{\delta f_n}{f_n} \propto \Im\left[Y(f_n)\right], \qquad \delta\left(\frac{\delta Q_n}{Q_n^2}\right) \propto Re\left[Y(f_n)\right]. \tag{2.2}$$

Though this experiment [80] was performed in closed system and in the classical regime, it was a first demonstration that properties of the electronic systems can be obtained by non-invasive measurements by coupling them to superconducting resonators. Later on, this technique was used to obtain the conductance of the non-connected Aharonov-Bohm rings [28] and silver rings [27], as well as the susceptibility of the SNS junctions [26, 37]. We compare the electronic susceptibility of the ring obtained by the classical approach and the quantum one in chapter 7.

Pioneering theoretical proposal of mesoscopic cavity QED with quantum dots instead of superconducting qubits has been reported in [18]. This proposal is based on capacitive coupling between the electron charge of the quantum dot and a superconducting transmission line resonator. Compared to cavity QED with superconducting qubits, cav-

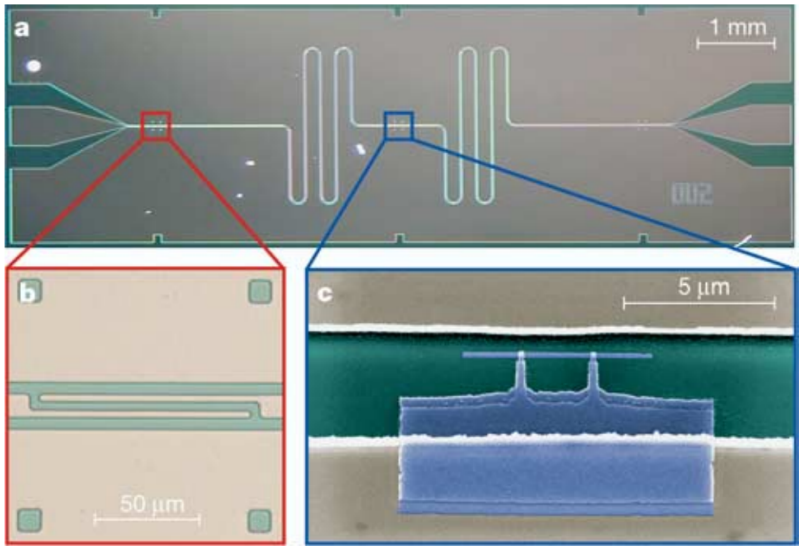

Figure 2.2: Integrated circuit for cavity QED. a) The superconducting niobium coplanar waveguide resonator is fabricated on chip using optical lithography. The stripline resonator consists of the center conductor and two lateral ground planes. The meandering resonator is coupled by a capacitor at each end of the resonator (see b) to an input and output feed line, fanning out to the edge of the chip and keeping the impedance constant. b) The capacitive coupling to the input and output lines and hence the coupled quality factor Q is controlled by adjusting the length and separation of the finger capacitors formed in the center conductor. c) False color electron micrograph of a Cooper pair box (blue) fabricated onto the silicon substrate (green) into the gap between the center conductor (top) and the ground plane (bottom) of a resonator (beige). The Josephson tunnel junctions are formed at the overlap between the long thin island parallel to the center conductor and the fingers extending from the much larger reservoir coupled to the ground plane. Reproduced from [101].

ity QED with quantum dots allows for strong coupling between distant quantum dots and thus for implementing a scalable quantum computer. Also quantum dots are highly tunable and give access to the electron spin. Since quantum dots can be tunnel coupled to metallic leads, mesoscopic cavity QED allows to study the properties of the quantum dots by electronic transport measurements in addition to photonic measurements.

Later on, it was demonstrated that for open mesoscopic conductors, such as quantum dots, the transmission coefficient at energy near the cavity frequency is sensitive to the charge susceptibility of the quantum dot circuit [24].

2.2 COUPLING A QUANTUM DOT TO A MICROWAVE CAVITY

Quantum dots are nanoscopic systems that emulate atoms by showing discrete energy levels and atomiclike electronic filling shell structure. Thus, they could be measured by optical means. But contrary to atoms, quantum dots can be coupled to metallic leads and probed in electronic transport experiments similarly to large metallic conductors [18]. By embedding quantum dots in superconducting transmission line resonators, it is possible to study quantum dots by photonic measurements in addition to electronic transport. Some recent experiments probed and manipulated a single or double quantum dot with resonators [6, 13, 29, 31, 40, 41, 72, 90, 93, 95, 102]. Theoretical study of the quantum dots coupled to transmission line resonators have been performed in [9, 18, 23, 24, 87], and we discuss it in the next section.

One of the pioneering experiments, in which a quantum dot has been coupled to a single mode of electromagnetic field in a superconducting resonator, has been reported in [29]. In this experiment, a single wall carbon nanotube is embedded in the coplanar waveguide resonator (see Fig.2.3) in order to implement a single quantum dot coupled to a cavity situation. A new aspect of this experiment is that there are two wires, source and drain, that go inside the cavity in order to drive a dc current through the quantum dot. This allows to measure a differential conductance dI/dV of the quantum dot while changing the source-drain voltage V_{sd}, which is a quantity typically measured in transport experiments. The quantum dot is also connected to gate electrodes that allows to change the position of the energy level inside the quantum dot by varying the gate voltage V_g. At the same time, a continuous microwave signal is transmitted through the cavity. The signal is sent through one side of the cavity and measured at the other one, thus allowing to measure the cavity transmission. The variation of the phase and the amplitude of the microwave signal is due to the presence of the quantum dot circuit inside the cavity. The differential conductance dI/dV of the quantum dot tunnel coupled to metallic leads as a function of the source-drain V_{sd} and gate V_g that has been measured in [29] and is presented in Fig.2.4, a). Coulomb diamonds as well as the Kondo ridge at zero bias associated with the Kondo effect have been observed. The variation of the phase $\delta\phi$ of the microwave

signal transmitted through the cavity near the cavity resonance frequency $f = 4.976$ GHz for the same parameters is presented in Fig.2.4, b). Comparing the differential conductance dI/dV and the phase shift $\delta\phi$ as a function of the source-drain bias V_{sd} over the Kondo ridge (see Fig.2.4,c), we can see these two quantities look very similar. Thus, this experiment demonstrated that photonic observable, such as the phase shift $\delta\phi$, gives access to the properties of the quantum dot obtained by measuring the transport quantity, such as dI/dV. However, the explanation why the phase shift and the differential conductance have a similar behaviour as a function of voltage bias was not given. Also, in this work [29] the value of the electron-photon coupling λ for carbon nanotube constant has been measured and is equal to 140 MHz. We use this estimate for the coupling constant when giving quantitative estimate of the phase shift in chapter 5.

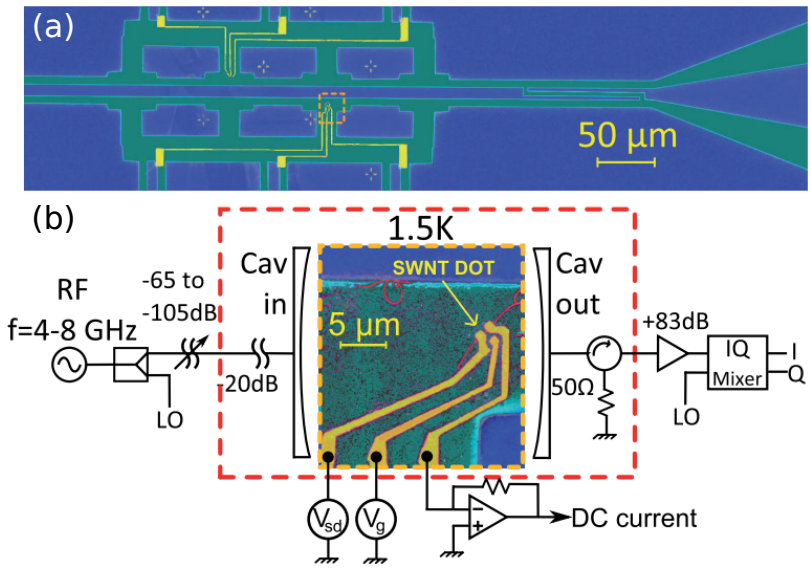

Figure 2.3: (a) Scanning electron microscope (SEM) picture in false colors of the coplanar waveguide resonator. Both the typical coupling capacitance geometry of one port of the resonator and the 3-terminals geometry are visible. (b) False colors SEM picture of a single wall carbon nanotube dot inside an on-chip cavity embedded in a schematics of the measurement setup. Reproduced from [29].

Mesoscopic cavity QED has been proven to be a powerful measurement technique that allows to detect extremely small variations of the phase of the signal transmitted through

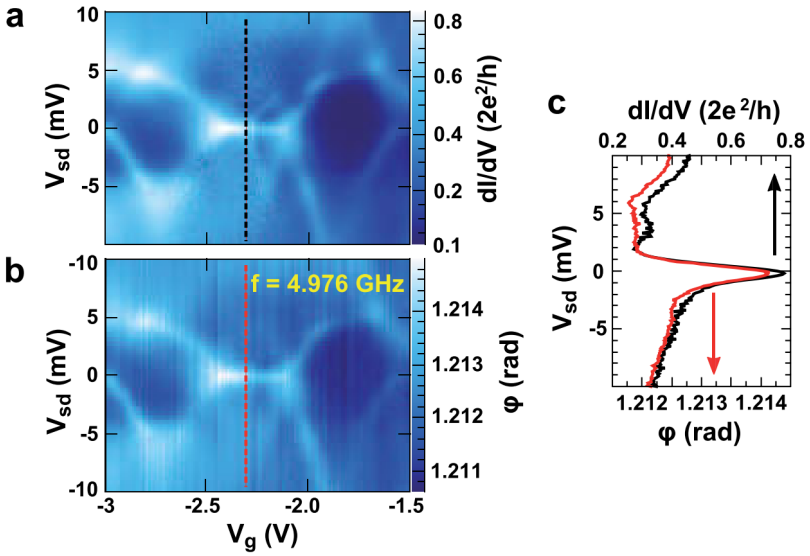

Figure 2.4: (a) Color scale plot of the differential conductance in units of $2e^2/h$ measured along three charge states exhibiting the conventional transport spectroscopy. A Kondo ridge is visible at zero bias. (b) Color scale plot of the phase of the microwave signal at resonance frequency $f = 4.976$ GHz, measured simultaneously with the differential conductance. (c) Differential conductance (black line) and phase of the transmitted microwave signal (red line) at the resonance frequency$f = 4.976$ GHz as a function of source-drain bias V_{sd} over a Kondo ridge in between two Coulomb peaks. Reproduced from [29].

the cavity (up to $\delta\phi \propto 10^{-3}$) [29]. The recent progress in engineering superconducting cavities makes it possible to implement on-chip mesoscopic circuits coupled to high finesse resonators [84]. Thus, properties of different mesoscopic systems can be studied by coupling them to a cavity. Cavity QED with a quantum dot has been extended to experimental study of interaction between two distant quantum dots [30, 32], spin-photon coupling [99] and Kondo physics [31]. On the theory side, mesoscopic QED has been used to investigate tunnel junctions [36, 61] and quantum point contacts [62], as well as Majorana fermions in topological superconductors (see chapter 3). Also nonlocal electronic transport through two quantum dots coupled to a microwave cavity was studied in [10, 21, 51].

2.3 ELECTRON-PHOTON COUPLING IN CAVITY QED

In this section, we discuss how to describe theoretically the coupling between the quantum conductor (for example, a quantum dot tunnel coupled to metallic leads) and photonic field inside the cavity. For simplicity, we consider a single mode of a microwave cavity field, but this description can be generalized to multimode cavity by introducing a sum over all cavity modes. The detailed derivation using photonic pseudopotential to account for electric coupling between electrons in a nanostructure and cavity photons has been recently done in [23]. Here we demonstrate how to obtain the capacitive coupling between the quantum conductor and photonic field inside the cavity. In a continuum description, we can describe the interaction between the electrons in the nanostructure and the electromagnetic field via the minimal coupling, i.e., $p \to p - eA$ in the electronic Hamiltonian, where A is the electromagnetic field vector potential and p is the momentum of the electrons.

The combined Hamiltonian that describes the electronic system and cavity photons can be written as

$$H_{tot} = \int d^3r \psi^\dagger(\vec{r}) h(\vec{r}) \psi(\vec{r}) + \hbar\omega_c a^\dagger a \quad \text{with} \quad h(\vec{r}) = \frac{1}{2m}\left(-i\hbar\nabla_{\vec{r}} + e\hat{A}(\vec{r})\right)^2, \quad (2.3)$$

where $\psi(\vec{r})$ is the field operator, $a(a^\dagger)$ is photon annihilation (creation) operator and $h(\vec{r})$ is a single-electron Hamiltonian that includes coupling to the electromagnetic field with

$$\hat{A}(\vec{r}) = A(\vec{r}) i \left(a - a^\dagger\right) \quad (2.4)$$

being a photonic vector potential. $\hbar\omega_c a^\dagger a$ describes a single-mode electromagnetic field with frequency ω_c. $e > 0$ is elementary charge.

The electron-photon coupling in Eq.2.3 contains creation or annihilation of one photon as well as two photons transitions via $\hat{A}^2$ term. In order to eliminate two-photon processes

in Hamiltonian Eq.2.3, let us perform a unitary transformation. But let us first introduce a photonic pseudopotential that account for possible spatial variations of $A(\vec{r})$

$$V_\perp(\vec{r}) = \omega_c \int_{C(\vec{r},\vec{r}_0)} A(\vec{r}')d\vec{l}, \tag{2.5}$$

where $C(\vec{r},\vec{r}_0)$ is a continuous functional path inside the circuit relating a reference point $\vec{r}_0$ and any point $\vec{r}$. After performing a unitary transformation

$$\tilde{H}_{tot} = U^\dagger H_{tot} U \qquad \text{with} \qquad U = \exp\left[\frac{e\left(a - a^\dagger\right)}{\hbar\omega_c}\int d^3r V_\perp(\vec{r})\psi^\dagger(\vec{r})\psi(\vec{r})\right], \tag{2.6}$$

the combined Hamiltonian of the electron-photon system Eq.2.3 becomes

$$\tilde{H}_{tot} = \int d^3r \psi^\dagger(\vec{r})\tilde{h}(\vec{r})\psi(\vec{r}) + \hbar\omega_c a^\dagger a + V\left(a + a^\dagger\right) + V^2/\hbar\omega_c, \tag{2.7}$$

where

$$V = -e\int d^3r V_\perp(\vec{r})\psi^\dagger(\vec{r})\psi(\vec{r}) \qquad \text{and} \qquad \tilde{h}(\vec{r}) = -\frac{\hbar^2}{2m}\Delta_{\vec{r}}. \tag{2.8}$$

Now the electron-photon coupling is included in $\tilde{H}_{tot}$ only by $V\left(a + a^\dagger\right)$ term, which is a single-photon process. When the spacial dependence of the photonic vector potential $A(\vec{r}) \equiv A_0$ can be disregarded, the photonic vector potential $V_\perp(\vec{r}) = \omega_c A_0 \vec{r}$ with $A_0 = E_0/\omega_c$.

In the following, we use the second-quantized formalism to describe an electronic system coupled to photonic field in the cavity. As an example of the electronic system, let us consider a quantum dot tunnel coupled to metallic leads. In the absence of the cavity, the electronic Hamiltonian can be written as

$$H_{el} = \sum_{o,j} \epsilon_{oj} c^{\dagger}_{oj} c_{oj} + \sum_{o,j \neq o',j'} \left(t_{oj,o'j'} c^{\dagger}_{oj} c_{o'j'} + h.c. \right), \tag{2.9}$$

where $c_{oj}(c^{\dagger}_{oj})$ is the electron annihilation (creation) operator with $o = d, l_1, l_2$ corresponding to the quantum dot and metallic leads, respectively. j accounts for orbitals in the dot or the leads. ϵ_{oj} is the energy of the quantum dot ($o = d$) or the leads ($o = l_1, l_2$) that corresponds to wavefunction $\phi_{oj}(\vec{r})$. In order to make the connection with Eq.2.7, let us write the field operator as

$$\psi(\vec{r}) = \sum_{o,j} \phi_{oj}(\vec{r}) c_{oj}. \tag{2.10}$$

In second-quantized description Eq.2.7 reads

$$H^{QD}_{tot} = H_{el} + \hbar\omega_c a^{\dagger} a + h_{int} \left(a + a^{\dagger} \right), \tag{2.11}$$

where the electron-photon Hamiltonian has the form

$$h_{int} = \sum_{o,j} \alpha_{oj} c^{\dagger}_{oj} c_{oj} + \sum_{o,j \neq o',j'} \left(\gamma_{oj,o'j'} c^{\dagger}_{oj} c_{o'j'} + h.c. \right) \tag{2.12}$$

where we have neglected the terms $V^2/\hbar\omega_c$. Using Eq.2.8 we can find the electron-photon couplings α_{oj} and $\gamma_{oj,o'j'}$.

$$\alpha_{oj} = -e \int d^3 r V_{\perp}(\vec{r}) \left| \phi_{oj}(\vec{r}) \right|^2 \tag{2.13}$$

acts as to shift the energy ϵ_{oj}. And

$$\gamma_{oj,o'j'} = -e \int d^3r V_\perp(\vec{r}) \phi^*_{oj}(\vec{r}) \phi_{o'j'}(\vec{r}) \qquad \text{with} \qquad oj \neq o'j' \tag{2.14}$$

accounts for photon-induced tunneling coupling between the dot and the leads.

If photonic vector potential varies slowly inside the quantum conductor $V_\perp(\vec{r}) = const$, then $\gamma_{oj,o'j'} \equiv 0$ since the wavefunctions with $oj \neq o'j'$ are orthogonal. And we are only left with capacitive coupling between the quantum dot (and metallic leads) and the cavity central conductor.

In most of the papers [24, 87], the coupling between the quantum dot circuit and the cavity is described as the capacitive coupling between number of electrons in the dot and the photonic field

$$H_{el-ph} = \alpha d^\dagger d(a + a^\dagger), \tag{2.15}$$

where $d(d^\dagger)$ is the electron annihilation (creation) in the quantum dot. While the coupling between the metallic leads and the cavity is disregarded. It could be done assuming that the leads-cavity coupling is symmetric, in which case it just shifts the dot-cavity coupling constant. In chapter 4 of this thesis, we consider fully the coupling between the metallic leads and a microwave cavity.

The derivation for the electron-photon coupling for topological superconductor discussed in chapter 5 is presented in appendix C.1.

2.4 INPUT-OUTPUT THEORY FOR MICROWAVE CAVITIES

In this section, we present details on the input-output theory for the cavity in the presence of the coupling to a quantum conductor (tunnel junction, quantum dot, topological wire, etc.). We demonstrate that the transmission of the cavity depends on the charge susceptibility of the electronic system. We concentrate on only single resonance of the cavity with frequency ω_c [20] and, for simplicity, we assume for the moment a single-sided cavity

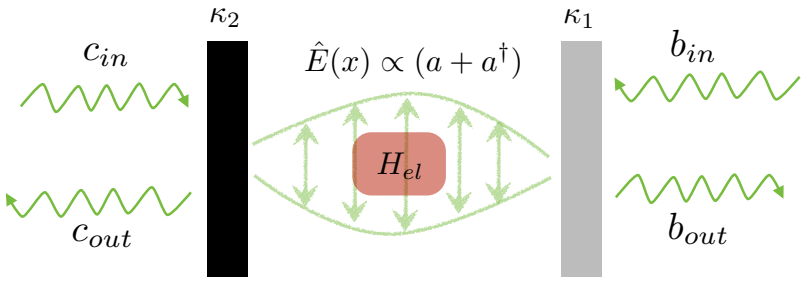

Figure 2.5: Sketch of a cavity system. The input fields b_{in} and c_{in} are sent from the right and left mirrors, respectively, towards the cavity, and an output fields b_{out} and c_{out} are collected on the same sides. The cavity field, which is quantified by the bosonic operators a and $a^\dagger$, interacts with the electronic system via capacitive coupling, affecting the cavity. The coupling between the cavity field and the external modes is quantified by the decay rate $\kappa_{1(2)} = 2\pi\rho|f_{1(2)}|^2$, with ρ the bath density of states and $|f_{1(2)}|^2 \equiv f_{1(2)} f^*_{1(2)}$ being the average coupling between the cavity and the bath modes on the right (left). In the first part, for simplicity, we assume that $\kappa_2 = 0$, which corresponds to a one-side cavity.

(for more details see appendix A). The total Hamiltonian describing the system reads [34, 36]

$$H = H_b + H_{c-b} + \underbrace{H_{el} + H_c + H_{el-c}}_{H_{sys}}. \tag{2.16}$$

The bath Hamiltonian is

$$H_b = \sum_q \omega_q b_q^\dagger b_q, \tag{2.17}$$

where b_q ($b_q^\dagger$) are the annihilation (creation) operators for the bath modes with energy ω_q, with q labeling their quantum numbers. The cavity Hamiltonian is

$$H_c = \omega_c a^\dagger a, \tag{2.18}$$

where a ($a^\dagger$) is the annihilation (creation) operator for the cavity mode with energy ω_c. The cavity-bath Hamiltonian is

$$H_{c-b} = -i \sum_q \left(f_q a^\dagger b_q - f_q^* b_q^\dagger a \right), \tag{2.19}$$

where the complex coefficients f_q are coupling parameters between the cavity and the external bath. The electron-cavity Hamiltonian is

$$H_{el-c} = \alpha(a + a^\dagger)n, \tag{2.20}$$

where α is the coupling strength between the cavity field and the total number operator in the system $n \equiv \sum_{j=1}^{N} c_j^\dagger c_j$, with c_j ($c_j^\dagger$) being the annihilation (creation) operator for the electrons (fermionic degrees of freedom) at site j in the electronic system. And H_{el} is the electronic Hamiltonian only.

The idea of the input-output theory is to find the output photons (or field) in terms of the input ones, as shown schematically in Fig. 2.5. Following Ref. [20], we obtain for the cavity equation of motion for a one-side cavity ($\kappa_2 = 0$ in Fig. 2.5):

$$\dot{a} = i\,[H_{sys}, a] - \frac{\kappa}{2} a - \sqrt{\kappa} b_{in}\,, \tag{2.21}$$

for the input field, and

$$\dot{a} = i\,[H_{sys}, a] + \frac{\kappa}{2} a - \sqrt{\kappa} b_{out}\,, \tag{2.22}$$

for the output field, where $\kappa = 2\pi\rho|f|^2$ is the cavity decay rate, with ρ the bath density of states and f being the average coupling between the cavity and the bath modes. Subtracting Eq. (A.22) from Eq. (A.19) we obtain that

$$b_{out}(t) = b_{in}(t) + \sqrt{\kappa} a(t), \tag{2.23}$$

a result which holds for any general cavity Hamiltonian.

In the following, we establish the relationship between b_{out} and b_{in} in the presence of the electronic system, as depicted in Fig. 2.5. For that, we first evaluate the commutator:

$$[H_{sys}, a] = -\omega_c a - \alpha n\,, \tag{2.24}$$

where n is the time-dependent electronic particle number (see below). In order to utilize this contribution to the equation of motion of the cavity field, we need to evaluate the time-dependent particle number $n(t)$, which itself depends on the coupling to the cavity. We can represent $n_H(t)$ in the Heisenberg picture as follows:

$$n_H(t) = U^\dagger(t, t_0) n_I(t) U(t, t_0), \tag{2.25}$$

where

$$U(t, t_0) = T_c \exp\left(-i \int_{t_0}^{t} dt' H_{el-c}(t')\right) \tag{2.26}$$

is the evolution operator with T_c the time-ordering operator that puts operators with later times to the left of the ones with earlier times. We can then write Eq.(2.25) in the following way

$$n_H(t) \approx n_I(t) + i\alpha \int_{t_0}^{t} dt' \left[(a + a^\dagger) n_I(t'), n_I(t)\right], \tag{2.27}$$

up to leading order in the coupling constant α. Thus, the time-evolution of the electronic particle number contains, besides the electronic component, a contribution that arises because of the coupling to the cavity. Introducing Eq. (2.27) into Eq. (2.24) and assuming $t_0 \to -\infty$ we obtain:

$$\begin{aligned}[H_{sys}, a] &= -\omega_c a - \alpha n_I(t) \\ &- i\alpha^2 \int_{-\infty}^{t} dt' \left[\left(a(t) e^{-i\omega_c(t'-t)} + a^\dagger(t) e^{i\omega_c(t'-t)}\right) n_I(t'), n_I(t)\right],\end{aligned} \tag{2.28}$$

where $a(t) \approx ae^{-i\omega_c t}$ and $a^\dagger(t) \approx a^\dagger e^{i\omega_c t}$ in zeroth order in α (because the expression is already multiplied by α^2 we can utilize the bare time dependence in this expression). In the following, we switch to the Fourier space in order to solve the equation for $a(t)$, and take into account all contributions that affect its time-dependence, namely the external modes too. We obtain:

$$-i\omega a(\omega) = -i\omega_c a(\omega) - \frac{\kappa}{2}a(\omega) - \sqrt{\kappa}b_{in}(\omega) - i\alpha n_I(\omega)$$
$$+\alpha^2 \int_{-\infty}^{\infty} dt e^{i\omega t} \int_{-\infty}^{t} dt' \Big[\Big(a(t)e^{-i\omega_c(t'-t)} + a^\dagger(t)e^{i\omega_c(t'-t)}\Big) n_I(t'), n_I(t)\Big]. \quad (2.29)$$

Before continuing with the derivation, let us describe each term in the above expression. The first term describes the free cavity evolution, the second term the leaking into the continuum of modes (the external bath) at rate $\kappa/2$, the third term is the input field supplied from the right side, the fourth term correspond to another "input" contribution to the cavity from the electronic system (a noise term), while the last term leads to both a shift in the cavity frequency as well as to frequency broadening. We can now average over the electronic system. Moreover, we can neglect the highly oscillating term $a^\dagger(t) \propto e^{i\omega_c t}$, namely we perform the so called Rotating Wave Approximation (RWA). Under all these assumptions, the last term in Eq. (2.29) becomes:

$$\alpha^2 \int_{-\infty}^{\infty} dt e^{i\omega t} \int_{-\infty}^{t} dt' a(t) e^{-i\omega_c(t'-t)} \langle [n_I(t'), n_I(t)] \rangle_0$$
$$= -ia(\omega)\Pi(\omega_c), \quad (2.30)$$

where

$$\Pi(t-t') = -i\theta(t-t')\alpha^2 \langle [n_I(t), n_I(t')] \rangle_0 , \quad (2.31)$$

is the retarded density-density electronic correlation function or electronic susceptibility, and $\langle \dots \rangle_0$ means the expectation value of the unperturbed electronic system. Note that

for deriving the above expression, we assumed that the electronic system is in a stationary state and thus time translational invariant.

We are now in position to find the cavity field $a(t)$ and the output field $b_{out}(t)$ in terms of the input field $b_{in}(t)$. Introducing Eq. (2.30) into Eq. (2.29) we obtain

$$a(\omega) = -\frac{\sqrt{\kappa} b_{in}(\omega) + i\alpha\langle n_I(\omega)\rangle_0}{-i(\omega-\omega_c) + \kappa/2 + i\Pi(\omega_c)}\,. \tag{2.32}$$

We thus have two contributions to the cavity field: the external input and the input from the electronic system. Our aim is to relate in fact the output and input fields, which can be done easily via the expression in Eq. (2.23):

$$b_{out}(\omega) = \frac{[-i(\omega-\omega_c) - \kappa/2 + i\Pi(\omega_c)]b_{in}(\omega) - i\sqrt{\kappa}\alpha\langle n_I(\omega)\rangle_0}{-i(\omega-\omega_c) + \kappa/2 + i\Pi(\omega_c)}\,. \tag{2.33}$$

In the limit of large number of photons in the input beam, we can neglect the contribution from the electronic system so that we obtain:

$$b_{out}(\omega) \approx \frac{-i(\omega-\omega_c) - \kappa/2 + i\Pi(\omega_c)}{-i(\omega-\omega_c) + \kappa/2 + i\Pi(\omega_c)} b_{in}(\omega)\,. \tag{2.34}$$

In experiments, one actually encounters a two-sided cavity (see Fig. 2.5 for the nomenclature), in which case the expression for the cavity equation of motion reads:

$$\dot{a} = i\,[H_{sys}, a] - \left(\frac{\kappa_1}{2} + \frac{\kappa_2}{2}\right) a - \sqrt{\kappa_1} b_{in} - \sqrt{\kappa_2} c_{in}\,, \tag{2.35}$$

so that for the output fields we get:

$$b_{out} = \sqrt{\kappa_1}\, a + b_{in} \tag{2.36}$$

$$c_{out} = \sqrt{\kappa_2}\, a + c_{in}\,. \tag{2.37}$$

By following the same reasoning as for the one-sided cavity and assuming the two mirrors are the same $\kappa_1 = \kappa_2 \equiv \kappa$, we obtain:

$$a(\omega) = -\frac{\sqrt{\kappa}[b_{in}(\omega) + c_{in}(\omega)] + i\alpha\langle n_I(\omega)\rangle_0}{-i(\omega - \omega_c) + \kappa + i\Pi(\omega_c)}\,. \tag{2.38}$$

Assuming again that the input flux is much larger than the electronic contribution, we can write:

$$c_{out}(\omega) = -\tau b_{in}(\omega) + (\ldots)c_{in}(\omega) \tag{2.39}$$

with

$$\tau = \frac{\kappa}{-i(\omega - \omega_c) + \kappa + i\Pi(\omega_c)} \equiv Ae^{i\phi} \tag{2.40}$$

being the transmission of the cavity, which is a complex number, and which depends on the electronic susceptibility $\Pi(\omega)$.

The phase and amplitude response of the cavity close to resonance $\omega \approx \omega_c$ are related to the susceptibility $\Pi(\omega)$ as follows:

$$\delta\phi = \Pi'(\omega)/\kappa, \tag{2.41}$$

$$\delta A/A_{in} = \Pi''(\omega)/\kappa, \tag{2.42}$$

where $\delta\phi = \phi_{out} - \phi_{in}$, $\delta A = A_{in} - A_{out}$, and $\Pi'(\omega) = \mathcal{R}e[\Pi(\omega)]$ ($\Pi''(\omega) = \mathcal{I}m[\Pi(\omega)]$) is the real (imaginary) part of the susceptibility. The frequency shift (or cavity pull) is proportional to the real part of the electronic susceptibility while the frequency broadening (or the modulation of the amplitude of the transmitted signal) is proportional to the imaginary part of the susceptibility.

2.5 SUMMARY

In this chapter, we summarize theoretical and experimental studies of atoms (real or artificial) coupled to superconducting resonators. In subsection 2.1.1, we demonstrate that the

properties of a single photon in a 3D resonator can be probed by atoms passing through the cavity. Then we discuss how the fixed atom-cavity coupling and scalability problems present in atomic cavity QED can be fixed by going from 3D cavity to 1D transmission line resonator and from a real atom to an artificial one. The main advantages of circuit QED:

1. The large dipole moment of the superconducting qubit and rms voltage of the resonator allow to reach easily the strong-coupling limit
2. Qubits can be separated by centimeter distances and entangling of qubits can be realized to implement two-qubits gates.

The idea to study quantum conductors embedded in superconducting resonators by coupling them to the wires and measuring differential conductance comes from mesoscopic cavity QED. In section 2.2, we discuss experimental and theoretical study of quantum dots with cavity QED. We provide the derivation of the electron-photon coupling Hamiltonian for mesoscopic cavity QED in section 2.3. And in section 2.4, we derive the optical transmission coefficient of the cavity

$$\tau = \frac{\kappa}{-i(\omega - \omega_c) + \kappa + i\Pi(\omega_c)} \tag{2.43}$$

and demonstrate that if the frequency is close to the cavity resonance, the phase shift and frequency broadening are related to the electronic susceptibility as

$$\delta\phi = \Pi'(\omega_c)/\kappa, \tag{2.44}$$

$$\delta A/A_{in} = \Pi''(\omega_c)/\kappa. \tag{2.45}$$

In this thesis, we apply methods from cavity QED to study different systems coupled to superconducting microwave cavity, such as a tunnel junction, a quantum dot tunnel coupled to metallic leads, a one-dimensional topological semiconducting wire and a superconducting ring.

3

MAJORANA FERMIONS

Majorana fermion is a particle that is its own antiparticle. Majorana fermions have been predicted by Ettore Majorana in 1937 [60]. Dirac equation

$$(i\gamma^{\mu}\partial_{\mu} - m)\,\phi = 0, \tag{3.1}$$

where ϕ is a four-component complex field, and γ matrices are required to obey the rules of the Clifford algebra, describes charged particles with spin 1/2, such as electrons. The idea of Ettore Majorana was to find an equation similar to Dirac equation that will describe a particle with spin 1/2 that is its on antiparticle [104]. If a particle is associated with a complex filed ϕ (see Eq.3.1), then the corresponding antiparticle will be associated with the conjugated field ϕ^*. For example, the antiparticle of an electron with charge e is a positron with charge $-e$ that appears as a solution of conjugated Dirac equation. Particles and their antiparticles have opposite charges, which means that the particle proposed by Ettore Majorana should have zero charge. Also, if the particle is associated with the field ϕ_M and its antiparticle is associated with the field ϕ_M^*, the Majorana particle should be associated with the real field $\phi_M \equiv \phi_M^*$. Under this condition, Ettore Majorana found the equation (later called Majorana equation)

$$\left(i\gamma_M^{\mu}\partial_{\mu} - m\right)\phi_M = 0, \tag{3.2}$$

where $\gamma_M^{\mu} = -\left(\gamma_M^{\mu}\right)^*$ are modified purely imaginary γ matrices that obey the rules of the Clifford algebra. One of the possibles forms of γ_M matrices is

$$\gamma_M^0 = \begin{pmatrix} 0 & 0 & 0 & -i \\ 0 & 0 & -i & 0 \\ 0 & i & 0 & 0 \\ i & 0 & 0 & 0 \end{pmatrix}, \tag{3.3}$$

$$\gamma_M^1 = \begin{pmatrix} 0 & 0 & i & 0 \\ 0 & 0 & 0 & i \\ i & 0 & 0 & 0 \\ 0 & i & 0 & 0 \end{pmatrix}, \tag{3.4}$$

$$\gamma_M^2 = \begin{pmatrix} i & 0 & 0 & 0 \\ 0 & i & 0 & 0 \\ 0 & 0 & -i & 0 \\ 0 & 0 & 0 & -i \end{pmatrix}, \tag{3.5}$$

$$\gamma_M^3 = \begin{pmatrix} 0 & 0 & 0 & -i \\ 0 & 0 & i & 0 \\ 0 & i & 0 & 0 \\ -i & 0 & 0 & 0 \end{pmatrix}. \tag{3.6}$$

Although Majorana fermions have been initially predicted as particles in high energy physics (the only elementary particle that could be Majorana fermion is neutrino), they could also emerge as quasiparticle excitations in condensed matter (solid-state) physics.

The special property of being its own antiparticle could be conveniently written in the second quantization formalism as

$$\gamma_j = \gamma_j^\dagger, \tag{3.7}$$

where γ_j is the Majorana operator. Conventional fermions are described by creation $c_j^\dagger$ and annihilation c_j operators. In order to build the Majorana operator γ_j, one should take a linear combination of conventional fermionic operators $c_j^\dagger$ and c_j, or electrons and holes

$$\gamma_j = uc_j^\dagger + vc_j. \tag{3.8}$$

In superconductors, the particle-hole symmetry relates the creation operator $\gamma_E^\dagger$ at energy E to the annihilation operator γ_{-E} at energy $-E$ [7]. At zero energy $E = 0$, a double degenerate level emerges in superconductors. This level has a special property

$$\gamma_{E=0}^\dagger = \gamma_{E=0}. \tag{3.9}$$

The zero-energy state in superconductors is the Majorana fermion.

Majorana fermions could be also used to build a topological quantum computer since they obey the non-abelian statistics in 2D [46]. In 3D, particles obey either the Fermi-Dirac statics and are thus called fermions or the Bose-Einstein statistics and are subsequently called bosons. Observing the behavior of multiparticle states during the exchange of particles allows to determine the statistics of the particles. For example, for a two-particle state

$$|\psi_1\psi_2\rangle = \pm|\psi_2\psi_1\rangle, \tag{3.10}$$

where sign $+(-)$ corresponds to particles being bosons (fermions). But in 2D systems, quasiparticles could obey statistics ranging continuously between Fermi–Dirac and Bose–Einstein statistics

$$|\psi_1\psi_2\rangle = e^{i\theta}|\psi_2\psi_1\rangle, \tag{3.11}$$

where θ is an arbitrary real number. If $\theta = 0(\pi)$, we recover the Bose-Einstein (Fermi-Dirac) statistics. Otherwise, particles obtain an arbitrary phase when they are interchanged. Such particles are called anyons. When anyon 1 and anyon 2 are interchanged twice, their wavefunction is not the same as the initial one, but rather $e^{i2\theta}|\psi_1\psi_2\rangle$. This means that the exchange of particles changes the state of the system with the same particle configuration (see Fig.3.1). The interchange of two Majorana operators is called braiding. And the result of the braiding depends on the order in which it is performed ($U_{12} \neq U_{21}$).

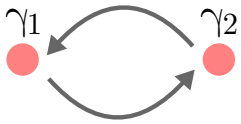

Figure 3.1: Exchange of two Majorana fermions γ_1 and γ_2 counterclockwise.

Studying Majorana fermions in the context of condensed matter physics is in focus of tremendous theoretical and experimental research activity. On one hand, this scrutiny is driven by the fundamental interest in particles that are their own antiparticles. On the other hand, such particles may have numerous applications in quantum computing.

3.1 CONVENTIONAL FERMIONIC AND MAJORANA OPERATORS

In condensed matter physics, Majorana fermions emerge as zero-energy and charge-neutral quasiparticles in superconductors.

Usual fermionic creation $c_j^\dagger$ and annihilation c_j operators obey anticommutation relations

$$\{c_i, c_j^\dagger\} = \delta_{i,j}, \qquad \{c_i, c_j\} = 0. \tag{3.12}$$

In order to create a neutral excitation, one needs to take a linear combination of fermionic creation and annihilation operators $c_j^\dagger, c_j$. Let us define Majorana operators as

$$\gamma_{A,j} = -i\left(c_j - c_j^\dagger\right), \qquad \gamma_{B,j} = c_j + c_j^\dagger. \tag{3.13}$$

These Majorana operators still satisfy the anticomutation relations

$$\{\gamma_{\alpha,j}, \gamma_{\alpha',j'}\} = 2\delta_{\alpha\alpha'}\delta_{jj'} \qquad \text{with} \qquad \alpha = A, B \qquad \text{and} \qquad j = 1, ..., N, \tag{3.14}$$

but also have a special property

$$\gamma_{\alpha,j} = \gamma_{\alpha,j}^\dagger. \tag{3.15}$$

Eq.3.15 demonstrates that Majorana fermion $\gamma_{\alpha,j}$ is identical to its antiparticle $\gamma_{\alpha,j}^\dagger$.

In the following sections, we discuss several theoretical models of the systems that support Majorana fermions as well as the experimental implementation of these systems. In section 3.2, we provide details on the Kitaev chain model as we use it in chapters 5,7. The Kitaev model is the simplest model that takes into account both Majorana states and bulk states of the superconductor. In section 3.3, we describe the spin-orbit coupled nanowire model, a realistic model that describes emergence of the Majorana fermions and has been already implemented experimentally. We use this model in chapter 5 to demonstrate that our findings for Kitaev model remain valid for a more realistic system. In section 3.4, we discuss first experimental signatures of Majorana fermions in condensed matter systems, e.g. zero-bias peak. We continue by presenting the fractional Josephson effect and its connection to the Majorana fermions physics in section 3.5 before a conclusive discussion in section 3.6.

3.2 PROTOTYPE MODEL FOR 1D P-WAVE SUPERCONDUCTOR: KITAEV MODEL

In this section, we introduce a toy model for a 1D topological superconductor that supports Majorana fermions, namely the Kitaev model for a spinless p-wave superconductor [49]. This model describes a chain of N sites with nearest-neighbor p-wave superconducting pairing. The Kitaev chain Hamiltonian reads

$$H_K = -\mu \sum_{j=1}^{N} c_j^\dagger c_j - \frac{1}{2} \sum_{j=1}^{N-1} \left(t c_j^\dagger c_{j+1} + \Delta c_j c_{j+1} + h.c. \right), \tag{3.16}$$

where μ is the chemical potential, t is the nearest-neighbor hopping amplitude and Δ is the p-wave superconducting pairing potential.

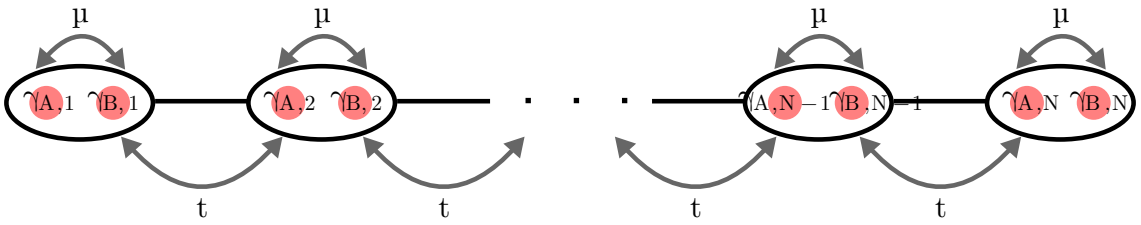

Figure 3.2: Scheme of the Kitaev chain.

It is instructive to first study the bulk properties of the Kitaev chain by imposing periodic boundary conditions on the system, $c_{N+1} \equiv c_1$. For periodic boundary conditions, we can use the Fourier description for the electronic operators:

$$c_j = \frac{1}{\sqrt{N}} \sum_k c_k e^{ikj}. \tag{3.17}$$

where c_k is the fermionic annihilation operator with momentum $k = 2\pi n/N$ (assuming the lattice spacing $d \equiv 1$ from now on), with $n = 1, ..., N$. By doing so, we can write the Kitaev Hamiltonian Eq. 5.4 in momentum space

$$H_K = \sum_{k>0} H^K_{BdG}(k), \tag{3.18}$$

with

$$H^k_{BdG}(k) = \xi_k(c^\dagger_k c_k - c_{-k}c^\dagger_{-k}) - i\Delta \sin k(c_{-k}c_k - c^\dagger_k c^\dagger_{-k}), \tag{3.19}$$

is the Bogoliubov-de Gennes Hamiltonian and $\xi_k = -t\cos k - \mu$. We can simply diagonalize the H_K in the k-space and write:

$$H_K = \sum_{k>0} E_k \left(\gamma^\dagger_k \gamma_k + \gamma^\dagger_{-k}\gamma_{-k}\right), \tag{3.20}$$

when expressed in terms of quasiparticle operators

$$c_k = u^*_k \gamma_k + v_k \gamma^\dagger_{-k}, \tag{3.21}$$

$$c^\dagger_{-k} = -v^*_k \gamma_k + u_k \gamma^\dagger_{-k}. \tag{3.22}$$

Here, the functions u_k and v_k are given by

$$|u_k|^2 = \frac{1}{2}\left(1 + \frac{\xi_k}{E_k}\right), \tag{3.23}$$

$$|v_k|^2 = \frac{1}{2}\left(1 - \frac{\xi_k}{E_k}\right), \tag{3.24}$$

and

$$E_k = \pm\sqrt{(-t\cos k - \mu)^2 + (\Delta \sin k)^2}, \tag{3.25}$$

is the bulk energy spectrum for the Kitaev chain (see Fig.3.3).

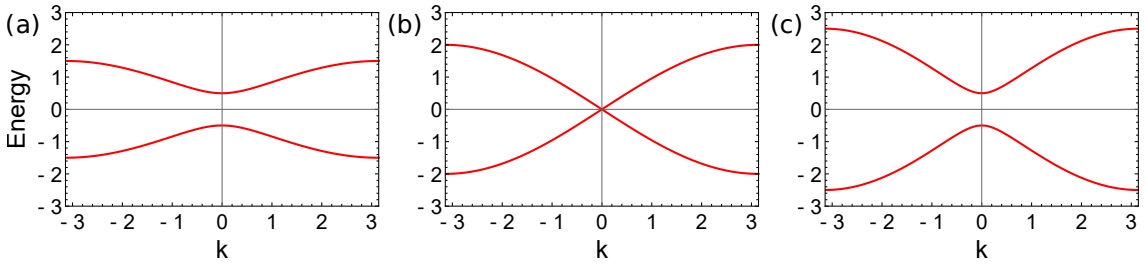

Figure 3.3: Bulk energy spectrum E_k of the Kitaev chain for parameters: $t = \Delta = 1$. a) The gap at $k = 0$ is open at $\mu = -0.5$ in the topological phase ($|\mu| < t$), b) the gap at $k = 0$ closes at $\mu = -1.0$ at the topological phase transition ($|\mu| = t$) , c) the gap at $k = 0$ opens again at $\mu = -1.5$ in the non-topological (trivial) phase ($|\mu| > t$).

The topological phase transition happens when the gap closes, $E_k = 0$. From Eq.3.25 we notice that the gap closes at $k = 0$ for $\mu = -t$ and $k = \pi$ for $\mu = t$. Thus $|\mu| = t$ is the topological phase transition point. In the following, we demonstrate that the Kitaev chain is in the topological phase when $|\mu| < t$, and in the non-topological phase when $|\mu| > t$. In the topological phase, the Majorana fermions emerge at both ends of the Kitaev chain with open boundary conditions.

Let us determine a topological phase of the system by introducing an integer-valued topological invariant — a winding number [68]. It is convenient to define the invariant in the pseudospin basis $\vec{h}(k)$, so let us rewrite the BdG Hamiltonian Eq. C.30 and set $\Delta = t$ as

$$H^k_{BdG}(k) = \vec{h}(k) \cdot \vec{\tau} \tag{3.26}$$

where $\vec{\tau} = (\tau^k_x, \tau^k_y, \tau^k_z)$ are Pauli matrices acting on the particle-hole basis $\left(c_k, c^\dagger_{-k}\right)$, $h_y(k) = -t\sin(k)$ and $h_z(k) = (-t\cos(k) - \mu)$. The pseudospin $\vec{h}(k)$ is defined in the yz-plane.

Let us introduce a unit vector

$$\hat{h}(k) = \frac{\vec{h}(k)}{\left|\vec{h}(k)\right|} \equiv \cos(\theta_k)\,\tau_y^k + \sin(\theta_k)\,\tau_z^k, \tag{3.27}$$

where $\left|\vec{h}(k)\right| = \sqrt{h_y^2 + h_z^2} = E_k$. The winding number is defined in terms of this unit vector.

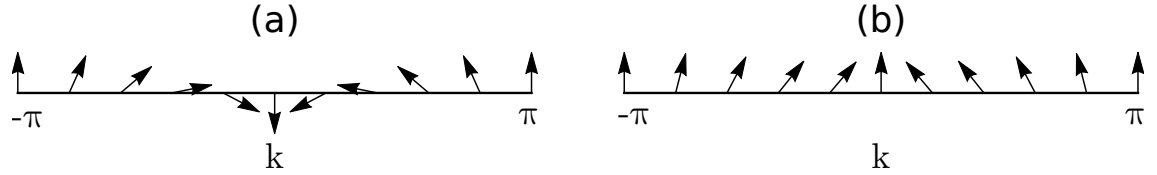

Figure 3.4: The pseudospin vector $\hat{d}(k)$ for parameters: $t = \Delta = 1$. a) $\mu = -0.5$; the pseudospin winds once along the Brillouin zone, i.e. $w = -1$, b)$\mu = -1.5$; the pseudospin does not wind along the Brillouin zone, i.e. $w = 0$.

The states of the system with periodic boundary conditions form a ring T^1 in the momentum space, while the unit vector $\hat{h}(k)$ is defined on a unit circle S^1 in the yz-plane. Thus the angle θ_k is a mapping $\theta_k : S^1 \to T^1$. The winding number is the fundamental group of this mapping

$$w = \oint \frac{d\theta_k}{2\pi}, \tag{3.28}$$

where $\theta_k = \arctan\left(-\dfrac{t\sin(k)}{t\cos(k) + \mu}\right)$ (we perform the rotation so that the angle is defined in the xy-plane) and the integral is taken over the first Brillouin zone. The winding number shows how many times the unit vector $\hat{d}(k)$ rotates in the yz-plane around the Brillouin zone (see Fig.3.4). The absolute value of the winding number is equal to the number of Majorana fermions at each end of the chain. The winding number can be any integer and remains constant as long as the system is gapped. The winding number changes only when the gap closes at the topological phase transition and is not defined at the phase transition point since $E_k = 0$ when the gap closes.

For the Kitaev model, the winding number $w = 0$ for $t < |\mu|$ implies the absence of Majorana fermions in the chain (or that the system is in non-topological phase) and $w = -1$ for $t > |\mu|$ imples the existence of one Majorana fermion at each of the chain (or that the system is in the topological phase) [96].

Having determined the conditions for the topological phase transitions, we consider a finite chain with Majorana fermions emerging at its ends [3, 49]. Each site of the chain in the Kitaev model is described by a pair of creation $c_j^\dagger$ and annihilation c_j fermionic operators. Let us formally define the Majorana operators by decomposing $c_j, c_j^\dagger$ operators in the Kitaev Hamiltonian Eq.5.4 in terms of two Majorana operators

$$c_j = \frac{1}{2}\left(\gamma_{B,j} + i\gamma_{A,j}\right), \qquad c_j^\dagger = \frac{1}{2}\left(\gamma_{B,j} - i\gamma_{A,j}\right), \tag{3.29}$$

where $\gamma_{A,j}$ and $\gamma_{B,j}$ are the Majorana operators that fulfill the relations

$$\gamma_{\alpha,j} = \gamma_{\alpha,j}^\dagger, \qquad \{\gamma_{\alpha,j}, \gamma_{\alpha',j'}\} = 2\delta_{\alpha\alpha'}\delta_{jj'}, \tag{3.30}$$

with $\alpha = A, B$ and $j = 1, ..., N$.

In terms of the Majorana operators $\gamma_{A,j}$ and $\gamma_{B,j}$, the initial Hamiltonian of the Kitaev chain Eq.5.4 becomes

$$H_K = -\frac{\mu}{2}\sum_{j=1}^{N}\left(i\gamma_{B,j}\gamma_{A,j} + 1\right) - \frac{i}{4}\sum_{j=1}^{N-1}\Big[(\Delta + t)\,\gamma_{B,j}\gamma_{A,j+1} + (\Delta - t)\,\gamma_{A,j}\gamma_{B,j+1}\Big]. \tag{3.31}$$

Figure 3.5: Schematic illustration of the Hamiltonian in Eq.3.32. Majorana operators $\gamma_{A,j}, \gamma_{B,j}$ from the same site j are paired.

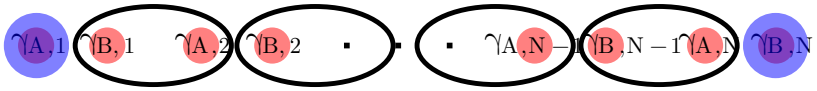

Figure 3.6: Schematic illustration of the Hamiltonian in Eq.3.33. Majorana operators $\gamma_{B,j}, \gamma_{A,j+1}$ from adjacent sites are paired. Majorana operators $\gamma_{A,1}$ and $\gamma_{B,N}$ drop out of the Hamiltonian.

Let us first consider two special cases.

1) Trivial case: $|\Delta| = t = 0$ and $\mu < 0$. Then Eq.3.31 is simplified and it reads

$$H_K = -\frac{\mu}{2} \sum_{j=1}^{N} \left(i\gamma_{B,j}\gamma_{A,j} + 1 \right). \tag{3.32}$$

In this case, the Hamiltonian H_K contains pairing only between the Majorana operators $\gamma_{A,j}, \gamma_{B,j}$ from the same site j (see Fig.3.5). Therefore, all the Majorana operators are always paired. For $|\Delta| = t = 0$ and $\mu < 0$, the Kitaev chain is in the topologically trivial (non-topological) phase.

2)Non-trivial case: $|\Delta| = t > 0$ and $\mu = 0$. For this choice of parameters, the Hamiltonian of the Kitaev chain Eq.3.31 reads

$$H_K = -i\frac{t}{2} \sum_{j=1}^{N-1} \gamma_{B,j}\gamma_{A,j+1}. \tag{3.33}$$

In this case, only the Majorana operators $\gamma_{B,j}, \gamma_{A,j+1}$ with $j = 1, ..., N-1$ from different sites are paired, while the operators $\gamma_{A,1}$ and $\gamma_{B,N}$ do not enter the Hamiltonian (see Fig.3.6). Let us introduce a new fermionic operator that combines the Majorana operators from different sites

$$f_j = \frac{1}{2} \left(\gamma_{A,j+1} + i\gamma_{B,j} \right). \tag{3.34}$$

The Kitaev Hamiltonian Eq.(3.33) can be written in terms of these new operators $f_j, f_j^\dagger$ as

$$H_K = t \sum_{j=1}^{N-1} \left(f_j^\dagger f_j - \frac{1}{2} \right). \tag{3.35}$$

Let us also combine two Majorana operators $\gamma_{A,1}$ and $\gamma_{B,N}$ that dropped out from Eq.3.33 and introduce an ordinary fermionic operator

$$\tilde{c}_M = \frac{1}{2} \left(\gamma_{A,1} + i\gamma_{B,N} \right), \tag{3.36}$$

that is a sum of two operators localized at sites 1 and N, respectively, and thus is a highly non-local object.

The finite size of the chain with open boundary conditions results in an overlap between $\gamma_{A,1}$ and $\gamma_{B,N}$ operators. This overlap can be described by an effective Hamiltonian [49]

$$H_K^{eff} = -i\frac{t}{2}\gamma_{B,N}\gamma_{A,1}, \tag{3.37}$$

where $t \propto \exp(-L/\xi)$ with L being the length of the chain and ξ being the coherence length.

The Hamiltonian H_K^{eff} can be written in terms of the ordinary fermionic operators as

$$H_{eff} = 2\epsilon_M \left(\tilde{c}_M^\dagger \tilde{c}_M - \frac{1}{2} \right), \tag{3.38}$$

where ϵ_M is called the Majorana energy splitting and $\epsilon_M = \frac{t}{4} \propto \exp(-L/\xi)$. Let us introduce a number of particles operator

$$n_M = \tilde{c}_M^\dagger \tilde{c}_M. \tag{3.39}$$

Depending on the Majorana state being empty ($n_M = 0$) or occupied ($n_M = 1$), the Majorana ground state is either even or odd with energy $-\epsilon_M$ or ϵ_M, respectively.

All the aforementioned analysis of the topological properties of the Kitaev chain remains valid for arbitrary values of μ, Δ and t. However, p-wave superconductors are very rare in nature (the only known p-wave superconductor is Sr_2RuO_4 [47]). So how one can realize a chain of spinless electrons in a laboratory?

The first theoretical proposal to effectively implement the Kitaev chain was to use an edge of a 2D topological insulator proximitized to an s-wave superconductor [42, 43]. At the edge of the 2D topological insulator, electrons with spin up propagate clockwise around the edge while electrons with spin down propagate counterclockwise, making the system appear spinless. p-wave superconductivity is generated in the system when interfacing the topological insulator with a s-wave superconductor.

3.3 PRACTICAL REALIZATION OF MAJORANA FERMIONS IN 1D P-WAVE SUPERCONDUCTORS: SPIN-ORBIT COUPLED NANOWIRE

In this section, we discuss in detail one of the theoretical proposals of experimental realization of a 1D spinless p-wave superconductor: a spin-orbit coupled nanowire subject to a magnetic field and in proximity to an s-wave superconductor. We use in chapter 5. This theoretical model has been first proposed in [59, 71] based on earlier semiconductor-based proposals [2, 86] and implemented experimentally in [64]. Three ingredients are combined in this model to engineer p-wave superconductivity: a 1D wire with strong spin-orbit coupling, a conventional s-wave superconductor, and a magnetic field. The scheme of the setup is shown in Fig.3.7.

The Hamiltonian for the nanowire with spin-orbit coupling in the presence of the magnetic field and in proximity to an s-wave superconductor reads [71]

$$H = \int \Psi^\dagger(y)\,\mathcal{H}\Psi(y)\,dy, \tag{3.40}$$

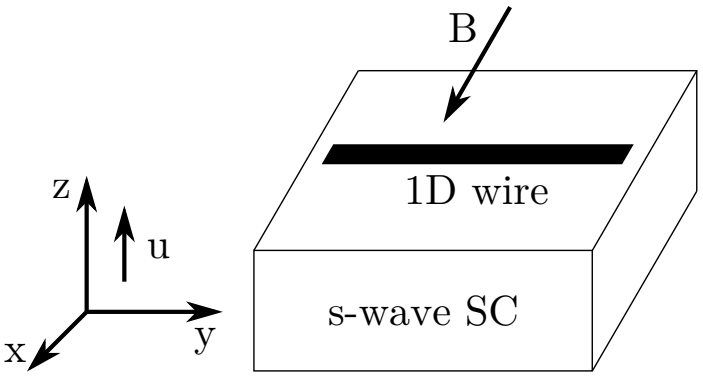

Figure 3.7: Scheme of the superconductor-semiconductor wire setup. 1D wire lies along the y axis, spin-orbit interaction u is along z axis and a magnetic field B is along x axis.

$$\mathcal{H} = \left(\frac{p^2}{2m} - \mu\right)\tau_z + up\sigma_z\tau_z + B\sigma_x + \Delta\tau_x, \tag{3.41}$$

where $\Psi = \left(\psi_\uparrow^\dagger, \psi_\downarrow^\dagger, \psi_\downarrow, -\psi_\uparrow\right)$, $\psi_{\uparrow,(\downarrow)}(y)$ annihilates spin-up (spin-down) electrons at position y. The Pauli matrices σ_i, τ_i, $i = x, y, z$ act in spin and particle-hole space, respectively. μ is the chemical potential, u is the spin-orbit interaction, B is the magnetic field and Δ is the s-wave pairing potential induced by proximity. We chose the wire to lie along the y axis, the spin-orbit interaction to be along the z axis, and the magnetic field to be along the x axis (see Fig.3.7). The directions of the fields could be chosen arbitrary provided that the spin-orbit field and the magnetic field are orthogonal.

The bulk energy spectrum for the spin-orbit coupled nanowire reads

$$\begin{aligned} E_\pm^2 = {} & B^2 + \Delta^2 + \left(\frac{p^2}{2m} - \mu\right)^2 + (up)^2 \\ & \pm 2\sqrt{B^2\Delta^2 + B^2\left(\frac{p^2}{2m} - \mu\right)^2 + (up)^2\left(\frac{p^2}{2m} - \mu\right)^2}. \end{aligned} \tag{3.42}$$

Let us discuss the energy spectrum of spin-orbit coupled nanowire and how it can emulate a spinless p-wave superconductor. In the absence of the magnetic field $B = 0$ and

induced superconductivity $\Delta = 0$, the energy spectrum consists of two shifted parabolas that cross at the momentum $p = 0$. Due to the spin-orbit coupling, these two parabolas have opposite spins. When the magnetic field is applied, the crossing at $p = 0$ is lifted and the gap at $p = 0$ opens. If we tune the chemical potential μ so that it lies inside the field-induced gap, the wire appears spinless. The superconducting pairing Δ opens gaps at the Fermi momentum $p = \pm p_F = \pm\sqrt{2m\mu}$ and ensures that they always remain finite. For large magnetic field $B \gg \Delta$ we can project away the upper energy band and the wire becomes effectively a spinless p-wave superconductor.

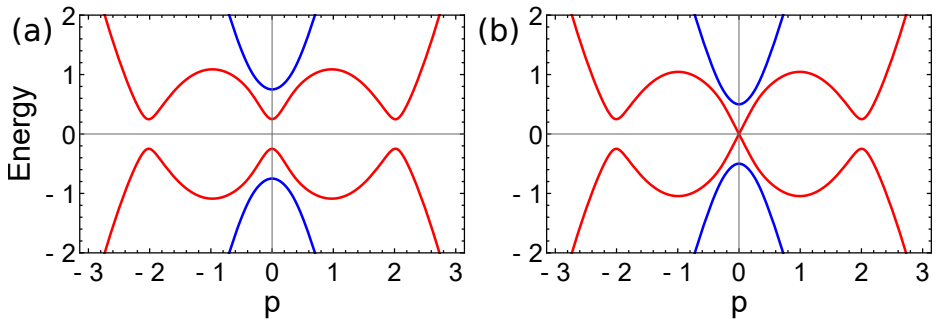

Figure 3.8: Bulk energy spectrum $E_\pm(p)$ of the spin-orbit coupled nanowire for parameters $\mu = 0$ and $\Delta = 0.25$. The momentum (energy) scale is set by $m\alpha\left(\frac{m\alpha^2}{2}\right)$. The blue line corresponds to the upper energy branch E_+ and the red line corresponds to the lower energy brunch E_-. a) The gap at $p = 0$ is open for $B = 0.5$ in the topological phase, $B > \sqrt{\Delta^2 + \mu^2}$, b) the gap at $p = 0$ closes at $B = 0.25$ at the topological phase transition point, $B = \sqrt{\Delta^2 + \mu^2}$.

The bulk energy spectrum $E_\pm$ has two gaps:

1) the gap at $p = 0$, which could be created by the magnetic field and is given by

$$E_0 = E(p = 0) = \left|B - \sqrt{\Delta^2 + \mu^2}\right|; \tag{3.43}$$

2) the gap at $p = \pm p_F$, which is created by the strong-spin orbit interaction and is always finite due to the induced superconductivity. The gap is given by

$$E_1 = E(p = \pm p_F) = \xi_{p=\pm p_F} \pm u p_F. \tag{3.44}$$

The quantum phase transition occurs when the gap at $p = 0$ closes, $E_0 = 0$, and $B^2 = \Delta^2 + \mu^2$ (see Fig.3.8). When $B^2 > \Delta^2 + \mu^2$, E_0 is dominated by the magnetic field B, the wire is in the topological phase with Majorana fermions at the ends of the wire. When $B^2 < \Delta^2 + \mu^2$, E_0 is dominated by the pairing potential Δ, the wire is in the non-topological phase.

Now we demonstrate that in the limit of strong spin–orbit coupling, the nanowire model Eq.3.41 reduces at low energies to a spinless p-wave-superconductor.

Let us diagonalize the Hamiltonian for the spin-orbit coupled nanowire $\mathcal{H} = H_0 + \Delta\tau_x$ in the absence of the induced pairing Δ and then treat the latter perturbatively [34, 73]

$$H_0 = \left(\frac{p^2}{2m} - \mu\right)\tau_z + up\sigma_z\tau_z + B\sigma_x. \tag{3.45}$$

In order to do so, we perform the unitary transformation

$$\tilde{H}_0 = UH_0U^\dagger \qquad \text{with} \qquad U = \exp\left(i\alpha\sigma_y\tau_z/2\right). \tag{3.46}$$

If we choose α so that

$$\tan(\alpha) = \frac{B}{up}, \tag{3.47}$$

$\tilde{H}_0$ takes the form

$$\tilde{H}_0 = \left[\frac{p^2}{2m} - \mu + \sqrt{u^2p^2 + B^2}\sigma_z\right]\tau_z. \tag{3.48}$$

Now let us reintroduce the pairing term $\Delta\tau_x$ and apply the transformation U to it.

Then $\tilde{H}_{NW}$ reads

$$\tilde{H}_{NW} = \left[\frac{p^2}{2m} - \mu + \sqrt{u^2p^2 + B^2}\sigma_z\right]\tau_z + \frac{\Delta up}{\sqrt{u^2p^2 + B^2}}\tau_x - \frac{\Delta B}{\sqrt{u^2p^2 + B^2}}\sigma_y\tau_y. \tag{3.49}$$

Neglecting the last term in Eq.C.50 for $B \gg \Delta, \mu$ the effective Hamiltonian reads

$$\tilde{H}_{eff} = \left[\frac{p^2}{2m} - \mu + \sqrt{u^2p^2 + B^2}\sigma_z\right]\tau_z + \frac{\Delta up}{\sqrt{u^2p^2 + B^2}}\tau_x. \tag{3.50}$$

The low-energy subspace at $p = \pm p_F$ is formed by the bands with $\sigma_z = -1$. The projection of $\tilde{H}_{eff}$ C.51 to the lower bands yields

$$\tilde{H}_{eff} = \left[\frac{p^2}{2m} - \mu - \sqrt{u^2p^2 + B^2}\right]\tau_z + \frac{\Delta up}{\sqrt{u^2p^2 + B^2}}\tau_x. \tag{3.51}$$

The large spin-orbit coupling $\epsilon_{SO} \gg \Delta$ guarantees that we can neglect the coupling to high-energy degrees of freedom near $\pm p_F$. Linearizing the Hamiltonian $\tilde{H}_{eff}$ 3.51 around the Fermi momenta and using $|up| \equiv \epsilon_{SO} \gg B$ the effective Hamiltonian takes the form

$$\tilde{H}_{eff} = u\,(|p| - p_F)\,\tau_z + \text{sign}\,(p)\,\Delta\tau_x. \tag{3.52}$$

This Hamiltonian describes a spinless p-wave superconductor with superconducting pairing $\Delta_p \propto \Delta p$ similar to the Kitaev model described in the previous section.

3.4 EXPERIMENTAL SIGNATURES OF MAJORANA FERMIONS: OBSERVATION OF ZERO-BIAS PEAK

There are several experimental manifestations associated with the presence of Majorana fermions, such as the zero-bias peak in the topological region [19, 25, 33, 64], the depen-

dence of the Majorana energy splitting on the Zeeman splitting, or the size of the system [1], enhanced conductance at zero energy in chain of magnetic atoms [66], ac fractional Josephson effect [81, 103]. Let us discuss several of them in more detail.

First experimental observation of signatures of the Majorana fermions has been reported in [64]. They studied a nanowire by electrical measurements and observed a peak at zero bias, which is consistent with the presence of zero-energy (midgap) bound states at the ends of the wire.

The experimental setup consists of InSb nanowire connected to one normal and one superconducting electrode in the presence of magnetic field. This physical system has all three components required for the emergence of Majorana fermions [59, 71]: a nanowire with strong spin-orbit interaction, proximity-induced superconductivity and magnetic field. However, the two latter quantities should be related as $E_z > \sqrt{\mu^2 + \Delta^2}$. In order to satisfy this relation, one needs to create Zeeman energy $E_z = g\mu_B B/2$ (μ_B is the Bohr magneton) large enough to exceed the induced superconducting gap $\Delta \approx 250\mu$eV. Choosing bulk InSb with $g \approx 50$, one can enter a topological regime at $\mu = 0$ ($E_z > \Delta$) given the magnetic filed $B \approx 0.15$T. At the same time, InSb nanowires have a strong spin-orbit interaction $\alpha = 0.2$ eV·Å.

The differential conductance dI/dV at voltage V for different values of magnetic field was measured. The peak at $V = 0$ appears for magnetic field $B \approx 100$ mT. This peak remains stuck to zero over a substantial range of magnetic fields (up to $B \approx 400$ mT). The zero-bias peak signals a presence of midgap states in the wire and could be interpreted as a transport signature of Majorana fermions. Thus, this experiment provides first evidence for the presence of the Majorana fermions in nanowires with proximity-induced superconductivity.

Recently, observation of exponential suppression of energy splitting with increasing wire length in InAs nanowire segment with epitaxial aluminium, which forms a proximity-induced superconducting Coulomb island, has been reported in [1]. For short devices of a few hundred nanometres, they found that energy of the sub-gap state oscillate as a function of magnetic field, as is expected for the Majorana fermions.

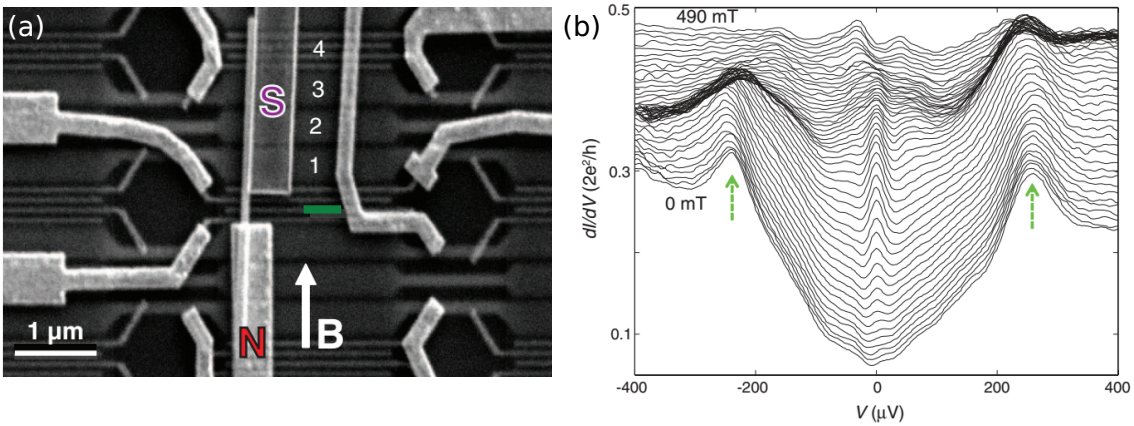

Figure 3.9: a) Experimental setup. Scanning electron microscope image of the device with normal (N) and superconducting (S) contacts. The S contact only covers the right part of InSb nanowire. The underlying gates, numbered 1 to 4, are covered with a dielectric. An external magnetic field B is aligned parallel to the wire in order not to destroy superconductivity. The Rashba spin-orbit interaction is perpendicular to the nanowire and to magnetic field as required. Parameters of the wire: $\alpha = 0.2$ eV·Å, $\Delta \approx 250\mu$eV. b) dI/dV as a function of V for different values of magnetic field B: from 0 to 490 mT from in 10 mT steps. Green arrows indicate the induced gap peaks. Reproduced from [64].

3.5 FRACTIONAL JOSEPHSON EFFECT

3.5.1 *Theoretical description of dc Josephson effect*

The Josephson effect describes the appearance of a supercurrent in a weak link between two superconductors. For usual s-wave superconductors, the supercurrent appears due to the tunneling of the Cooper pairs with charge 2e across a weak link. In this section, we discuss dc Josephson effect, when there is no voltage applied to the junction and the phases of the superconductor are created by magnetic flux. The Josephson current depends on the phase difference of the superconductors and is given by $I_J \propto \sin(\phi_R - \phi_L)$, where ϕ_L (ϕ_R) is a phase of the left (right) superconductor. In case of topological superconductors (see Fig.3.10) the supercurrent appears due to fusing the Majorana fermions across a weak link. The current is carried by charge e quasiparticles instead of the Cooper pairs and is

given by $I_J \propto \sin\left(\frac{\phi_R - \phi_L}{2}\right)$. This effect that arises because of the degeneracy of the zero energy Majorana modes is called the fractional Josephson effect.

The fractional Josephson effect is one of the hallmarks of the Majorana fermions [43, 49, 50, 59, 74]. It corresponds to 4π periodicity of the supercurrent in the superconductor phase difference across a weak link, as opposed to 2π periodicity for the usual Josephson effect in conventional s-wave superconductors.

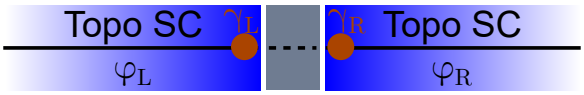

Figure 3.10: Scheme of a Josephson junction consisting of two topological wires (black lines) connected via a topologically trivial weak link (dashed line). p-wave superconductivity is created by a proximity to s-wave superconductors (blue rectangles). A weak link could be created by an insulating barrier (grey rectangle). The left (right) s-wave superconductor has a phase ϕ_L (ϕ_R). The presence of the Majorana fermions γ_L and γ_R (brown circles) give rise to the 4π-periodic Josephson current across a weak link.

Let us consider a simplest setup required to observe the fractional Josephson effect: the superconductor-insulator-superconductor junction (see Fig.3.10). We assume that the topological superconductors are long enough, so that only a finite overlap between two Majorana fermions γ_L and γ_R at both sides of a weak link could be taken into account. Let us define a usual fermionic operator that consists of two Majorana operators

$$\tilde{c}_M = \frac{1}{2}(\gamma_L + i\gamma_R) \tag{3.53}$$

and a number of particles operator

$$n_M = \tilde{c}_M^\dagger \tilde{c}_M. \tag{3.54}$$

In the topological phase, the Josephson current is mainly transmitted by the Majorana states. Effective low-energy Hamiltonian for a setup shown in Fig. 3.10 reads

$$H_{eff} = \frac{\Gamma}{2}\cos\left(\frac{\Delta\phi}{2}\right) i\gamma_L\gamma_R = \Gamma\cos\left(\frac{\Delta\phi}{2}\right)\left(n_M - \frac{1}{2}\right), \tag{3.55}$$

where $\Delta\phi = \phi_R - \phi_L$. Note that $[H_{eff}, n_M] = 0$, so that the number of Majorana fermions is conserved.

The Majorana energy splitting is given by

$$E = \pm\Gamma\cos\left(\frac{\Delta\phi}{2}\right), \tag{3.56}$$

where $-$ sign corresponds to even parity ($n_M = 0$) and $+$ corresponds to odd parity ($n_M = 1$). The energy spectrum is presented in Fig.3.11.

The Josephson current could be defined as [59] $I_J = -\dfrac{\partial\langle H_{eff}\rangle}{\partial\Delta\phi}$ and is equal to

$$I_J = \pm\frac{\Gamma}{2}\sin\left(\frac{\Delta\phi}{2}\right). \tag{3.57}$$

For even parity, the Josephson current carried by the Majoranas is $I_J \propto \sin\left(\frac{\Delta\phi}{2}\right)$. For odd parity, it is $I_J \propto -\sin\left(\frac{\Delta\phi}{2}\right)$. Since the parity of the Majorana state is a conserved quantity, the Josephson current is 4π-periodic in the phase difference. And also the sign of the Josephson current could allow to distinguish the parity of the Majorana state.

The simplest way to reveal the fractional Josephson effect is to measure directly the current through the junction. But if the measurement is performed on time scale which is long compared to relaxation/switching time of the Majorana fermions, then the ground state energy becomes $\epsilon_M \propto -\left|\cos\left(\frac{\Delta\phi}{2}\right)\right|$. In this case the Josephson current is $I_J \propto \left|\sin\left(\frac{\Delta\phi}{2}\right)\right|$ and is 2π-periodic. However, if there is a voltage difference across the junction

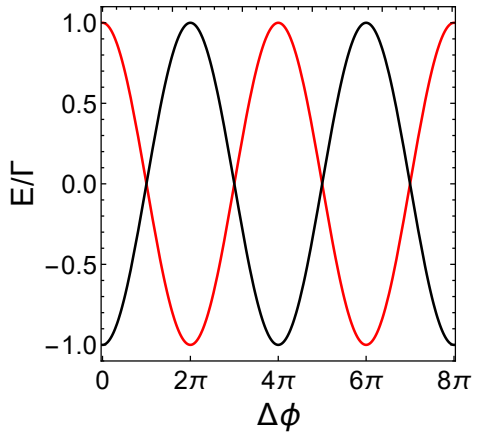

Figure 3.11: Energy spectrum E as a function of the phase difference across the junction $\Delta\phi$. Energy comes back to its initial value at 4π.

it gives rise to ac Josephson current. And in this case 4π Josephson current has been observed [81, 103].

3.5.2 *Observation of 4π-periodic ac Josephson current*

In this section, we discuss other experimental manifestation of Majorana fermions, namely the fractional Josephson effect. In [81], the first observation of the fractional ac Josephson effect in a hybrid superconductor-semiconductor nanowire junction has been reported. When the junction is irradiated with a frequency ω_0 in the absence of an external magnetic field, quantized voltage steps (Shapiro steps) with a height $\hbar\omega_0/2e$ are observed, as is expected for conventional superconductor junctions, where the supercurrent is carried by charge $2e$ Cooper pairs. At high magnetic fields the height of the first Shapiro step is doubled to $\hbar\omega_0/e$, suggesting that the supercurrent is carried by charge e quasiparticles. This experimental result is as a signature of the Majorana fermions.

In [81], the experimental device consists of Nb/InSb/Nb Josephson junctions. Superconductivity in InSb is induced by the proximity effect from a Nb film placed on top of the InSb nanowire. The supercurrent is flowing only in the nanowire. This experimental realization is based on the theoretical proposal [59].

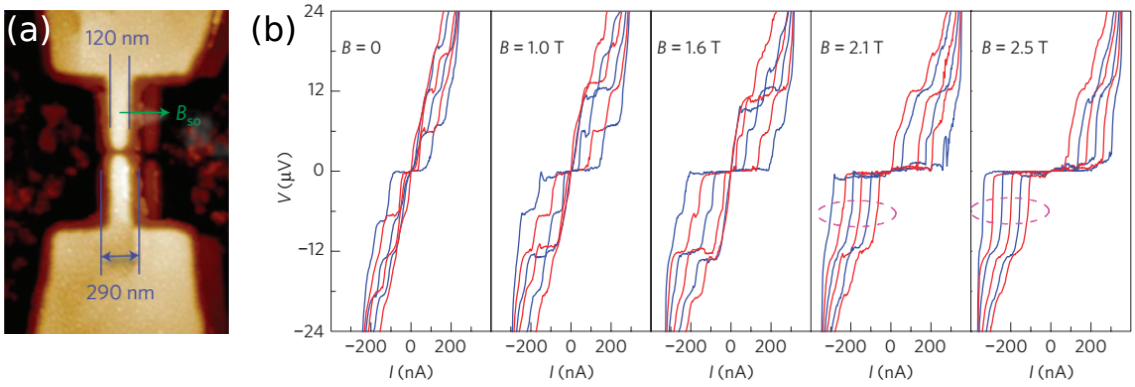

Figure 3.12: a) Experimental setup. AFM image of a Josephson junction. The light areas are Nb. A light brown halo around Nb is a thin 2–3 nm Nb layer which defines the width of the semiconductor wire. Green arrow indicated the direction of the spin–orbit field B_{SO}. b) $I-V$ characteristic of a Nb/InSb/Nb Josephson junction in the presence of magnetic field $B \parallel I$ measured with voltage V_{rf} between 3 and 6 mV with 0.6 mV steps. For $B < 2$ T, Shapiro steps with a height $\Delta V = \hbar\omega_0/2e = 6\mu V$ are clearly observed. For $B > 2$ T the plateau at $6\mu V$ disappears, as emphasized by dashed ovals, and the first step is observed at $\hbar\omega_0/e = 12\mu V$. This doubling of the first Shapiro step is a signature of the presence of the Majorana fermions in the system. Reproduced from [81].

In the presence of microwave excitation with frequency ω_0, phase locking between the rf field and the Josephson supercurrent gives rise to constant-voltage Shapiro steps in the $I-V$ characteristics at $V_n = n\frac{\hbar\omega_0}{q}$, where q is the charge of quasiparticles and $n = 0, \pm1, \pm2, \ldots$ numbers of the Shapiro steps. At zero magnetic field $B = 0$ and $\omega_0 = 3$ GHz the Shapiro steps with $\Delta V = 6\mu V$ were observed (up to $n = 10$). This value of ΔV is consistent with the Cooper pair (with charge $2e$) tunneling. When a low magnetic field $B \parallel I$, $B < 2$ T is applied, first three Shapiro steps at $V = 6, 12$ and 18μ V are clearly visible [81]. The first step with $n = 1$ at $6\mu V$ disappears above $B \approx 2$ T. This observation could be explained if the current is carried by the charge e quasiparticles, e.g. the Majorana fermions. Thus, the doubling of the Shapiro step is a signature of the topological quantum phase transition and presence of the Majorana fermions.

Another experimental observation of the doubling of the Shapiro step has been reported in [103]. In this paper, they study a Josephson junction based on HgTe, a 3D topological insulator and observe a missing $n = 1$ Shapiro step in $I-V$ characteristic. This could

be explained by the presence of a 4π-periodic supercurrent, e.g. the fractional Josephson effect.

3.6 DISCUSSION

The experiments Refs. [64, 81, 103] are in qualitative agreement with theoretical proposals for the emergence of Majorana fermions, yet not fully consistent with the predicted values of the conductance, the required values of the magnetic field for topological phase transition and the absence of all odd Shapiro steps. Therefore, zero-bias peaks obtained in transport experiments can be caused by other physical processes, such as disorder [5, 57], weak antilocalization [75] or Kondo effect [52].

Cavity QED, discussed in chapter 2, offers an alternative approach to probe the signatures of Majorana fermions in topological wires by using the photonic field in the cavity. Several theoretical works study the interplay of the Majorana fermions physics and microwaves in a superconducting cavity QED setup [22, 65, 69, 70, 88, 89, 96, 105]. In contrast to the conventional electronic methods, this approach is unique in that it can be totally non-invasive, i.e. it does not alter the electronic system, a crucial feature in view of using these excitations for quantum computing. However, most studies concentrate on effective models that consider *only* the Majorana fermions interacting with the cavity field, which cannot account for the evolution of the Majorana fermions through the topological transition from a topological to a trivial superconductor. More specifically, the Majorana fermions emerge as edge modes in a topological superconductor: below the phase transition, the system is topological and shows edge modes, while above the phase transition, the system is trivial and has no edge modes. Majorana fermions are thus closely related to the bulk physics. We consider the whole system in chapter 5.

4

OUT-OF-EQUILIBRIUM QUANTUM DOT COUPLED TO A MICROWAVE CAVITY

In this chapter, we apply the cavity QED approach described in chapter 2 to study two mesoscopic conductors: a tunnel junction and a quantum dot tunnel coupled to metallic leads. We demonstrate that the measurement of the optical transmission coefficient which is related to the charge susceptibility can be used to extract information on the transport properties of the quantum dot. We show that the asymmetry of the capacitive couplings between the electronic reservoirs and the cavity plays a crucial role in relating optical observables to transport ones. In particular, we found that when the quantum dot is far from resonance, the charge susceptibility is directly proportional to the admittance. However, when the quantum dot is near a resonance, such a relation generally holds only for the symmetric couplings between the leads and the cavity, at low frequency and for equal tunnel coupling or low voltage. Beyond this low-energy near equilibrium regime, the charge susceptibility offers new insights on the quantum conductors since the optical observables are not directly connected to transport quantities. For symmetric lead capacitive couplings, we show that the optical measurements can be used to reveal the Korringa-Shiba relation, connecting the reactive to the dissipative part of the susceptibility, at low frequency and low bias.

4.1 MODEL HAMILTONIAN

Our system, depicted in Fig. 4.1, consists of a quantum dot that is tunnel coupled to metallic leads. Both the quantum dot and the leads are capacitively coupled to a (superconducting) microwave cavity. We assume that the wavelength of the electromagnetic field (~mm) is much larger than the mesoscopic system (~μm), and thus the coupling is con-

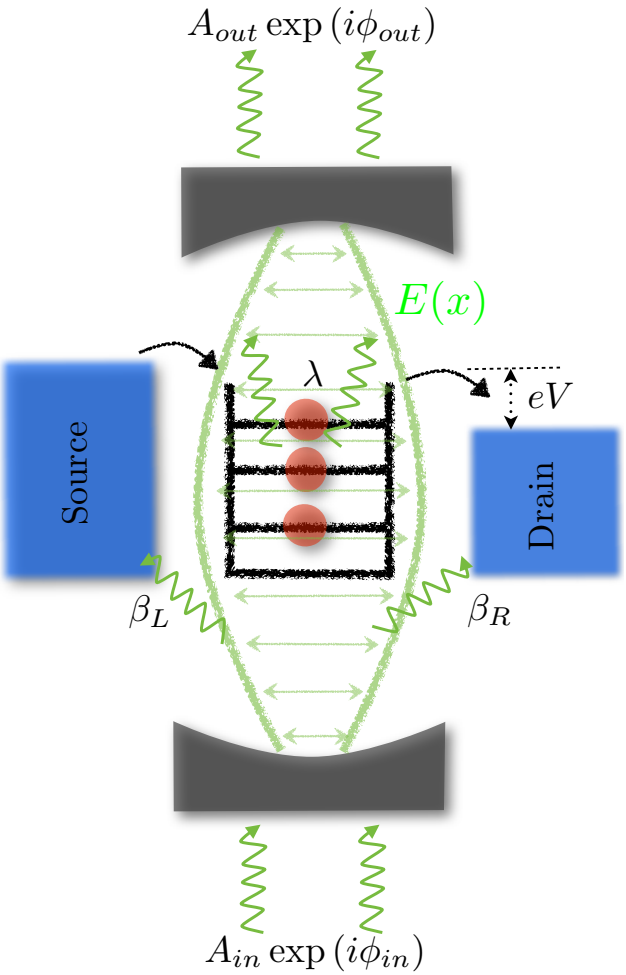

Figure 4.1: Sketch of the system. The quantum dot with discrete energy levels (in black) is coupled to the source and drain electrodes (blue), which have a voltage bias eV. Differential conductance of the system may be found by transport measurements. The entire setup is coupled to the microwave cavity (depicted as light between two mirrors; mirrors in gray). The photons are coupled to the left lead with coupling strength β_L, to the right lead with β_R and to the dot with λ. The electromagnetic field inside the cavity is probed by sending input field with amplitude A_{in} and phase ϕ_{in} and measuring the output field with A_{out} and ϕ_{out}. The difference between the outgoing and ingoing fields gives direct access to the charge susceptibility of the electronic system (see text).

stant over its length. The cavity supports many (in principle, infinitely many) modes, all

of which should couple to the system. However, only cavity modes resonant with some electronic modes are relevant, the others giving negligible effect. From here on, we assume that only one mode, e.g. the lowest, couples to the system. Nevertheless, our analysis can be straightforwardly extended to a multimode cavity. We analyze the optical transmission and its relation to various observables of the mesoscopic system. We consider both the equilibrium and out-of-equilibrium situations where the voltage bias is large.

The Hamiltonian of the combined system reads:

$$H_{sys} = H_{el} + H_{el-c} + H_{ph}\,, \tag{4.1}$$

$$H_{el} = \epsilon_d d^\dagger d + \sum_{k\alpha} \left(t_\alpha c^\dagger_{k\alpha} d + h.c. \right) + \sum_{k\alpha} \epsilon_{k\alpha} c^\dagger_{k\alpha} c_{k\alpha}\,, \tag{4.2}$$

$$H_{el-c} = \lambda(a + a^\dagger) d^\dagger d + (a + a^\dagger) \sum_{k\alpha} \beta_\alpha c^\dagger_{k\alpha} c_{k\alpha}\,, \tag{4.3}$$

and $H_{ph} = \omega_c a^\dagger a$. In these equations, $c_{k\alpha}$ ($c^\dagger_{k\alpha}$) is the annihilation (creation) operator of an electron in the left (right) lead $\alpha = L(R)$ with momentum k; d ($d^\dagger$) is the annihilation (creation) operator of an electron in the quantum dot; a ($a^\dagger$) is the annihilation (creation) operator of the photon field. We denote the energy level of the quantum dot as ϵ_d, the tunneling amplitude between the quantum dot and the lead α as t_α, and the cavity mode frequency as ω_c. Finally, λ and β_α are the electron-photon coupling constants to the quantum dot, and the lead $\alpha = L, R$, respectively. Note that we include the capacitive coupling between the quantum dot and the cavity as well as between the cavity and the electronic reservoirs. We have neglected direct photon-induced tunneling terms in the Hamiltonian which are subleading compared to capacitive couplings terms [23]. A general expression for the coupling constants λ and β_α is given in Ref. [23], involving an integral over the spatial variation of the vector potential in the corresponding part of the conductor, lead or quantum dot. The result depends on the geometry of the device and there is no general argument to favor λ over β_α (or the opposite) in the general case.

4.2 ELECTRONIC CHARGE SUSCEPTIBILITY

4.2.1 *General relations obeyed by transport quantities*

According to Eq. 2.40, the weak coupling between the cavity and the electronic system results in the modification of the transmission coefficient τ in the linear response regime [36] (see chapter 2 for a derivation of τ). In the time domain, the correlation function $\Pi(\omega)$ reads

$$\begin{aligned}\Pi(t-t') = &-i\theta(t-t')\langle\Big[\left(\lambda n_d+\beta_L n_L+\beta_R n_R\right)(t),\\ &\left(\lambda n_d+\beta_L n_L+\beta_R n_R\right)(t')\Big]\rangle,\end{aligned} \tag{4.4}$$

which corresponds to the total charge susceptibility of the electronic system capacitively coupled to the cavity, where $n_d = d^\dagger d$ is the number operator for electrons in the dot and $n_\alpha = \sum_k c^\dagger_{k\alpha} c_{k\alpha}$ is the number operator of electrons in the lead α.

Using the fact that total charge is conserved, $n_d + n_L + n_R = N$, with N proportional to the total charge operator commuting with H_{sys}, the susceptibility in Eq.4.4 can be rewritten as

$$\begin{aligned}\Pi\left(t-t'\right) &= \left(\beta_L-\lambda\right)^2\Pi_{LL}\left(t-t'\right)+\left(\beta_R-\lambda\right)^2\Pi_{RR}\left(t-t'\right)\\ &+\left(\beta_L-\lambda\right)\left(\beta_R-\lambda\right)\left[\Pi_{LR}\left(t-t'\right)+\Pi_{RL}\left(t-t'\right)\right],\end{aligned} \tag{4.5}$$

where we introduced

$$\Pi_{\alpha\beta}\left(t-t'\right) = -i\theta(t-t')\langle\left[n_\alpha(t), n_\beta\left(t'\right)\right]\rangle. \tag{4.6}$$

Using the equation of motion techniques, we can write

$$\begin{aligned}i\partial_t\Pi_{\alpha\beta}\left(t-t'\right) &= \delta(t-t')\langle\left[n_\alpha(t), n_\beta\left(t'\right)\right]\rangle\\ &+\theta(t-t')\langle\left[I_\alpha(t), n_\beta\left(t'\right)\right]\rangle/e,\end{aligned} \tag{4.7}$$

where

$$I_\alpha = e\frac{dn_\alpha(t)}{dt} \tag{4.8}$$

is the current operator. Let us introduce the correlation function

$$Y_{\alpha\beta}(t,t') = -i\theta(t-t')\langle[I_\alpha(t), n_\beta(t')]\rangle, \tag{4.9}$$

which may be interpreted as an admittance or as a generalized non-equilibrium differential conductance (see *e.g.* [83] with an opposite sign in the definition). Note that Y depends on the voltage bias V although it is not immediately visible from Eq. (4.9). Using Eq. (4.7) and Eq. (4.9) we find the following relations between the susceptibility and the generalized differential conductance in Fourier space :

$$\Pi_{\alpha\alpha}(\omega) = \frac{i}{e\omega}Y_{\alpha\alpha}(\omega), \tag{4.10}$$

$$\Pi_{LR}(\omega) + \Pi_{RL}(\omega) = \frac{i}{e\omega}\left[Y_{LR}(\omega) + Y_{RL}(\omega)\right]. \tag{4.11}$$

From Eqs (4.10) and (4.11), we can relate $\Pi(\omega)$ defined in Eq. (4.4) to a linear combination of the admittances. Such linear combination may be simplified in some limiting case as follows. For example, let us assume that there is no charge fluctuation in the quantum dot so that $n_d(t) \approx const$ in the cavity frequency range of interest. In this limit,

$$\Pi(\omega) \approx \frac{i}{e\omega}(\beta_L - \beta_R)^2 Y(\omega), \tag{4.12}$$

where $Y = Y_{LL} = Y_{RR} = -Y_{LR} = -Y_{RL}$. $\Pi(\omega)$ is non-zero only for asymmetric couplings to the leads, $\beta_L \neq \beta_R$. The prediction of Eq. (4.12) is quite intuitive: the cavity electric field shakes the electrons in the reservoirs asymmetrically and therefore probes the admittance of the whole system. Eq. (4.12) also implies that the imaginary part of $\Pi(\omega)$ measured via the cavity resonance broadening is proportional to the real part of the admittance, which, at low frequency, reduces to the differential conductance. Thus the charge freez-

ing limit $n_d(t) \approx const$ is a particular case where the optical transmission coefficient directly measures the non-equilibrium admittance of the system. Charge freezing can be obtained by replacing the quantum dot by an insulating barrier, by tuning the dot level far off-resonance, or by considering an interacting quantum dot in the Kondo regime as in Ref. [29]. We discuss this situation at the end of section 4.4.

Introducing the non-symmetrized noise at finite frequency at

$$C_{\alpha\beta}(\omega) = \int_{-\infty}^{\infty} dt \exp(i\omega t)\langle I_\alpha(t) I_\beta(0)\rangle, \tag{4.13}$$

the admittance $Y_{\alpha\alpha}(\omega)$ can be related to the current-current correlator [83] through

$$C_{\alpha\alpha}(\omega) - C_{\alpha\alpha}(-\omega) = -2\omega e Y'_{\alpha\alpha}(\omega). \tag{4.14}$$

The first term on the left hand side of Eq. (4.14) corresponds to the emission noise and the second term corresponds to the absorption noise. Hence Eq. (4.14) directly relates the increase in the cavity resonance broadening to the balance between the emission and absorption noise resulting from photon exchange between the quantum conductor and the cavity [61].

4.2.2 *Calculation of the electronic susceptibility*

In order to calculate the components of the total charge susceptibility introduced in Eq. (4.6), we use the scattering formalism that is well suited for such non-interacting problems. In this formalism, the current operator $I_\alpha(t)$ [12, 82] can be written as

$$\begin{aligned} I_\alpha(t) = \frac{e}{2\pi} \int_{-\infty}^{\infty} dE \int_{-\infty}^{\infty} dE' \exp\left(i(E-E')t\right) \\ \times \sum_{\gamma\gamma'} A_{\gamma\gamma'}(\alpha, E, E') a^\dagger_\gamma(E) a_{\gamma'}(E'), \end{aligned} \tag{4.15}$$

where

$$A_{\gamma\gamma'}(\alpha, E, E') = \delta_{\alpha\gamma'}\delta_{\alpha\gamma} - S^*_{\alpha\gamma}(E)S_{\alpha\gamma'}(E'). \tag{4.16}$$

In Eq. (4.16), $S_{\alpha\gamma}(E)$ are the elements of the scattering matrix characterizing the system (tunnel junction, quantum dot, etc.). The current operator I_α is expressed in terms of annihilation (creation) $a_\alpha(E)$ ($a^\dagger_\alpha(E)$) operators of the electrons in the reservoir connected to terminal α. These operators are normalized so that

$$\langle a^\dagger_\alpha(E)a_{\alpha'}(E')\rangle = \delta_{\alpha\alpha'}\delta(E-E')f_\alpha(E), \tag{4.17}$$

where $f_\alpha(E) = [\exp(E-\mu_\alpha)/k_BT + 1]^{-1}$ denotes the Fermi function in the lead α and μ_α is its chemical potential.

The Fourier transform of $I_\alpha(t)$ reads:

$$I_\alpha(\omega) = e\int_{-\infty}^{\infty} dE \sum_{\gamma\gamma'} A_{\gamma\gamma'}(\alpha, E, E+\omega)a^\dagger_\gamma(E)a_{\gamma'}(E+\omega). \tag{4.18}$$

Using

$$n_\alpha(t) = \frac{i}{2\pi e}\int_{-\infty}^{\infty} d\omega \exp(-i\omega t)\frac{I_\alpha(\omega)}{\omega} \tag{4.19}$$

and Eq. (4.18), we can express the number operator as

$$\begin{aligned} n_\alpha(t) = \frac{i}{2\pi}\int_{-\infty}^{\infty} d\omega \exp(-i\omega t)\frac{1}{\omega} \\ \times \int_{-\infty}^{\infty} dE \sum_{\gamma\gamma'} A_{\gamma\gamma'}(\alpha, E, E+\omega)a^\dagger_\gamma(E)a_{\gamma'}(E+\omega). \end{aligned} \tag{4.20}$$

Performing manipulations detailed in the appendix B.1, we can rewrite $\Pi_{\alpha\beta}$ as

$$\Pi_{\alpha\beta}(\omega) = \left(\frac{1}{2\pi}\right)^2 \int_{-\infty}^{\infty}\int_{-\infty}^{\infty} d\omega_2 dE_2 \Bigg\{ \frac{1}{\omega_2^2}\frac{1}{\omega+\omega_2+i\eta} \times \sum_{\gamma_1,\gamma_1'} F^{\alpha\beta}_{\gamma_1\gamma_1'}(E_2,\omega_2)\left[f_{\gamma_1}(E_2+\omega_2) - f_{\gamma_1'}(E_2)\right]\Bigg\}, \tag{4.21}$$

where we introduced a new function

$$F^{\alpha\beta}_{\gamma\gamma'} = A_{\gamma\gamma'}(\alpha, E+\omega, E) A_{\gamma'\gamma}(\beta, E, E+\omega). \tag{4.22}$$

At zero temperature ($T = 0$), this expression can be simplified further. Introducing the integrals

$$\begin{aligned} K_{\alpha\beta}(\omega_2) = &\int_{eV/2}^{eV/2-\omega_2} dE_2 F^{\alpha\beta}_{LL}(E_2,\omega_2) \\ &+ \int_{-eV/2}^{-eV/2-\omega_2} dE_2 F^{\alpha\beta}_{RR}(E_2,\omega_2) \\ &+ \int_{-eV/2}^{eV/2-\omega_2} dE_2 F^{\alpha\beta}_{LR}(E_2,\omega_2) \\ &+ \int_{eV/2}^{-eV/2-\omega_2} dE_2 F^{\alpha\beta}_{RL}(E_2,\omega_2), \end{aligned} \tag{4.23}$$

the real and imaginary part of the susceptibility can be written as

$$\Pi'_{\alpha\beta}(\omega) = \left(\frac{1}{2\pi}\right)^2 \mathcal{P}\int_{-\infty}^{\infty} d\omega_2 \frac{1}{\omega_2^2}\frac{1}{\omega+\omega_2} K_{\alpha\beta}(\omega_2), \tag{4.24}$$

$$\Pi''_{\alpha\beta}(\omega) = -\frac{\pi}{(2\pi\omega)^2} K_{\alpha\beta}(-\omega). \tag{4.25}$$

In order to compute the susceptibility $\Pi_{\alpha\beta}$ for a non-interacting scatterer in question, we first need to compute the functions $F^{\alpha\beta}_{\gamma\gamma'}$ in Eq. (4.22), and then the functions $K_{\alpha\beta}$ in

Eq. (4.23). In the next section, we present these computations for a simpler system – the tunnel junction, – and we analyze a more complex quantum dot system in section .

4.3 TUNNEL JUNCTION

4.3.1 *Cavity pull and dissipation*

The Hamiltonian that combines the resonating cavity with the tunnel junction has the form of Eq. (4.1) with

$$H_{el} = \sum_{k\alpha} \epsilon_{k\alpha} c^\dagger_{k\alpha} c_{k\alpha} + \sum_{kq} \left(t c^\dagger_{kR} c_{qL} + h.c. \right) \tag{4.26}$$

and

$$H_{el-c} = (a + a^\dagger) \sum_{k\alpha} \beta_\alpha c^\dagger_{k\alpha} c_{k\alpha} \,, \tag{4.27}$$

characterized by the capacitive coupling β_L (β_R) of the left (right) lead to the cavity. The tunneling amplitude t being independent of energy is equivalent to instantaneous electron scattering. As a result, no charge can accumulate in the junction, the total charge in the leads $N = n_R + n_L$ is constant, and the current is conserved $I_R = -I_L$. The different charge susceptibilities are related to each other

$$\Pi_{LL}(\omega) = \Pi_{RR}(\omega) = -\Pi_{LR}(\omega) = -\Pi_{RL}(\omega) \tag{4.28}$$

so that the total electronic susceptibility in Eq. 2.40 reads

$$\Pi(\omega) = \sum_{\alpha,\gamma} \beta_\alpha \beta_\gamma \Pi_{\alpha\gamma}(\omega) = (\beta_L - \beta_R)^2 \Pi_{LL}(\omega), \tag{4.29}$$

as in Eq. (4.12). The dependence on the coupling difference $\beta_L - \beta_R$ may be also viewed as a consequence of gauge invariance as discussed in section. 4.3.2.

Using the scattering formalism of section 4.2, we can compute the electronic susceptibility for the tunnel junction. The scattering matrix is energy independent and takes the form

$$S = \begin{pmatrix} ir & t \\ t & ir \end{pmatrix}, \tag{4.30}$$

where unitarity implies $r^2 + t^2 = 1$ (we choose real parameters for simplicity). The functions introduced in Eq. (4.22) are then expressed as $F_{LL}^{\alpha\beta} = F_{RR}^{\alpha\beta} = \varepsilon_{\alpha\beta} T^2$ and $F_{LR}^{\alpha\beta} = F_{RL}^{\alpha\beta} = \varepsilon_{\alpha\beta} T(1-T)$, where $T = t^2$ is the tunnel junction transmission, $\varepsilon_{\alpha\beta} = 1$ if $\alpha = \beta$ and -1 otherwise. Inserting these expressions in Eq. (4.23), we obtain

$$K_{\alpha\beta}(\omega_2) = -2T\omega_2 \, \varepsilon_{\alpha\beta}. \tag{4.31}$$

Even at this level one may observe that the photonic transmission is not affected by the bias voltage V. This is due to the linearity in the I-V characteristic of the tunnel junction.

Integrating Eq. (4.24)

$$P\int_{-\infty}^{\infty} \frac{d\omega_2}{\omega_2(\omega + \omega_2)} = 0, \tag{4.32}$$

we find that the real part of the susceptibility becomes zero, $\Pi'_{\alpha\beta} = 0$, hence the absence of the cavity pull. This result is in agreement with Ref. [61] where a different gauge was used, corresponding to the Eq. (4.35) derived in the next subsection. Therefore, any shift in the cavity resonant frequency is due to either a weak energy dependence in the electronic transmission or to higher order effects (backaction) in the electron-photon coupling. The imaginary part is obtained from Eq. (4.25) and reads $\Pi''_{\alpha\beta}(\omega) = -(T/2\pi\omega)\, \varepsilon_{\alpha\beta}$ recovering the current conservation in Eq. (4.28). Finally, the total susceptibility of the tunnel junction

$$\Pi(\omega) = -i(\beta_L - \beta_R)^2 \frac{T}{2\pi\omega} \tag{4.33}$$

corresponds to a purely dissipative effect of the electrons on the photonic transmission. This expression can be also obtained by computing the admittance $Y(\omega)$ and using Eq. (4.12). For the tunnel junction, the admittance $Y(\omega)$ does not depend on neither the frequency ω nor the voltage V. It is equal to the linear conductance $G = \frac{\partial I}{\partial V}$.

4.3.2 *Gauge invariance*

Different choices of gauge are possible to describe the same system. They are related to each other via unitary transformations. In order to relate to the previous work, we discuss below two other gauges.

The first unitary transformation is given by the displacement operator $U_1 = e^{(\beta_R/\omega_c)n(a^\dagger - a)}$, shifting the photon field $a \to a - (\beta_R/\omega_c)n$. The operator U_1 does not affect the dynamics of electrons since the total number of electrons $n = n_R + n_L$ commutes with the Hamiltonian, hence $U_1 H_{el} U_1^\dagger = H_{el}$. The operator U_1 substracts β_R from the capacitive couplings thereby canceling the coupling to the right lead. More specifically, the transformed Hamiltonian is given by

$$U_1(H_{ph} + H_{el-c})U_1^\dagger = \omega_c a^\dagger a + (a + a^\dagger)(\beta_L - \beta_R)n_L - \frac{\beta_R\beta_L}{\omega_c}n^2 - \frac{\beta_R(\beta_L - \beta_R)}{\omega_c}n(n_L - n_R). \tag{4.34}$$

The first two terms describe the single mode resonator and its coupling to the left lead. The second term particularly emphasizes the sensitivity of the photon transmission to the capacitive inhomogeneity $\beta_L - \beta_R$. Since n commutes with the total Hamiltonian, the third term is a constant and the last term describes an additional small bias voltage. The result of Eq. (4.33) may be obtained from Eq. (4.34) straightforwardly.

The second unitary transformation removes the linear coupling between the cavity and the electrons, i.e. Eq. (4.27), by dressing the tunneling amplitude between the two leads.

This transformation with the unitary operator $U_2 = e^{A(a^\dagger - a)}$, with $\omega_c A = \beta_L n_L + \beta_R n_R$, transforms the Hamiltonian into

$$H' = U_2 H U_2^\dagger = \sum_{kq} \left(t e^{(\beta_R - \beta_L)(a^\dagger - a)/\omega_c} c_{kR}^\dagger c_{qL} + \text{h.c.} \right) + \sum_{k\alpha} \epsilon_{k\alpha} c_{k\alpha}^\dagger c_{k\alpha} + \omega_c a^\dagger a - \frac{A^2}{\omega_c}. \tag{4.35}$$

The last term in this expression A^2/ω_c describes capacitive electron-electron interaction across the tunnel junction and is usually neglected.

We remark that the different gauges correspond to shifted positions of the resonator vacuum. A vacuum in one gauge is different from the vacuum in another gauge.

4.4 QUANTUM DOT

Let us determine the charge susceptibility probed by the microwave cavity of the QD tunnel coupled to metallic leads and capacitively coupled to the microwave cavity. The scattering matrix for the single-level quantum dot reads

$$S(E) = -1 + i g(E) \begin{pmatrix} \Gamma_L & \sqrt{\Gamma_L \Gamma_R} \\ \sqrt{\Gamma_L \Gamma_R} & \Gamma_R \end{pmatrix}, \tag{4.36}$$

where

$$g(E) = \frac{1}{E - \epsilon_d + i\Gamma/2}, \tag{4.37}$$

and $\Gamma = \Gamma_L + \Gamma_R$ is the width of the level. Using this expression for the S-matrix we can compute the functions $A_{\gamma\gamma'}(\alpha, E, E')$ defined in Eq. (4.16), then the sixteen functions $F_{\gamma\gamma'}^{\alpha\beta}$ introduced in Eq. (4.22), and finally the functions $K_{\alpha\beta}(\omega)$ defined in Eq. (4.23). Being lengthy and not essential for further discussion, the intermediate expressions for the functions $F_{\gamma\gamma'}^{\alpha\beta}$, and $K_{\alpha\beta}(\omega)$ are given in Appendix []. The functions $K_{\alpha\beta}$ directly provide $\Pi''_{\alpha\beta}$ through Eq. (4.25). However, in order to obtain $\Pi'_{\alpha\beta}$, we need to perform a final tedious

integration over energy in Eq. (4.24), the details of which are given in the Appendix B.2. The final expressions for the real and imaginary parts of the total susceptibility are given in Eq. (B.48) and Eq. (B.49), respectively, of the Appendix B.2. However, such expressions are intricate and difficult to interpret directly. Therefore, we consider some limiting cases where simple expressions and conclusions can be obtained before addressing the general case.

4.4.1 *The Quantum RC-circuit limit*

For the two following limits (or sets of parameters) our system reduces to the so-called quantum RC circuit, which has been largely studied theoretically[15, 23, 39, 53, 63, 67] as well as implemented and verified experimentally [14, 38, 44].

Case $\Gamma_R = 0$

This case corresponds to a quantum dot connected to a single reservoir by a junction. The quantum RC circuit is particularly interesting in the small frequency limit when some universal behavior is expected [63, 67] and was observed [14].

When ω is smaller than all other energy scales at play, we can further simplify the expression of the susceptibility $\Pi(\omega)$ to obtain

$$\Pi'(\omega) = -\frac{2\Gamma_L(\beta_L - \lambda)^2}{\pi\left(\Gamma_L^2 + 4\epsilon_d^2\right)} + O(\omega^2)\,, \tag{4.38}$$

for the real part, and

$$\Pi''(\omega) = -\frac{4\Gamma_L^2\omega(\beta_L - \lambda)^2}{\pi\left(\Gamma_L^2 + 4\epsilon_d^2\right)^2} + O(\omega^3)\,, \tag{4.39}$$

for the imaginary part. Note that these expressions correspond exactly to $\Delta\omega_0^a$ and $\Delta\Lambda_0$ in Ref. [23] with $\Gamma = \Gamma_L/2$ [up to a minus sign which can be traced back to our different definition of $\Pi(t)$ in Eq. (4.4)].

The real and imaginary contributions, Π' and Π'', respectively, are not independent and fulfill at the lowest order in ω the following relation

$$\Pi''(\omega) = -\pi\omega \left[\Pi'(0)\right]^2 / (\lambda - \beta_L)^2. \tag{4.40}$$

Up to the electron-photon couplings, this is nothing but the Korringa-Shiba relation connecting the dissipative part of the susceptibility to its reactive part. Note that we defined the correlation function $\Pi(t)$ in Eq. (4.4) with a different sign compared to, e.g., Ref. [63], and thus introduced the opposite sign in the Korringa-Shiba relation. Note that the use of a microwave cavity for verifying the Korringa-Shiba relation has first been proposed in Ref. [23].

Case $\beta_L = \beta_R$

For equal capacitive coupling to the leads ($\beta_L = \beta_R$), the cavity electric field effectively couples to a single larger lead as well as to the quantum dot. We thus expect to observe the same physics as in the previous case. Again, we assume ω to be smaller than the other energy scales in the system.

In this low-frequency limit, the real part of the total susceptibility Π reads

$$\begin{aligned}\Pi'(\omega) = &- \frac{2(\lambda - \beta_L)^2}{\pi} \left[\frac{\Gamma_L}{(eV - 2\epsilon_d)^2 + \Gamma^2} \right. \\ &\left. + \frac{\Gamma_R}{(eV + 2\epsilon_d)^2 + \Gamma^2} \right] + O(\omega^2), \end{aligned} \tag{4.41}$$

while the imaginary part reads

$$\Pi''(\omega) = -\frac{4\Gamma\omega\,(\lambda-\beta_L)^2}{\pi}\left[\frac{\Gamma_L}{\left((eV-2\epsilon_d)^2+\Gamma^2\right)^2} + \frac{\Gamma_R}{\left((eV+2\epsilon_d)^2+\Gamma^2\right)^2}\right] + O(\omega^3). \tag{4.42}$$

For zero bias voltage $eV = 0$, one recovers the Korringa-Shiba relation Eq. (4.40). Indeed, the two leads combine and the quantum dot effectively couples to a single lead.

In the latter case ($\beta_L = \beta_R$), given that $eV = 0$, as well as in the former case ($\Gamma_R = 0, eV = 0$), the cavity measures only local charge fluctuations on the dot – leading to the dissipation channel fulfilling the Korringa-Shiba relation, – but it is not sensitive to the charge transfer across the quantum dot.

4.4.2 *The tunneling limit*, $\epsilon_d/\Gamma \to -\infty$

The transmission coefficient for the quantum dot, T_d, in the tunneling limit ($\epsilon_d \to -\infty$) reads

$$T_d = \frac{\Gamma_L\Gamma_R}{\epsilon_d^2}. \tag{4.43}$$

Using this equation, we can immediately evaluate the real and imaginary parts of Π:

$$\Pi'(\omega) = -\frac{T_d}{2\pi}\left[\frac{(\beta_L-\lambda)^2}{\Gamma_R} + \frac{(\beta_R-\lambda)^2}{\Gamma_L} + (\beta_L-\lambda)(\beta_R-\lambda)\left(\frac{1}{\Gamma_L}+\frac{1}{\Gamma_R}\right)T_d\right], \tag{4.44}$$

$$\Pi''(\omega) = -\frac{T_d}{2\pi\omega}(\beta_L-\beta_R)^2. \tag{4.45}$$

The imaginary part of the susceptibility of the QD, related to $\delta A/A$, Eq. (4.45), is equal to the susceptibility of the tunnel junction in Eq. (4.33). The real part of the susceptibility of the QD, related to the phase shift $\delta\phi$, is not zero as opposed to the tunnel junction result. The non-zero phase shift for the QD is explained by the existence of a localized level inside the barrier which is coupled virtually to the continuum of levels in the leads by the cavity field. On the other hand, such level is absent in a pure tunnel junction resulting in the zero real part of the susceptibility.

4.4.3 *The low-frequency limit*

Let us explore in detail the low-frequency regime when the cavity frequency is typically smaller than the electronic quantum dot resonance width, $\omega \ll \Gamma$. This regime is studied experimentally in [29].

In this limit, one can take a series in ω/Γ of both the real and imaginary parts of the charge susceptibility:

$$\Pi'_{\alpha\beta}(\omega) = \Pi'_{\alpha\beta}(0) + O(\omega^2), \tag{4.46}$$

$$\Pi''_{\alpha\beta}(\omega) = \frac{1}{\pi\omega}\Lambda^{(-1)}_{\alpha\beta} + \omega\Lambda^{(1)}_{\alpha\beta} + O(\omega^3). \tag{4.47}$$

We obtain the following expressions for the lowest order terms.

$$\Pi'_{LL,RR}(0) = -\frac{2\Gamma_{L,R}\left[(eV \mp 2\epsilon_d)^2 \pm (\Gamma_L^2 - \Gamma_R^2)\right]}{\pi\left[(eV \mp 2\epsilon_d)^2 + \Gamma^2\right]^2}, \tag{4.48}$$

$$\Pi'_{LR}(0) + \Pi'_{RL}(0) = -\frac{4\Gamma\Gamma_L\Gamma_R}{\pi} \times \left[\frac{1}{\left((eV - 2\epsilon_d)^2 + \Gamma^2\right)^2} + \frac{1}{\left((eV + 2\epsilon_d)^2 + \Gamma^2\right)^2}\right]. \tag{4.49}$$

And similarly

$$\Lambda^{(-1)}_{LL,RR} = -\frac{2\Gamma_L\Gamma_R}{\left[(eV \mp 2\epsilon_d)^2 + \Gamma^2\right]}, \tag{4.50}$$

$$\Lambda^{(-1)}_{LR} + \Lambda^{(-1)}_{RL} = 2\Gamma_L\Gamma_R \times \\ \times \left[\frac{1}{(eV - 2\epsilon_d)^2 + \Gamma^2} + \frac{1}{(eV + 2\epsilon_d)^2 + \Gamma^2}\right]. \tag{4.51}$$

The expressions for $\Lambda^{(1)}_{\alpha\beta}$ read:

$$\Lambda^{(1)}_{LL,RR} = -\frac{4\Gamma_{L,R}}{3\pi\left[(eV \mp 2\epsilon_d)^2 + \Gamma^2\right]^3} \times \\ \left[(3\Gamma_{L,R} - 2\Gamma_{R,L})\Gamma^2 + 3(\Gamma + \Gamma_{R,L})(eV \mp 2\epsilon_d)^2\right], \tag{4.52}$$

and

$$\Lambda^{(1)}_{LR} + \Lambda^{(1)}_{RL} = -\frac{4\Gamma_L\Gamma_R}{3\pi}\left[\frac{5\Gamma^2 - 3(eV - 2\epsilon_d)^2}{\left[(eV - 2\epsilon_d)^2 + \Gamma^2\right]^3} \right. \\ \left. + \frac{5\Gamma^2 - 3(eV + 2\epsilon_d)^2}{\left[(eV + 2\epsilon_d)^2 + \Gamma^2\right]^3}\right]. \tag{4.53}$$

Analyzing these equations, one may observe that both the real and imaginary parts of the susceptibility $\Pi_{\alpha\beta}(\omega)$ have peaks at $\epsilon_d = \pm eV/2$. Noticing that $\Lambda^{(-1)}_{LL} + \Lambda^{(-1)}_{RR} + \Lambda^{(-1)}_{LR} + \Lambda^{(-1)}_{RL} = 0$, we can further simplify the expression for $\Pi''(\omega)$ as

$$\begin{aligned}\Pi''(\omega) =& \frac{(\beta_L - \beta_R)}{\pi\omega}\left[(\beta_L - \lambda)\Lambda^{(-1)}_{LL} - (\beta_R - \lambda)\Lambda^{(-1)}_{RR}\right] \\ &+ \omega\left[(\beta_L - \lambda)^2\Lambda^{(1)}_{LL} + (\beta_R - \lambda)^2\Lambda^{(1)}_{RR}\right. \\ &\left. + (\beta_L - \lambda)(\beta_R - \lambda)(\Lambda^{(1)}_{LR} + \Lambda^{(1)}_{RL})\right] . \end{aligned} \tag{4.54}$$

Let us discuss both $\beta_L = \beta_R$ and $\beta_L \neq \beta_R$ cases.

Case $\beta_L = \beta_R$

For $\beta_L = \beta_R$, we find again the effective quantum RC circuit case discussed above. In particular, it implies that at $V = 0$,

$$\delta\phi(V = 0) \approx -\frac{2\Gamma(\beta_L - \lambda)^2}{\pi\kappa\left(\Gamma^2 + 4\epsilon_d^2\right)}, \tag{4.55}$$

which corresponds to a Lorenztian shape as a function of the dot gate voltage $\propto \epsilon_d$.

In order to analyze the general non-equilibrium $V \neq 0$ case, we plot in Fig. 4.2 both $\tilde{\Pi}' = \Pi'/(\beta_L - \lambda)^2$ and $\tilde{\Pi}'' = \Pi''/(\beta_L - \lambda)^2$ as functions of ϵ_d and eV. Both the real and imaginary parts of Π have peaks around $eV = 0$. For eV larger than Γ, the peaks split, and resonances are found for $eV/2 = \pm\epsilon_d$. For $\beta_L = \beta_R$, the Korringa-Shiba relations are satisfied at low energy for $V = 0$. This implies that $\Pi'' \propto (\Pi')^2$ and therefore the resonances in Π'' are more narrow at $eV = 0$ than the resonances of Π'.

Let us compare these results to the non-equilibrium differential conductance $G(V) = dI/dV$ across the quantum dot that reads

$$G(V) = \frac{e^2}{2\pi}\left(\frac{2\Gamma_L\Gamma_R}{(eV - 2\epsilon_d)^2 + \Gamma^2} + \frac{2\Gamma_L\Gamma_R}{(eV + 2\epsilon_d)^2 + \Gamma^2}\right). \tag{4.56}$$

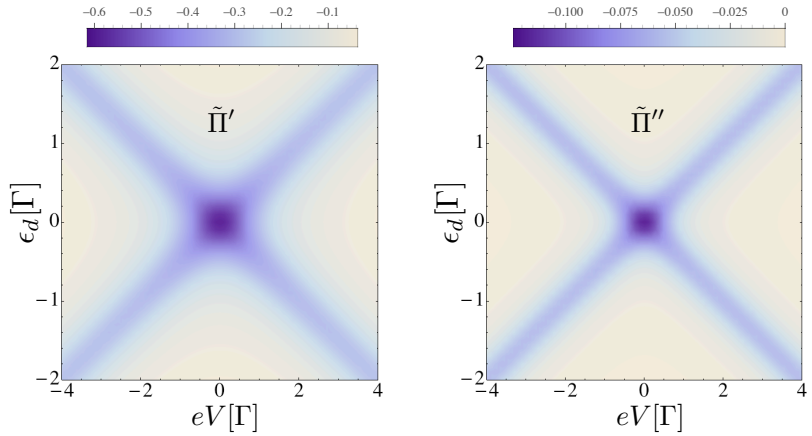

Figure 4.2: $\tilde{\Pi}'(\omega) \equiv \Pi'(\omega)/(\beta_L - \lambda)^2$ (left) and $\tilde{\Pi}''(\omega) \equiv \Pi''/(\beta_L - \lambda)^2$ (right) as a function of eV and ϵ_d for $\beta_L = \beta_R$, $\Gamma_L = \Gamma_R = 0.5$ and $\omega = 0.1$. All energies are expressed in terms of $\Gamma = \Gamma_L + \Gamma_R$.

The differential conductance has a Lorentzian shape double peaked at $eV/2 = \pm\epsilon_d$. Noticing that, for $\Gamma_L = \Gamma_R$, the expression of $\Pi'(\omega, V)$ given in Eq. (4.41) is directly proportional to $G(V)$. We thus expect that

$$\delta\phi(V) = -\frac{4(\beta_L - \lambda)^2}{\kappa e^2 \Gamma} G(V), \tag{4.57}$$

for $\Gamma_L = \Gamma_R = \Gamma/2$.

Therefore, for both symmetric tunneling amplitudes and lead capacitive couplings, Eq. (4.57) directly relates the optical phase shift to the non-equilibrium conductance.

For small deviations from the equalities $\Gamma_L = \Gamma_R$ and $\beta_L = \beta_R$, we expect the relation Eq. (4.57) to hold approximately. For strong asymmetric tunneling, even though the expressions for Π' and $G(V)$ are no longer proportional within each other, these two quantities still have a similar shape characterized by Lorentzian peaks around $eV/2 = \pm\epsilon_d$.

Such quantitative comparison cannot be made between Π'' (and therefore $\delta A/A$) and $G(V)$ for $\beta_L = \beta_R$ because the term proportional to $1/\omega$ in the series for $\Pi''(\omega)$ is exactly zero. However, small deviations of the stringent condition $\beta_L = \beta_R$ may allow comparing these quantities as we show next.

Case $\beta_L \neq \beta_R$

In the more general case $\beta_L \neq \beta_R$, the expression for Π'' simplifies for $eV = 0$ as

$$\Pi''(\omega, V = 0) \approx -\frac{(\beta_L - \beta_R)^2}{2\pi\omega} \frac{4\Gamma_L\Gamma_R}{4\epsilon_d^2 + \Gamma^2} = -\frac{(\beta_L - \beta_R)^2}{2\pi\omega} T_d. \tag{4.58}$$

In this limit, $\Pi''(\omega)$ has the same structure as for the tunnel junction [see Eq. (4.33)]. Hence the frequency broadening

$$\frac{\delta A}{A}(V = 0) \approx -\frac{(\beta_L - \beta_R)^2}{2\pi\omega\kappa} T_d. \tag{4.59}$$

Therefore, the frequency broadening follows the conductance as a function of the dot gate voltage. The $1/\omega$ term in the frequency series for Π'' dominates even for a very small asymmetry of the capacitive couplings. Note that, for $\beta_L \approx \beta_R$, the phase shift is still given approximately by Eq. (4.55) and still has a Lorentzian shape. These equilibrium results (derived for $V = 0$) agree with experimental results obtained in Ref. [29], where the cavity frequency is the smallest energy scale, and a small asymmetry between the capacitive couplings is present.

In order to explore how the susceptibility depends on the bias and dot gate voltage, we introduce $\gamma = (\beta_L - \lambda)/(\beta_R - \lambda)$ such that

$$\frac{\Pi(\omega)}{(\beta_L - \lambda)(\beta_R - \lambda)} = \gamma\Pi_{LL}(\omega) + \frac{\Pi_{RR}(\omega)}{\gamma} + \Pi_{LR}(\omega) + \Pi_{RL}(\omega).$$

We remind that for $|\gamma - 1| \ll 1$, and $\Gamma_L \sim \Gamma_R$, the out-of-equilibrium relation in Eq. (4.57) holds. However, no such relation is present between $\delta A/A$ and $G(V)$ at finite bias.

We plotted both the real and imaginary parts of $\Pi/(\beta_L - \lambda)(\beta_R - \lambda)$ in Fig. 4.3. While Π' has the same structure as in Fig. 4.2, we find that Π'' has a more complicated non-monotonic behavior. This is due to the competition between the $\Pi''_{LL} + \Pi''_{RR}$ and $\Pi''_{LR} + \Pi''_{RL}$ terms having opposite signs, which explains, for example, the saddle point in the vicinity of the point $\epsilon_d = eV = 0$. Therefore, in this limit of large asymmetric capacitive

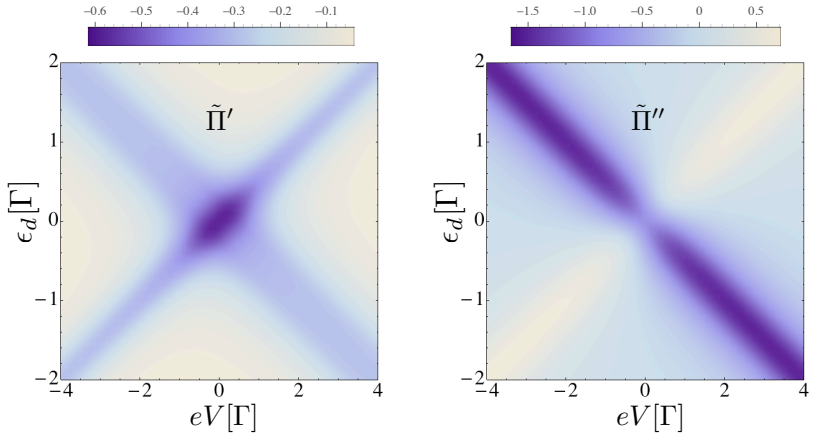

Figure 4.3: $\tilde{\Pi}'(\omega) \equiv \Pi'(\omega)/\gamma\,(\beta_R - \lambda)^2$ (left) and $\tilde{\Pi}''(\omega) \equiv \Pi''/\gamma(\beta_R - \lambda)^2$ (right) as a function of eV and ϵ_d for $\Gamma_L = \Gamma_R = 0.5$, $\gamma = 0.5$, and $\omega = 0.1$. All energies are expressed in terms of $\Gamma = \Gamma_L + \Gamma_R$.

coupling, it is no longer possible to relate $\Pi'' \propto \delta A/A$ to the differential conductance, even qualitatively.

4.4.4 *The general case*

Contrary to the previous section where we explored the low frequency regime with cavity frequency being the smallest scale, we now explore the general case with $\omega \sim \Gamma$ making it impossible to expand Π in frequency series.

Case $\beta_L = \beta_R$

Analyzing the plots of the real and imaginary parts of Π in Fig. 4.4, we observe that Π' has now four peaks in the ϵ_d, eV plane. Compared to the low frequency case, the two lines of resonance at $eV = \pm 2\epsilon_d$ are now split into resonances at positions $eV = \pm 2(\epsilon_d \pm \omega)$. For such large frequency, the cavity acts like a classical AC voltage. Therefore, it modulates the chemical potential of both leads, which corresponds to the photon assisted tunneling

regime. The imaginary part of Π in Fig. 4.4 resembles the one we obtained in the low frequency regime in Fig. 4.2.

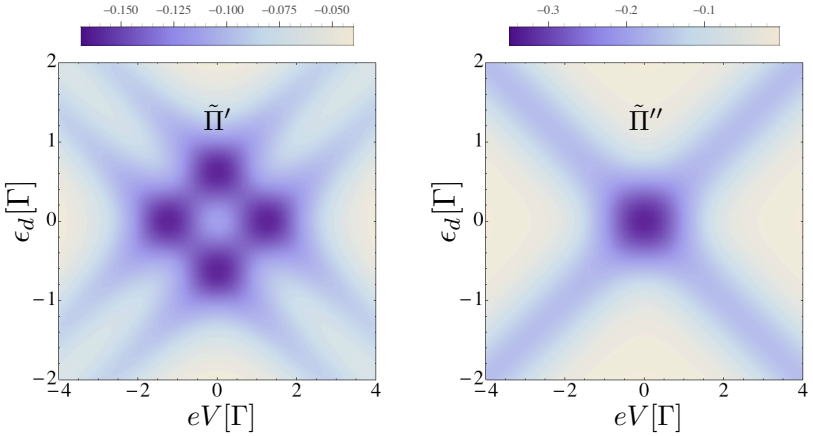

Figure 4.4: Same as Fig. 4.2 for $\omega = 0.8$.

Comparing the resonance lines in both Π' and Π'', we conclude that the Korringa-Shiba relation is violated in this large frequency regime, as expected.

Case $\beta_L \neq \beta_R$

Analyzing plots of the real and imaginary part of Π for an asymmetry parameter $\gamma = 0.5$ in Fig. 4.5, we observe that Π is no longer invariant when $V \to -V$ or $\epsilon_d \to -\epsilon_d$. Let us first focus on the dissipative part Π'. In the small γ limit, we expect $\Pi/(\beta_L - \lambda)(\beta_R - \lambda)$ to be dominated by Π_{RR}. Since the susceptibility is mainly determined by the right reservoir in this limit, we expect the resonance condition $-eV/2 = \epsilon_d$ that occurred at small frequency to become $-eV/2 = \epsilon_d \pm \omega$ at larger frequency. However, the condition $eV/2 = \epsilon_d$ remains unaltered since the charge susceptibility is almost blind to the left reservoir. Already for $\gamma = 0.5$, we can see the aforemetioned features in Fig. 4.5 both for Π' and Π''.

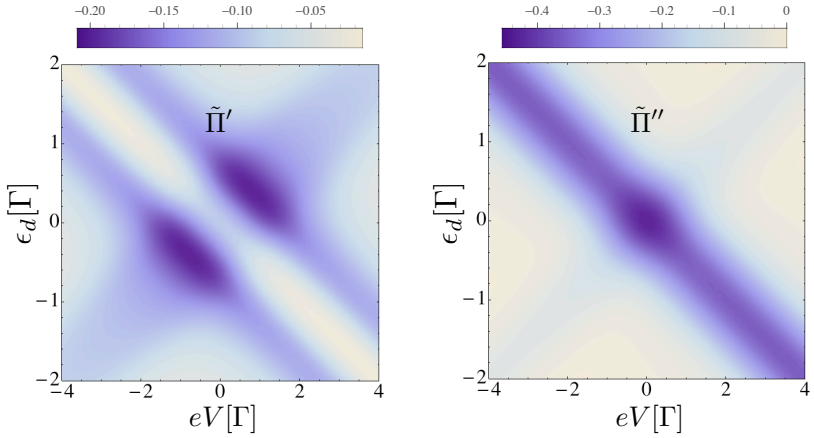

Figure 4.5: Same as Fig. 4.3 with $\omega = 0.8$.

4.4.5 *A quantum dot in the deep Kondo regime*

As mentioned in section 4.2, when the quantum conductor is far from any resonance, the susceptibility and the admittance are related by Eq. (4.12). This relation holds for a non-equilibrium case and does incorporate the bias V. Since ω is usually fixed by the cavity frequency ω_c, $\Pi''(V)$ is proportional to the non-equilibrium differential conductance $Y'(V)$ which is characterized by a Kondo peak around zero bias. Therefore, we expect the dissipative part of the transmission phase shift to be sensitive to this zero bias anomaly. However, in the experimental data of Ref. [29], the phase shift $\delta\phi(V) \propto \Pi'(V)$ was surprisingly shown to exhibit a behavior similar to the differential conductance.

4.5 SUMMARY OF THE RESULTS

We studied a hybrid system consisting of either a tunnel junction or a quantum dot coupled to metallic leads while the whole system itself is coupled to a single mode of a microwave cavity field. We took into account the capacitive coupling between the cavity and the whole electronic system, including the leads. Even for non-interacting conductors, many energy scales characterize the system, for example the cavity frequency, the voltage

bias, the position and width of a resonance and finally the asymmetry of the capacitive couplings.

1. For a tunnel junction with asymmetric capacitive coupling $\beta_L \neq \beta_R$, the imaginary part of the electronic susceptibility $\Pi(\omega)$ is proportional to the admittance $Y(\omega)$ which is equal to the linear conductance dI/dV. Similarly, for a quantum dot far from resonance, therefore characterized by the absence of charge fluctuations, we found that the electronic susceptibility is directly proportional to the quantum dot admittance for all frequency and voltage. The proportionality constant is related to the asymmetry between the lead and cavity capacitive couplings.

2. The case of symmetric capacitive couplings to the leads, $\beta_L = \beta_R$, can be absorbed into a redefinition of the capacitive coupling to the quantum dot.

3. At zero voltage and small frequency, we recover the Korringa-Shiba relation that relates the real and imaginary part of the electronic susceptibility, similarly to the case of a quantum dot connected to a single reservoir (the so-called quantum RC-circuit).

4. In the case of symmetric tunneling amplitudes, $\Gamma_L = \Gamma_R$, we found that the optical phase shift is directly proportional to the differential conductance of the quantum dot for arbitrary bias. This strongly symmetric case thus provides a weakly invasive measurement of the non-equilibrium differential conductance, extracted from the cavity field response. Nevertheless, the lead capacitive couplings have no reason to be equal in general since they depend on the particular geometry of the conductor. They are also hardly tunable.

5. Finally, at zero voltage, we find that the imaginary part of the electronic susceptibility is proportional to the equilibrium zero-frequency admittance.

6. Beyond the above mentioned limits however, the charge susceptibility and the admittance are generally not in correspondance.

4.6 CONCLUSIONS

In this chapter, we studied an electronic system consisting of either a tunnel junction or a quantum dot with metallic leads capacitively coupled to a single mode of electromagnetic resonator. We considered and detailed different cases and our results are summarized in section 4.5. We demonstrated that the asymmetry of the capacitive couplings between the electronic reservoirs and the cavity plays actually a crucial role by rendering the cavity electric field sensitive to charge transfers between two different leads. We found that the cavity field can be used to probe the low finite frequency admittance $Y_{\alpha\beta}$ (where α, β are lead indices) of the electronic system. Beyond the low frequency regime, the charge susceptibility and therefore the optical transmission in general offers new insights on the quantum conductor. Since the optical observables are not in direct correspondence with standard transport quantities, they can be used as a non-invasive probe to better characterize the quantum conductor.

5

MAJORANA FERMIONS IN TOPOLOGICAL SUPERCONDUCTORS COUPLED TO A MICROWAVE CAVITY

In this chapter, we apply the methods of cavity QED to study Majorana fermions in topological superconductors. While most of the experimental efforts are targeted at probing these quasiparticles using electronic transport measurements, we propose instead to detect the Majorana fermions by probing the light exiting from the cavity. As shown in the chapter , optical transmission coefficient that is measured in the cavity QED experiments is related to the electronic susceptibility of the topological superconductor. We analyze two superconducting systems: the prototypical Kitaev chain, and a topological semiconducting wire. For both systems, we show that the electronic susceptibility allows us to determine the topological phase transition point, the emergence of the Majorana fermions, and the parity of their ground state.

5.1 MODEL HAMILTONIAN

We study a topological superconductor capacitively coupled to a microwave cavity. The sketch of the system is presented in Fig. (7.1).

In the following, we consider various models of topological superconductors coupled to a superconducting microwave cavity, such as the Kitaev model [49], and the spin-orbit coupled nanowire subject to a magnetic field and in the proximity of an s-wave superconductor [59, 71].

The general Hamiltonian for the one-dimensional systems we consider here is of the form:

$$H_{sys} = H_{el} + H_{el-ph} + H_{ph}\,, \tag{5.1}$$

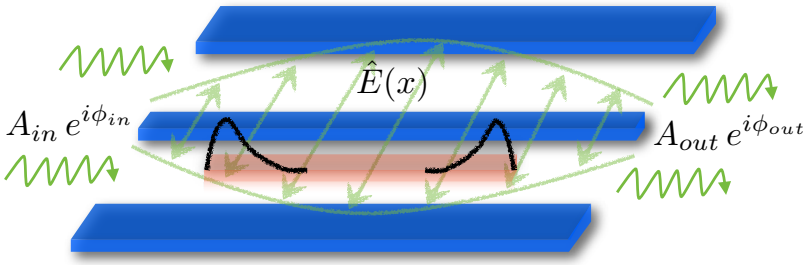

Figure 5.1: A sketch of the system: a one dimensional system (red rectangle) is placed at the maximum of the electrical field (green straight arrows) inside a superconducting microwave cavity (blue). The electromagnetic field inside the cavity is probed by sending input fields of amplitude and phase A_{in} and ϕ_{in}, respectively, and measuring the field at the end with A_{out} and ϕ_{out}. The difference between the two gives a direct access to the electronic correlation function in the wire (see text). The presence of Majorana end modes in the finite wire (black curves) is also signaled in the cavity response.

where H_{el} is the electronic Hamiltonian that describes p-wave superconductor, H_{el-ph} is electron-photon coupling Hamiltonian that describes capacitive coupling of the p-wave superconductor to the cavity, and H_{ph} is the free photon field Hamiltonian. While the electronic term is model specific, and it will be discussed below, the electron-photon coupling Hamiltonian reads:

$$H_{el-ph} = \alpha \sum_{i=1}^{N} \hat{n}_i \, (a + a^\dagger), \tag{5.2}$$

where $a^\dagger(a)$ is the photon creation (annihilation) operator, respectively. α is the electron-photon coupling constant that couples to the charge density $\hat{n}$. This merely acts as to shift the chemical potential. We have a considered a global capacitive coupling between the electronic nanosystem and the cavity electric field. Such a coupling can be justified by a full microscopic approach (see Appendix C.1 for details and also [23] that provides a microscopic description of the electric coupling between electrons in a nanocircuit and cavity photons).

The charge susceptibility of the electronic system (which can be here a 1D p−wave superconductor or a topological 1D wire) reads

$$\Pi(t-t') = -i\alpha^2\theta(t-t')\langle[\hat{n}_I(t),\hat{n}_I(t')]\rangle\,, \tag{5.3}$$

where $\hat{n}_I(t) = U^\dagger(t)\hat{n}U(t)$, with $\hat{n}$ being the total number of electrons operator and $U(t) = \exp(-iH_{el}t)$ the evolution operator for the electronic system. We assume zero temperature limit ($T = 0$) so that the average $\langle\ldots\rangle$ is taken over the superconducting ground state. Note that $\Pi(\omega) = \int_{-\infty}^{\infty} dt \exp(i\omega t)\Pi(t)$ and that $\Pi(\omega) \equiv 0$ in the absence of superconductivity ($\Delta = 0$), i.e. there are no effects from such a coupling for a wire in the normal state. We detail below the models for both topological 1D systems we consider in this chapter.

5.2 TOPOLOGICAL PHASE TRANSITION DETECTION

Next we show that the topological phase transition can be inferred from the cavity response from the transmission $\tau(\omega)$ via the susceptibility $\Pi(\omega)$. This function can be calculated straightforwardly in the case of a closed ring, i.e. for periodic boundary conditions (PBCs), so that $c_{N+1} \equiv c_1$ for the Kitaev chain ($c_{N+1\sigma} \equiv c_{1\sigma}$ for the SO nanowire).

5.2.1 *Kitaev chain model*

The simplest model of a p-wave superconductor that hosts Majorana fermions is the Kitaev chain model [49], which we have discussed in chapter 3. Therefore, we first consider for the electronic part in Eq. (5.1), the Kitaev Hamiltonian H_{el}^K. As a reminder, it is expressed as

$$H_{el}^K = -\mu\sum_{j=1}^{N} c_j^\dagger c_j - \frac{1}{2}\sum_{j=1}^{N-1}(t\,c_j^\dagger c_{j+1} + \Delta\, c_j c_{j+1} + \text{h.c.})\,, \tag{5.4}$$

where t is the hopping parameter, Δ is the p-wave superconducting pairing potential, μ is the chemical potential, and N is the total number of sites. Also, $c_j^\dagger(c_j)$ is the creation (annihilation) electronic operator at the site j. Note that the electronic operators are spinless, and the electronic density is given by $\hat{n} = \sum_{j=1}^{N} c_j^\dagger c_j$.

In the present setup, which is based on a microwave superconducting stripline cavity, the s-wave superconductor that induces superconducting correlations in the wire could be a part of the underlaying cavity. For example, the nanowire could be tunnel-coupled to the central (super-)conductor showed in Fig. 7.1. The fact that microwave photons effectively couple only to electrons of the Kitaev chain is accounted for in Appendix C.1.

For PBCs, we can utilize the Fourier description for the electronic operators: $c_j = 1/\sqrt{N}\sum_k e^{ikj} c_k$, with $k = 2\pi n/N$ (assuming the lattice spacing $d \equiv 1$ thereon), with $n = 1 \ldots N$. For more details see Appendix C.2. By doing so, we can readily write down the electronic Hamiltonian $H_{el}^K = \sum_k H_{BdG}^K(k)$, with

$$H_{BdG}^K(k) = (-t\cos k - \mu)\,\tau_z^k - \Delta \sin k\, \tau_y^k\,, \tag{5.5}$$

where $\vec{\tau}^k = (\tau_x^k, \tau_y^k, \tau_z^k)$ are Pauli matrices that act in the Nambu (particle-hole) space, i.e. on the vectors $\vec{c}_k = (c_k, c_{-k}^\dagger)$. The coupling to the cavity, on the other hand, simply reads

$$H_{el-c} = \alpha \sum_k \tau_z^k (a^\dagger + a)\,, \tag{5.6}$$

so that the susceptibility in the time domain can be written as:

$$\Pi(t) = -i\alpha^2 \sum_k \langle 0|[\tau_z^k(t), \tau_z^k(0)]|0\rangle\,, \tag{5.7}$$

with $\tau_z^k(t) = e^{iH_{BdG}^K(k)t}\tau_z^k e^{-iH_{BdG}^K(k)t}$. Utilizing this description, after some lengthy but straightforward calculations, we obtain for the susceptibility (in the ω space):

$$\Pi(\omega) = -\alpha^2 \sum_{k>0;p=\pm} \frac{(\Delta \sin k)^2}{E_k^2} \frac{p}{\omega + 2pE_k + i\eta}\,, \tag{5.8}$$

where $E_k = \sqrt{(-t\cos k - \mu)^2 + (\Delta \sin k)^2}$ is the Bogoliubov spectrum of the 1D p-wave superconductor [from diagonalizing the BdG Hamiltonian in Eq. (5.5)] [49] and η is a small positive number that accounts for causality. For $t = \Delta$, the imaginary part $\Pi''(\omega)$ acquires a simple analytical form, and it is given by

$$\Pi''(\omega) = \frac{\alpha^2 t N}{2\mu\omega}\sqrt{1 - \frac{\left[(\omega/2)^2 - t^2 - \mu^2\right]^2}{4t^2\mu^2}}, \tag{5.9}$$

for $|t+\mu| < \omega/2 < |t-\mu|$ and is zero otherwise. The topological phase transition takes place at $|\mu| = t$, with the system being in the topological (trivial) phase for $|\mu| < t$ ($|\mu| > t$). In Fig. 5.2, we plot $\Pi''(\omega)$ (main plot) and $\Pi'(\omega)$ (inset) as a function of the chemical potential μ for various values of the cavity frequency ω. We see that this function shows a large peak at the transition point ($|\mu| = t$), which becomes narrower and more pronounced for smaller ω (compared to the gap Δ). Physically, this is due to the fact that the electronic levels close to the zero energy have larger curvatures, i.e. they are more susceptible close to the phase transition point. The real part also serves for detecting the phase transition, although not as directly as the imaginary part, as shown in Fig. 5.2, where the phase transitions are inferred from the kinks in this function. We have checked that the same peak structure holds for the cases when $\Delta \neq t$, too, the only modification being a shift in the scale for ω, which should be of the order of $\omega \sim \Delta$.

5.2.2 *Spin-orbit coupled nanowire model*

A realistic system that can emulate, in some limits, the Kitaev chain consists of a nanowire with a spin-orbit interaction, subjected to an external magnetic field, and coupled by proximity effect to an s-wave superconductor [59, 71]. The entire system is then assumed to be capacitively coupled to the microwave cavity. The tight-binding Hamiltonian H_{el}^{W}

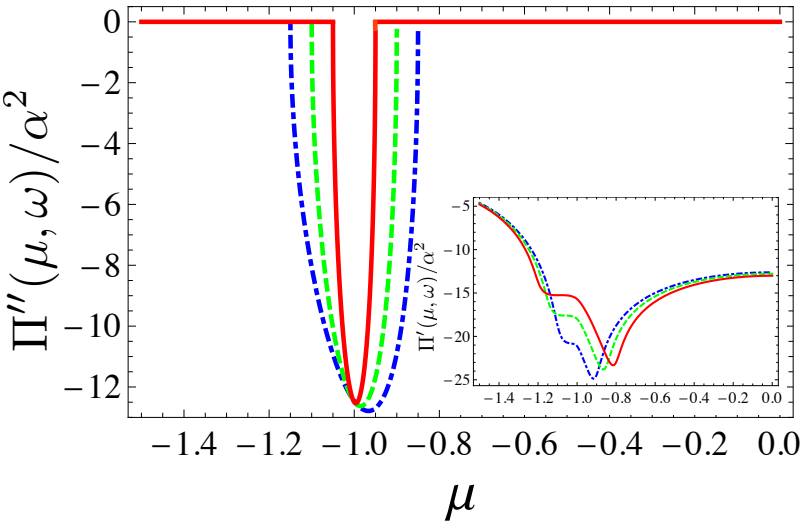

Figure 5.2: The imaginary part of the electronic susceptibility $[\Pi''(\omega)]$ as a function of μ for the Kitaev model. The topological phase transition takes place at $\mu = -1$, where this function reaches its maximum, indicating the transition point. Inset: The real part of the electronic susceptibility $[\Pi'(\omega)]$, which also shows features (kinks) around the topological phase transition point. The full, dashed, dot-dashed curves correspond to the $\omega = 0.2$, 0.3, and 0.4, respectively. We assumed $t = \Delta = 1$, $N = 50$ and all energies are expressed in terms of t.

for the nanowire with spin-orbit (SO) interaction in the presence of the magnetic field reads [79, 94]

$$\begin{aligned} H_{el}^{W} = &-t\sum_{j=1}^{N-1} c_{j+1\alpha}^{\dagger}\delta_{\alpha\beta}c_{j\beta} - \mu\sum_{j=1}^{N} c_{j\alpha}^{\dagger}\delta_{\alpha\beta}c_{j\beta} \\ &+ \Delta\sum_{j=1}^{N} c_{j\uparrow}^{\dagger}c_{j\downarrow}^{\dagger} - i\gamma\sum_{j=1}^{N-1} c_{j+1\alpha}^{\dagger}\sigma_{\alpha\beta}^{y}c_{j\beta} \\ &- V_Z\sum_{j=1}^{N} c_{j\alpha}^{\dagger}\sigma_{\alpha\beta}^{x}c_{j\beta} + \text{h.c.}\,, \end{aligned} \tag{5.10}$$

where t and μ are the hopping amplitude and the chemical potential, respectively, γ is the spin-flip hopping amplitude (or the spin-orbit coupling), Δ is the *s*-wave pairing potential induced by proximity, V_Z is the Zeeman splitting energy ($V_Z = -g\mu_B B/2$, with g and

B being the g-factor and external magnetic fields, respectively). Also, $c_{j\sigma}$ ($c^\dagger_{j\sigma}$) are the annihilation (creation) operators for electrons at site j and spin $\sigma = \uparrow, \downarrow$, and σ_i, with $i = x, y, z$ are the Pauli matrices that act in the spin space. This model accounts thus for spinful electrons. Note that we assumed the spin-orbit field and the magnetic field to be orthogonal. The coupling to the cavity is again capacitive, and the density reads in this case $\hat{n}_i = \sum_\sigma c^\dagger_{i\sigma} c_{i\sigma}$.

The case of a realistic SO coupled nanowire is more complicated that the Kitaev model showed above, and so is the evaluation of susceptibility. This is so because the SO coupled wire has four bands (because of the spin), instead of two, and a more complicated spectrum. Nevertheless, writing the electronic operators in the Fourier space as $c_{j\sigma} = 1/\sqrt{N}\sum_k e^{ikj} c_{k\sigma}$, we can write again the electronic Hamiltonian as $H^W_{el} = \sum_k H^W_{BdG}(k)$, with

$$H^W_{BdG} = [(-t\cos k - \mu) + \gamma \sin k\, \sigma_z]\tau^k_z + V_Z \sigma_x + \Delta \tau^k_x \,, \tag{5.11}$$

and the coupling to the cavity the same as in Eq. (5.6). However, the expression for $\Pi(t)$ becomes rather cumbersome for the general case and to get some analytical insights we need to resort to approximations. For that, the Hamiltonian can be put in a different form by the use of a unitary transformation (see Appendix C.3):

$$\begin{aligned} H^W_{BdG}(k) = &\left[-t\cos k - \mu + \sqrt{(\gamma \sin k)^2 + V_Z^2}\,\sigma_z\right]\tau^k_z \\ &+ \frac{\Delta\gamma \sin k}{\sqrt{(\gamma \sin k)^2 + V_Z^2}}\tau^k_x - \frac{\Delta V_Z}{\sqrt{(\gamma \sin k)^2 + V_Z^2}}\sigma_y \tau^k_y \,, \end{aligned} \tag{5.12}$$

while the H_{el-ph} stays unchanged. Progress can be made if we assume the limit of large magnetic field, $V_Z \gg \Delta, \mu$, in which case we can neglect the last term in the above Hamiltonian. By doing so, we recover two copies of the Kitaev chain, for $\sigma_z = \uparrow, \downarrow$. The susceptibility becomes:

$$\Pi(\omega) = -\alpha^2 \sum_{k>0;p,\sigma=\pm} \frac{(\Delta_{eff} \sin k)^2}{E^2_{k\sigma}} \frac{p}{\omega + 2pE_{k\sigma} + i\eta} \,, \tag{5.13}$$

where $E_{k\sigma}$ are given by the Kitaev spectrum with:

$$\mu_{k\sigma}^{\text{eff}} = \mu - \sqrt{(\gamma \sin k)^2 + V_Z^2}\,\sigma_z\,, \tag{5.14}$$

$$\Delta_{\text{eff}} = \frac{\Delta\gamma}{\sqrt{(\gamma \sin k)^2 + V_Z^2}}\,. \tag{5.15}$$

All the results from the previous section apply to this case but with the k-dependent parameters showed above. The system is in the topological nontrivial (trivial) regime for $V_Z > \sqrt{\mu^2 + \Delta^2}$ ($V_Z < \sqrt{\mu^2 + \Delta^2}$). In Fig. 5.3 we plot the imaginary part of the susceptibility as a function of the Zeeman splitting V_Z for two different values of the cavity frequency ω_c. We see a similar behavior as in the case of the Kitaev chain: a peak emerges in $\Pi''(\omega)$ at the topological phase transition point, which becomes narrower as $omega$ becomes smaller. However, an extra peak emerges at a larger V_Z, and it is due to the resonance condition with the gaps around the $k \sim k_F$ (external gaps in the SO coupled nanowire spectrum).

5.3 MAJORANA FERMIONS DETECTION

In this section, we consider a finite 1D topological system coupled to the cavity (therefore with open boundary conditions, or OBCs), so that there are two Majorana fermions emerging in the topological region, each localized at one of the two ends of the chain. Taken together, they give rise to a zero-energy fermionic state in the infinite wire limit, which can be either empty or occupied, thus labeling the *parity* of a 1D p-wave superconductor [4]. The Majorana wavefunctions decay exponentially in the wire on the scale of the superconducting correlation length ξ, and for a finite wire it can lead to a finite energy splitting $\epsilon_M \propto \exp(-L/\xi)$ of the initially zero energy fermionic state [49]. In the following, we show that both the presence of the Majorana fermions and the parity of the Majorana fermionic state can be inferred from the susceptibility $\Pi(\omega)$.

In the finite chain case, we can no longer obtain exact results for the electronic susceptibility $\Pi(\omega)$, and therefore we proceed to calculate this quantity numerically (see

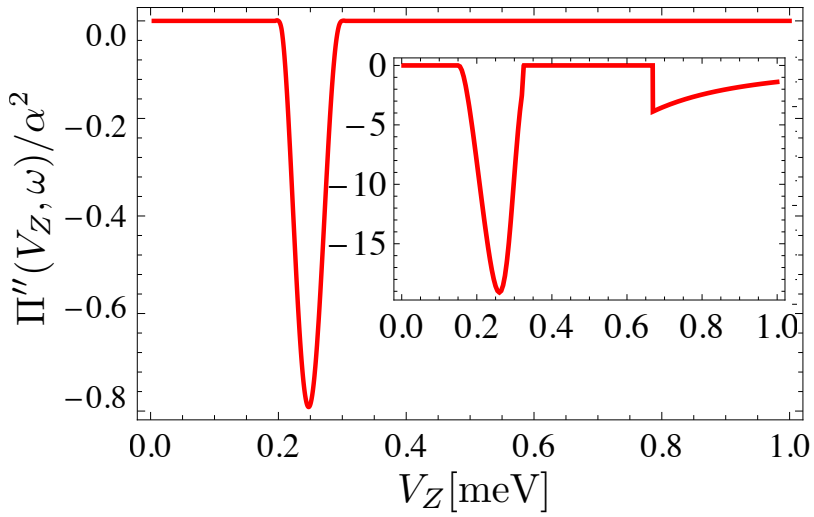

Figure 5.3: The imaginary part of the electronic susceptibility $[\Pi''(\omega)]$ as a function of the Zeeman splitting V_Z for a SO coupled nanowire in case of PBCs for parameters $L = 2\,\mu m$, $t = 0.5 \cdot 10^{-2}$ eV, $\alpha = 0.4$ meV, $\mu = -10^{-2}$ eV, $\Delta = 0.25$ meV, $N = 80$, and $\omega = 0.1$ meV ($\omega = 0.2$ meV in the Inset). The topological transition takes place for $V_Z \approx 0.25$ meV, for which the susceptibility reaches its maximum. The emergence of a second peak is due to the resonance condition around the external gaps ($k \sim k_F$).

Appendix C.4). We treat the two models, the Kitaev chain and the SO coupled wire, on equal footing, showing that they give similar results.

For starters, the electronic Hamiltonian can be cast in the following form:

$$H_{el} = \frac{1}{2}\vec{c}^{\dagger} M \vec{c}, \tag{5.16}$$

with

$$\vec{c} = (\{c_{1s}\} \ldots \{c_{Ns}\}\{c_{1s}^{\dagger}\} \ldots \{c_{Ns}^{\dagger}\}), \tag{5.17}$$

where s counts internal degrees of freedom, such as spin, band index, etc. For the Kitaev chain $s = 1$ (and thus we can disregard it), while for the SO coupled nanowire $s = \uparrow, \downarrow$. Here, M is a $2Ns \times 2Ns$ matrix [49], and we can write $M = PWP^T$, with

$$W_{2p-s,2k-s} = (-1)^{s+1}\delta_{p,k}\epsilon_k; \quad s = 0, 1. \tag{5.18}$$

P is a unitary matrix ($PP^T = P^TP = 1$) whose columns are the eigenvectors of M [49]. Also, ϵ_p, with $p = 1, \ldots, sN$ are the eigenenergies of the electronic Hamiltonian, including the Majoranas (if present). Thus, the electronic Hamiltonian can be rewritten as

$$H_{el} = (1/2)\vec{\tilde{C}}^{\dagger} W \vec{\tilde{C}},$$

and $\vec{\tilde{C}} = P^{\dagger}\vec{C}$, where

$$\vec{\tilde{C}} = (\{\tilde{c}_{1s}\}\ldots\{\tilde{c}_{Ns}\}\{\tilde{c}^{\dagger}_{1s}\}\ldots\{\tilde{c}^{\dagger}_{Ns}\}), \tag{5.19}$$

with $\tilde{c}^{\dagger}_p$ ($\tilde{c}_p$) are the creation (annihilation) operators for the Bogoliubov quasiparticles in the finite wire, with $p = 1 \ldots N$ labeling the energy levels. Finally, we can write

$$H_{el} = \sum_{p,s} \epsilon_{ps}\left(\tilde{c}^{\dagger}_{ps}\tilde{c}_{ps} - \frac{1}{2}\right), \tag{5.20}$$

and also define the spinorial wavefunction for the state of energy $\pm\epsilon_{ps}$ at position j as $\vec{\psi}_{ps}(j) = (u^j_{ps}, v^j_{ps})^T$, where $u^j_{ps}(v^j_{ps}) = P_{2j-1,p}(P_{2j,p})$ are the electron (hole) components of the wavefunction at position j in the wire.

The electron-cavity coupling Hamiltonian can then be written in the new basis as follows:

$$\begin{aligned} H_{el-ph} = \sum_{p,p'} &\left[C^{(1)}_{ps,p's'}\tilde{c}^{\dagger}_{ps}\tilde{c}_{p's'} - iC^{(2)}_{ps,p's'}\tilde{c}^{\dagger}_{ps}\tilde{c}^{\dagger}_{p's'} + \text{h.c.}\right] \\ &\times (a^{\dagger} + a), \end{aligned} \tag{5.21}$$

where $C^{(1,2)}_{ps,p's'}$ are coefficients that depend on the transformation from the electronic basis $\vec{C}$ to the Bogoliubov basis $\vec{\tilde{C}}$ and read [23, 96]:

$$C^{(1,2)}_{ps,p's'} = \alpha \sum_{j=1}^{N} \vec{\psi}^{\dagger}_{ps}(j)\tau_{z,y}\vec{\psi}_{p's'}(j)\,. \tag{5.22}$$

Here the pseudo-spin $\vec{\tau} = (\tau_x, \tau_y, \tau_z)$ acts in the Nambu (or particle-hole) subspace. In general, all $C^{(1,2)}_{ps,p's'} \neq 0$ for $p \neq p'$ and $s \neq s'$, thus there are couplings between all the levels (and bands) via the cavity field, and that includes transitions between the Majorana and the bulk (or gapped) modes. This in turn affects the correlation function in Eq. (5.3), which can be written as $\Pi(\omega) = \Pi_{BB}(\omega) + \Pi_{BM}(\omega) + \Pi_{MM}(\omega)$, being the sum of the terms that contain only bulk states (bulk-bulk, or BB), cross terms between Majorana and the bulk (bulk-Majorana or BM), and Majorana contributions only (Majorana-Majorana or MM), respectively. However, $\Pi_{MM}(\omega) \equiv 0$ [22] due to the fact that the cavity cannot mix different parities, and consequently the only contribution from the Majorana modes comes through the cross terms $\Pi_{BM}(\omega)$. We have found that for $N \gg 1$, the $\Pi_{BB}(\omega)$ contribution is given by the one obtained from the PBCs, i.e., $\Pi_{BB} \propto N$, while $\Pi_{BM} \propto \text{const}$, up to exponentially small terms in L/ξ.

In the following, we analyze the cross-terms contribution $\Pi_{BM}(\omega)$. For $\epsilon_M \ll \epsilon_p \pm \omega$, with $p \neq M$, we obtain:

$$\begin{aligned}\Pi_{BM}(\omega) = &\sum_{p,s\neq M} \left(\frac{1}{\epsilon_{ps} + \omega + i\eta} + \frac{1}{\epsilon_{ps} - \omega - i\eta} \right) \\ &\times \left[|C^{(1)}_{M,ps}|^2 (n_M - n_{ps}) - |C^{(2)}_{M,ps}|^2 (n_M - 1 + n_{ps}) \right] ,\end{aligned} \tag{5.23}$$

where n_{ps} and n_M are the occupations of the bulk and Majorana states, respectively. Inspecting the above expression, we see that it is strongly dependent on the Majorana state parity n_M. Assuming that $\epsilon_{ps} > 0$ for $p, s \neq M$ and $n_{ps} = 0$ for $n \neq M$ in the ground state, we obtain that $\Pi^{+}_{BM} \propto |C^{(1)}_{M,ps}|^2$ ($\Pi^{-}_{BM} \propto |C^{(2)}_{M,ps}|^2$) for $n_M = 1$ ($n_M = 0$). To

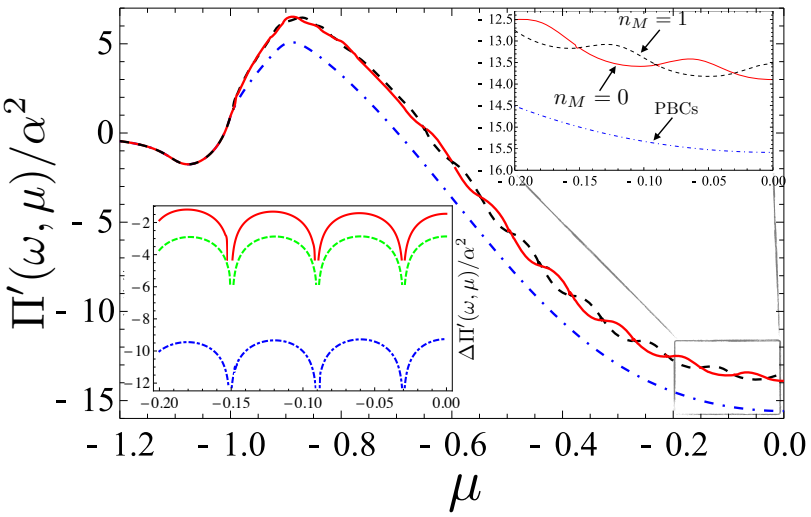

Figure 5.4: Dependence of $\Pi'(\omega,\mu)$ on the chemical potential μ. The blue (dot-dashed), red (full), and the black (dashed) lines correspond to the susceptibility for PBCs, OBCs for parity $n_M = 0$, and OBCs for parity $n_M = 1$, respectively. Lower Inset: the relative strength of the susceptibility $\Delta\Pi' = 2\left|(\Pi^+_{BM} - \Pi^-_{BM})/(\Pi^+_{BM} + \Pi^-_{BM})\right|$ as a function of μ in logarithmic scale, for $\Delta = 0.1$ (red-full), $\Delta = 0.2$ (green-dashed), and $\Delta = 0.3$ (blue-dot-dashed). The size of $\Delta\Pi'$ is exponentially reduced as a function of Δ. We used $N = 50$, $\omega = 0.2$, $\Delta = 0.1$, $t = 1$, and all energies are expressed in terms of t.

get more physical insight into the resulting susceptibility, we write the coefficients $C^{(1,2)}_{M,ps}$ in the following way:

$$C^{(r)}_{M,ps} = \sum_j [(u^j_M \delta_{r,1} + v^j_M \delta_{r,2}) u^j_{ps} - (u^j_M \delta_{r,2} + v^j_M \delta_{r,1}) v^j_{ps}] \,. \tag{5.24}$$

Let us analyze the implication of the above result. When $\epsilon_M = 0$, we also have $u^j_M = v^j_M$, and thus $C^{(1)}_{Mp} = C^{(2)}_{Mp}$, since electron and hole contributions are the same in the Majorana state. However, for a finite energy splitting $\epsilon_M \neq 0$, and thus we have that $u^j_M \neq v^j_M$, which in turn results in $C^{(1)}_{Mp} \neq C^{(2)}_{Mp}$. All these suggest that the susceptibility $\Pi(\omega)$, via $\Pi_{BM}(\omega)$ should allow us to infer both the parity of the ground state and the zeros in the Majorana energy ϵ_M, assuming their spatial overlap is large enough.

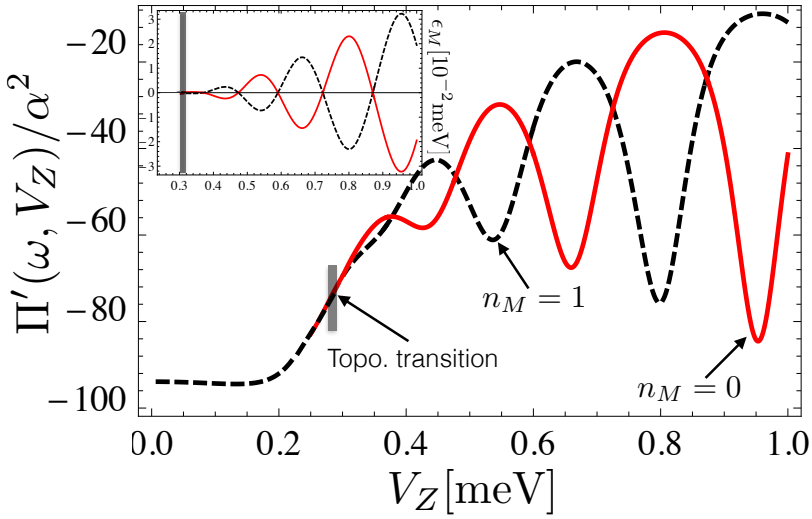

Figure 5.5: Dependence of $\Pi'(\omega, V_Z)$ on the Zeeman splitting V_Z. Above the topological transition (indicated in the figure), the red (full) and black (dashed) curves correspond to $\Pi'(\omega, V_Z)$ for parity $n_M = 0$ and $n_M = 1$, respectively. $\Pi'(\omega, V_Z)$ shows oscillations as a function of V_Z, that are different in amplitude for the two parities $n_M = 0, 1$ (but having the same period), crossing at points where $\epsilon_M = 0$ (see Inset). Below the topological transition the susceptibility reproduces well the one for PBCs. The parameters we took are [8]: $L = 2\mu m$, $t = 0.5 \cdot 10^{-2} eV$, $\alpha = 0.4 meV$, $\mu = -10^{-2} eV$, $\Delta = 0.25 meV$, $\omega = 0.02 meV$, and $N = 80$.

In the main plot in Fig. 5.4, we show the real part $\Pi'(\omega)$ for the Kitaev chain as a function of the chemical potential μ for the two parities $n_M = 0, 1$ as well as the bulk value for PBCs. First of all, the values for $\Pi(\omega)$ in case of periodic and open BCs are different because of $\Pi_{BM}(\omega)$, as this contribution has a different dependence on μ and Δ from the bulk states. Second of all, the open BCs wire susceptibility shows oscillations as a function of μ on top of the average value, of the form $\pm \cos(k_F L)$, with $+(-)$ corresponding to $n_M = 1$ ($n_M = 0$), i.e. they are opposite in sign for the two parities. Here k_F is the Fermi wavevector of the electronic system, and for the range of parameters considered is $k_F \approx 2\mu$ [49]. This means that the cavity field can access the parity of the Majorana fermions non-invasively and without locally accessing the wire. Moreover, the oscillations disappear below the phase transition point $|\mu| = 1$, the susceptibility $\Pi'(\omega)$ acquires the same value as for the PBCs wire which signals that the Majorana fermions exist only above

the topological phase transition. In order to get a closer look at the oscillations of $\Pi(\omega,\mu)$, in the lower inset in Fig. 5.4 we show the real part of the relative difference between the two parities, $\Delta\Pi(\omega,\mu) = 2\left|(\Pi^{+}_{BM} - \Pi^{-}_{BM})/(\Pi^{+}_{BM} + \Pi^{-}_{BM})\right|$, for different values of Δ. We see that the oscillations have the same periodicity as the Majorana energy splitting $\epsilon_M \sim \exp(-L/\xi)\cos(k_F L)$. Notice that the oscillations of the Majorana splitting with the magnetic field (chemical potential) has been studied in detail [77, 85] together with the fact that the magnitude of the oscillations becomes exponentially suppressed in L/ξ [74, 106].

In the main figure in Fig. 5.5, we plot the real part of the susceptibility for a 1D topological wire as a function of the Zeeman splitting V_Z for the two parities $n_M = 0, 1$. The susceptibility Π for that figure was computed using realistic parameters that might be appropriate for an InSb wire such as in the experiments in Ref. [64]. We find similar features as for the Kitaev toy model, namely oscillations as a function of the Zeeman splitting above the topological transition. These oscillations around the ground state have opposite sign and different amplitudes for each parity. Like for the Kitaev model, they have the same periodicity as the Majorana energy ϵ_M (see the inset of Fig. 5.5) and cross at points where $\epsilon_M = 0$. Notice that if the parity is not conserved in the system (for example, due to the quasi-particle poisoning), Π' will follow the ground state and exhibit therefore sharp cusps as a function Δ_Z at the crossing points where $\epsilon_M = 0$ (see also Ref. [98] for similar features in a topological Josephson junction). As for the Kitaev chain, we thus find that the cavity phase shift is thus able to detect the Majorana fermions and the parity of the ground state of a realistic topological wire.

The imaginary part of $\Pi(\omega)$ gives us also information on the presence of Majorana fermions. In Fig. 5.6, we show the dependence of $\Pi''(\omega)$ on ω for the Kitaev chain, both in the topological and non-topological regimes, for $t = \Delta$. We see that the Majorana fermions, through $\Pi_{BM}(\omega)$, give rise to an extra peak in the susceptibility at half the effective superconducting gap $\Delta_{\text{eff}} = ||\mu| - t|$ in the topological regime, while such a peak is absent for the same effective gap Δ_{eff}, but in the non-topological case. For completeness, we also show the result for PBCs, in which case there are no Majorana fermions.

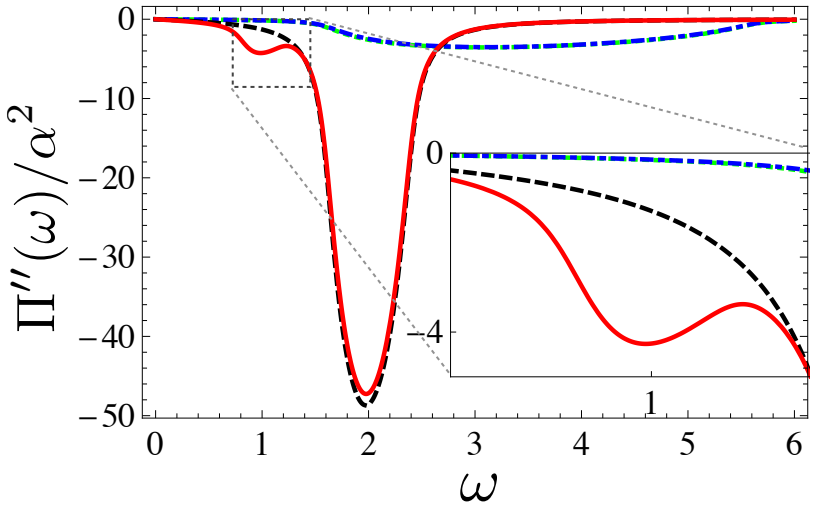

Figure 5.6: Dependence of $\Pi''(\omega)$ on the cavity frequency ω for $N = 50$. The full-red (dashed-black) line corresponds to the susceptibility in the topological regime for $\mu = -0.2$, while the dot-dashed-blue (dotted-green) corresponds to the non-topological regime with open (periodic) BCs with $\mu = -1.8$, so that the effective gap is the same $\Delta_{\text{eff}} = ||\mu| - t| = 0.8$ in both regions. Inset: a zoom in the region where the Majorana peak emerges. For all the plots we used $t = \Delta = 1$, and all energies are expressed in terms of t.

Finally, let us give some estimates for $\Pi(\omega)$, and in particular for $\Pi_{BM}(\omega)$ and the resulting phase shift in the exiting photonic signal. We assume typical experimental values for the cavity frequency, $\omega_c \approx 2 \times 10^{-5}$ eV, and with a quality factor $Q \approx 10^5$, which results in photon escape rate $\kappa = 2 \times 10^{-10}$ eV. For an estimate of the capacitive coupling α we refer, for example, to the case of carbon nanotubes, which have been under experimental scrutiny in the context of cavity QED [23, 29]. There, it was found that $\alpha \approx 5.6 \times 10^{-7}$ eV, and we believe similar values should be relevant for semiconductor nanowires too. The phase shift of the radiation exiting the cavity satisfies $\delta\phi \propto (\alpha^2/t\,\kappa)$ so that we obtain $\delta\phi \approx 0.3$ which is a sizeable value.

5.4 CONCLUSIONS

In this chapter, we studied two paradigmatic examples of 1D topological superconducting systems capacitively coupled to a microwave superconducting stripline cavity: the Kitaev chain and a 1D nanowire with strong SO interaction in the presence of a magnetic field and in proximity of a superconductor. We analyzed the electronic charge susceptibility of these systems that is revealed in the photonic transport through the microwave cavity via its transmission $\tau(\omega)$. We demonstrated that this electronic susceptibility can actually be used to detect the topological phase transition, the occurrence of Majorana fermions and the parity of the Majorana fermionic state in a non-invasive fashion. Such effects are due to the interplay between the bulk and Majorana states, either via virtual or real transitions taking place between the two, and which are mediated by the photonic field.

6

DETECTION OF MULTIPLE MAJORANA FERMIONS COUPLED TO A MICROWAVE CAVITY

In this chapter, we discuss the case of multiple Majorana fermions emerging at each edge of the wire. This situation becomes possible if the system has not only the nearest-neighbor hopping, but also the next-nearest-neighbor hopping. We discuss what possible signatures of multiple Majorana fermions could be visible in cavity QED experiments. We start with establishing the phase diagram of the extended Kitaev model. We discuss for which set of parameters it is possible to obtain the oscillations of the Majorana energy splitting. Then we demonstrate that the electronic susceptibility can be used to probe the phase transitions from 0 to 1 to 2 Majorana fermions present in the system. Moreover, the frequency response of the cavity is sensitive to the transitions between two lowest-energy Majorana states. Also we show that there are oscillations of the electronic susceptibility as a function of chemical potential similar to the ones of the Majorana energy splitting. These oscillations have different periodicity depending whether there is one or two Majorana fermions at each end of the chain.

6.1 MODEL HAMILTONIAN

Let us consider a model of the topological wire that allows for multiple Majorana fermions emerging in the system. The Kitaev model with the next-nearest-neighbor hopping that can show up to two Majorana fermions emerging at each end of the chain has been introduced in [68]. Later the fractional Josephson effect with multiple Majorana fermions has been studied [91] and it was shown that the experimentally accessible quantity differential conductance dI/dV should be doubled when there are two Majorana fermions at

each end of the chain. However, the doubling of the differential conductance has not been observed experimentally.

We consider the extended Kitaev chain model that includes also the hopping and superconducting pairing between next-nearest-neighbors (see Fig.6.1).

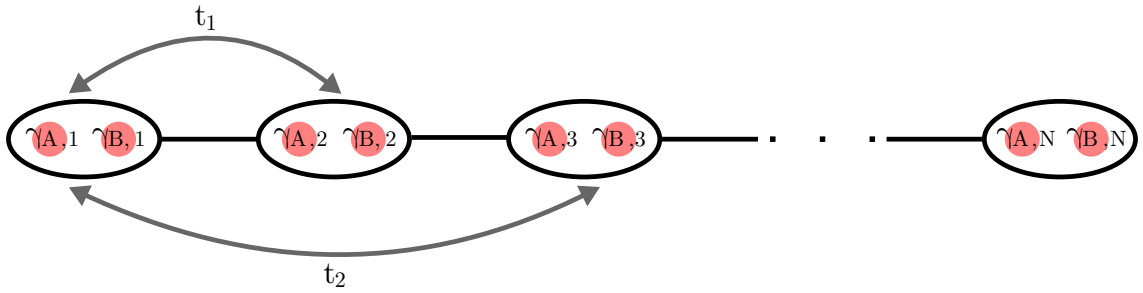

Figure 6.1: Scheme of the extended Kitaev chain. t_1 is the nearest-neighbor hopping amplitude and t_2 is the next-nearest-neighbor hopping amplitude.

The Hamiltonian of the Kitaev chain model with next-nearest-neighbor hopping and superconductivity reads [68]

$$H_{el} = -2\mu \sum_{j=1}^{N} c_j^\dagger c_j - \sum_{j=1}^{N-1} \left(t_1 c_j^\dagger c_{j+1} + \Delta_1 c_j c_{j+1} + h.c. \right) - \sum_{j=2}^{N-1} \left(t_2 c_{j-1}^\dagger c_{j+1} + \Delta_2 c_{j-1} c_{j+1} + h.c. \right), \tag{6.1}$$

where μ is the chemical potential, t_1 is the nearest-neighbor hopping amplitude, Δ_1 is the nearest-neighbor superconducting pairing potential, t_2 is the next-nearest-neighbor hopping amplitude and Δ_2 is the next-nearest-neighbor superconducting pairing potential. N is the total number of sites. $c_j^\dagger (c_j)$ are the electron at the site j creation (annihilation) operators, respectively. When $t_2 = \Delta_2 = 0$, this Hamiltonian in Eq.(6.1) corresponds to the Kitaev model.

We consider capacitive coupling between the topological wire and the cavity,

$$H_{el-ph} = \alpha \sum_{j=1}^{N} c_j^\dagger c_j (a + a^\dagger), \tag{6.2}$$

where α is the electron-photon coupling constant and a ($a^\dagger$) is the photon annihilation (creation) operator. In the previous chapter, we found the relation between the susceptibility of the Kitaev chain and the transmission coefficient of the cavity in the presence of the topological wire. As shown in [34], the susceptibility for the topological wire coupled to the cavity reads

$$\Pi(t) = -i\theta(t)\alpha^2 \langle \left[c_j^\dagger(t) c_j(t), c_j^\dagger(0) c_j(0) \right] \rangle. \tag{6.3}$$

Here we compute the electronic susceptibility of the Kitaev chain with the next-nearest-neighbor hopping.

6.2 PHASE DIAGRAM AND ENERGY SPECTRUM

Let us start our study of the extended Kitaev chain model by establishing a phase diagram of the system. To do so, we close the wire into a ring by applying periodic boundary conditions, $c_{N+1} \equiv c_1$, and perform Fourier transformation. The electronic Hamiltonian of the system in the k-space, $H = \sum_{k>0} H_k(k)$, reads

$$H_k(k) = [-2\mu - 2t_1 \cos(k) - 2t_2 \cos(2k)]\tau_z + [-2\Delta_1 \sin(k) - 2\Delta_2 \sin(2k)]\tau_y. \tag{6.4}$$

In order to compute the winding number of the system, let us diagonalize the Hamiltonian $H_k(k)$ by performing a unitary transformation $\tilde{H}_k(k) = U^\dagger H_k(k) U$ with $U = \exp(-i\theta_k \tau_x/2)$.

$$\tan(\theta_k) = -\frac{\Delta_1 \sin(k) + \Delta_2 \sin(2k)}{\mu + t_1 \cos(k) + t_2 \cos(2k)}. \tag{6.5}$$

The bulk energy spectrum of the extended Kitaev model reads

$$E_{k,\pm} = \pm 2\sqrt{(\mu + t_1 \cos(k) + t_2 \cos(2k))^2 + (\Delta_1 \sin(k) + \Delta_2 \sin(2k))^2}. \tag{6.6}$$

The condition for the topological phase transition is closing of the gap, $E_k = 0$. In general case, when $t_1 \neq \Delta_1$ and $t_2 \neq \Delta_2$, the gap at $k = 0$ closes when $t_2 = -\mu - t_1$ and the gap at $k = \pi$ closes when $t_2 = -\mu + t_1$, while the third condition can be found only numerically.

Now let us calculate how many Majorana zero modes are in each phase. To do so, let us compute the winding number [55, 68] $P = \int_0^{2\pi} \frac{d\theta_k}{2\pi}$.

We compute numerically the winding number and find the phase diagram of the Kitaev model with next-nearest-neighbor hopping and superconducting pairing. As can be seen from the phase diagram Fig.6.2, when changing the chemical potential μ for a fixed values of the next-nearest-neighbor hopping amplitude t_2 and superconducting pairing $\Delta_1 = \Delta_2$, the phase of the system can change from non-topological with 0 Majorana fermions at each end of the chain to topological with 1 Majorana fermion at each end of the chain, then again to topological, but with 2 Majorana fermions, and again to non-topological with 0 Majorana fermions. The winding number that corresponds to this phase transition ($0 \to 1 \to 2 \to 0$) as a function of the chemical potential is presented in Fig.6.3.

Now that we have found the phase diagram of the wire that can support multiple Majorana fermions, let us compute the energy spectrum for the chain with open boundary conditions that can host Majorana fermions at its ends. When we tune the parameters of the chain so that there is only one Majorana fermion at each end of the wire for $-1 < \mu < -0.5$ and two Majorana fermions for $-0.5 < \mu < 0$, we can see that the period of oscillations of the Majorana energy splitting changes over the phase transition (see Fig.6.4).

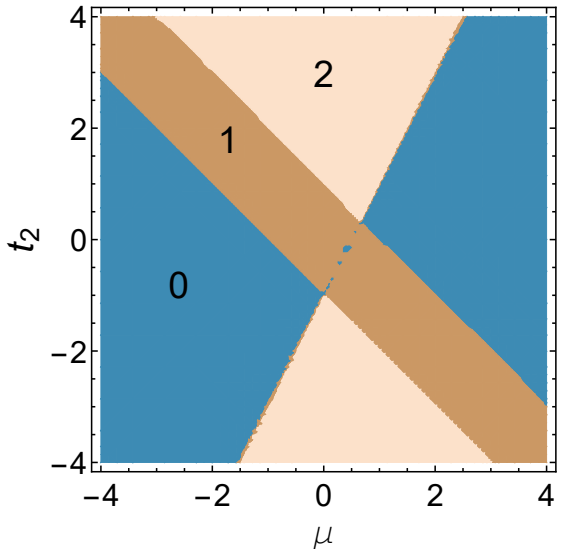

Figure 6.2: The phase diagram of the extended Kitaev model as a function of μ and t_2 for parameters: $t_1 = 1$, $\Delta_1 = \Delta_2 = 0.2$. Numbers $0, 1, 2$ in the plot indicate the number of the Majorana fermions at each end of the chain for particular values of (μ, t_2).

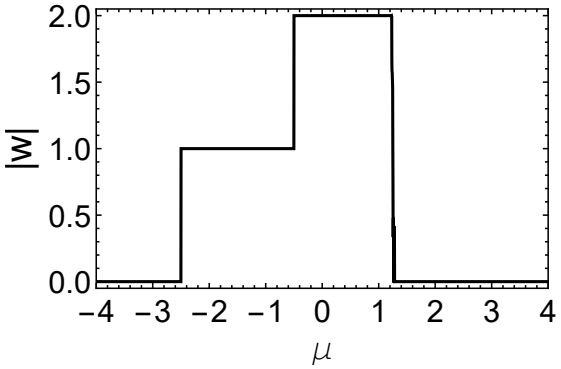

Figure 6.3: The winding number $|w|$ of the extended Kitaev model as a function of chemical potential μ for parameters: $t_1 = 1$, $\Delta_1 = \Delta_2 = 0.2$ and $t_2 = 1.5$.

6.3 ELECTRONIC SUSCEPTIBILITY

In this section, we calculate the electronic susceptibility of the extended Kitaev model for periodic and open boundary conditions for different chemical potential and frequency.

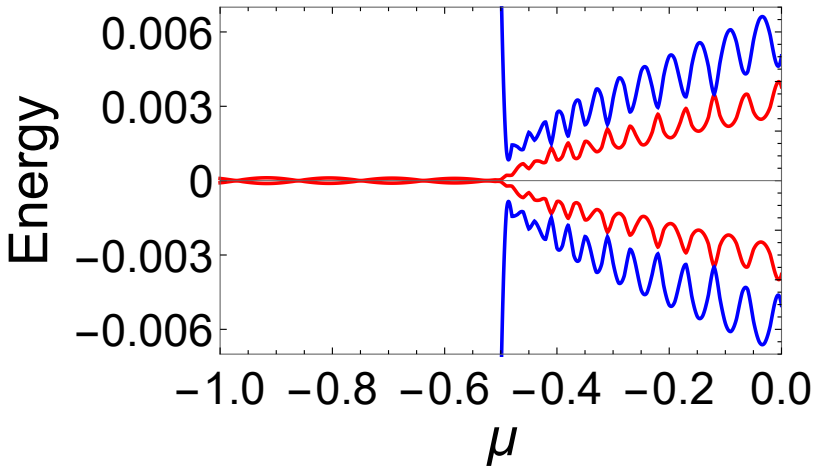

Figure 6.4: Energy spectrum as a function of chemical potential μ in case of open boundary conditions for parameters: $N = 100$, $t_1 = 1$, $t_2 = 1.5$,$\Delta_1 = \Delta_2 = 0.2$. Red line corresponds to the lowest-energy state, first Majorana fermion (M_1) and blue line corresponds to the second lowest-energy state, second Majorana fermion (M_2). Phase transition point is $\mu = -0.5$.

6.3.1 *Topological phase transition detection*

As was demonstrated in chapter 3, the topological phase transition points can be inferred from the response of the cavity when the topological wire is closed in a ring. Electronic susceptibility for the extended Kitaev chain reads

$$\Pi(t) = -i\theta(t) \sum_{k,q>0} \langle \left[\tau_z(t), \tau_z(0) \right] \rangle. \tag{6.7}$$

After performing Fourier transformation and substituting sum with the integral (see appendix D for more details on the derivation), the susceptibility of the closed chain reads

$$\Pi(\omega) = \frac{N}{2\pi} \int_0^{\pi} dk \frac{4(\Delta_1 \sin(k) + \Delta_2 \sin(2k))^2}{E_k^2} \left(\frac{1}{\omega - 2E_k + i\eta} - \frac{1}{\omega + 2E_k + i\eta} \right). \tag{6.8}$$

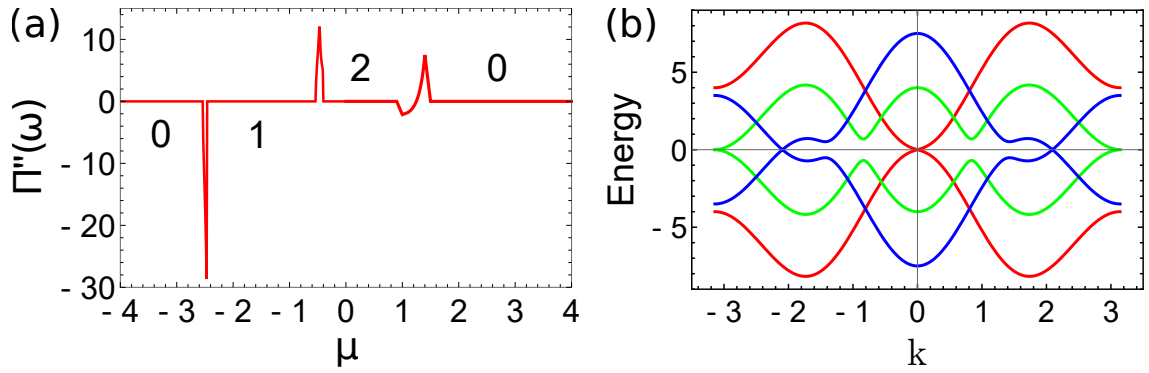

Figure 6.5: a) Imaginary part $\Pi''(\omega)$ as a function of μ in case of periodic boundary conditions for parameters: $N = 100$, $t_1 = 1$, $t_2 = 1.5$, $\Delta_1 = \Delta_2 = 0.2$, $\omega = 0.15$. Numbers in the plot indicate the number of the Majorana fermions in the region between the phase transitions obtained by computing the corresponding winding number. b) Bulk energy spectrum $E_{k,\pm}$ as a function of k in case of periodic boundary conditions for parameters: $t_1 = 1$, $t_2 = 1.5$, $\Delta_1 = \Delta_2 = 0.2$. Red line corresponds to $\mu = -2.5$ (gap closes at $k = 0$, which corresponds to the topological phase transition from 0 to 1 Majorana fermions), green line corresponds to $\mu = -0.5$ (gap closes at $k = \pi$, which corresponds to the topological phase transition from 1 to 2 Majorana fermions) and blue line corresponds to $\mu \approx 1.25$ (which corresponds to the topological phase transition from 2 to 0 Majorana fermions).

We can compute the imaginary part of the susceptibility Eq.6.8 analytically. We obtain that $\Pi''(\omega)$ as a function of the chemical potential peaks at the values of the chemical potential that correspond to the topological phase transition (see Fig.6.5, a)). Moreover, depending on how the number of the Majorana fermions changes over the phase transition the structure of the peak changes. The susceptibility has a minimum at $\mu = -2.5$ (see Fig.6.5, a)) that in the energy spectrum corresponds to the gap closing at $k = 0$ (see Fig.6.5, b)). This value of the chemical potential corresponds to the topological phase transition from 0 to 1 Majorana fermion (see Fig.6.3). Then the maximum of $\Pi''(\mu)$ at $\mu = -0.5$ corresponds to the energy gap closing at $k = \pi$. $\mu = -0.5$ corresponds to the topological phase transition from 1 to 2 Majorana fermions. And finally the double peak in the susceptibility at $\mu \approx 1.25$ corresponds to the topological phase transition from 2 to 0 Majorana fermions.

6.3.2 *Frequency dependence of the cavity response*

Now let us calculate the susceptibility of the Kitaev chain with the next-nearest-neighbors hopping in case of open boundary conditions. Since this model can show up to 2 Majorana fermions at each end of the chain, there are four different combinations of the Majorana parity:

1. $n_{M_1} = 0, n_{M_2} = 0$
2. $n_{M_1} = 1, n_{M_2} = 1$
3. $n_{M_1} = 0, n_{M_2} = 1$
4. $n_{M_1} = 1, n_{M_2} = 0,$

where M_1 corresponds to the lowest-energy state, or first Majorana fermion, and M_2 corresponds to the second-lowest-energy state, or second Majorana fermion. If there are two Majorana fermions, the susceptibility of the wire can be decomposed as:

$$\Pi(\omega) = \Pi_{BB}(\omega) + \Pi_{BM_1}(\omega) + \Pi_{BM_2}(\omega) + \Pi_{M_1M_2}(\omega) + \Pi_{M_1M_1}(\omega) + \Pi_{M_2M_2}(\omega), \tag{6.9}$$

where Π_{BB} corresponds to the transitions between different bulk levels, $\Pi_{BM_1}(\omega)$ ($\Pi_{BM_2}(\omega)$) comes from the transition between bulk and M_1 (M_2) Majorana levels while $\Pi_{M_1M_1}(\omega) = \Pi_{M_2M_2}(\omega) \equiv 0$ and corresponds to the transitions between the same Majorana levels.

Electronic susceptibility of the chain for $n_{M_1} = n_{M_2} = 0$ presented in Fig.6.6 shows the non-monotonic behavior as a function of frequency ω. Real part has a kink around $\omega_p = \epsilon_{M_1} + \epsilon_{M_2}$, while imaginary part has a peak around the same value of frequency. This peak (kink) at ω_p comes from the low-energy response of the cavity, which is well separated from the higher-energy response when the frequency ω is in resonance with the effective p-wave gap. The Majorana part of the susceptibility is nonzero only when

there are two Majorana fermions at each end of the chain [34]. In spectroscopic response of the cavity there are four different peaks at $\omega = \pm\epsilon_{M_1} \pm \epsilon_{M_2}$ depending on the parity of the Majorana states.

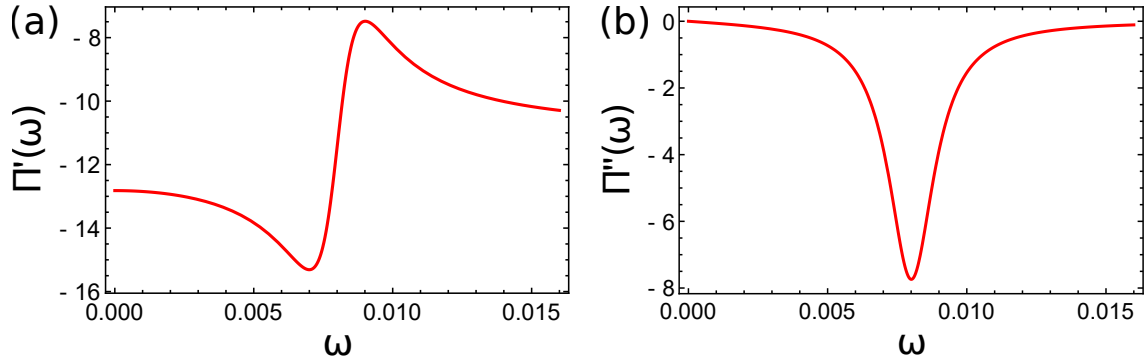

Figure 6.6: Electronic susceptibility as a function of frequency ω in case of open boundary conditions for parameters: $N = 100$, $t_1 = 1$, $t_2 = 1.5$, $\Delta_1 = \Delta_2 = 0.2$, $\eta = 0.001$ and $\mu = -0.1$. First bulk energy level is at $\epsilon_{B1} = 0.17$. a) Real part of the susceptibility $\Pi'(\omega)$ has a kink at $\omega = \epsilon_{M1} + \epsilon_{M2} = 0.008$ ($n_{M_1} = n_{M_2} = 0$). b) Imaginary part of the susceptibility $\Pi''(\omega)$ has a peak at $\omega = \epsilon_{M1} + \epsilon_{M2} = 0.008$ ($n_{M_1} = n_{M_2} = 0$).

6.3.3 *Parity dependence and oscillations of the susceptibility*

In this subsection, we discuss the dependence of the electronic susceptibility on chemical potential for different parities of the Majorana states. The real part of the susceptibility $\Pi'(\mu)$ is presented in the main plot in Fig.6.7. For $-1 < \mu < -0.5$ there is one Majorana fermion at each end of the chain and we get oscillations of $\Pi'(\mu)$ with the period equal to that for the Kitaev chain [34] (see the inset in Fig.6.7). Black and red lines correspond to different parities of the Majorana state, $n_{M_1} = 0$ and $n_{M_1} = 1$, respectively. When we cross the phase transition at $\mu = -0.5$, there are two Majorana fermions at each end of the chain and four different possibilities for the Majorana parity. Real part of the susceptibility shows oscillation as a function of chemical potential. The period of the oscillation is different compared to $-1 < \mu < -0.5$ region, but it is consistent with the Majorana energy splitting. Thus, the period of the oscillations in two different phases with one and two Majorana fermions is different and is the same as for the Majorana energy splitting.

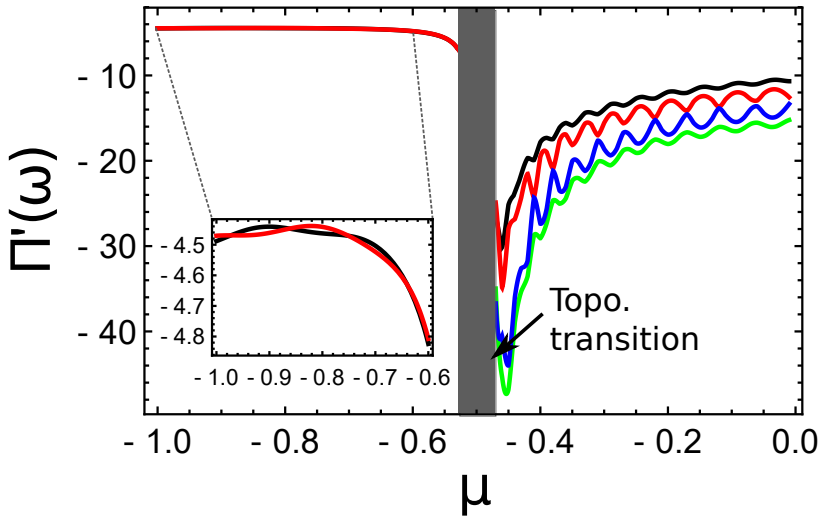

Figure 6.7: Real part of the total susceptibility $\Pi'(\omega)$ as a function of chemical potential μ in case of open boundary conditions for parameters: $N = 100$, $t_1 = 1$, $t_2 = 1.5$, $\Delta_1 = \Delta_2 = 0.2$, $\eta = 0.01$ and $\omega = 0.05$. Black line corresponds to $n_{M_1} = 0, n_{M_2} = 0$, red line corresponds to $n_{M_1} = 1, n_{M_2} = 0$, blue line corresponds to $n_{M_1} = 0, n_{M_2} = 1$ and green line corresponds to $n_{M_1} = 1, n_{M_2} = 1$. Topological phase transition point is at $\mu = -0.5$. For $\mu < -0.5$ there is one Majorana fermion at each end of the chain, while for $\mu > -0.5$ there are two Majorana fermions at each end of the chain.

The change of the oscillations period should allow to distinguish between the number of the Majorana fermions.

6.4 CONCLUSIONS

In this chapter, we studied the Kitaev model with the next-nearest-neighbor interaction that can show 0, 1 or 2 Majorana fermions emerging at each end of the finite chain. We found the phase diagram for the system for the regime when there are oscillations of the Majorana energy splitting ($t_1 \neq \Delta_1$). We demonstrated that the imaginary part of the electronic susceptibility for periodic boundary conditions is sensitive to the topological phase transitions, and the peak in $\Pi''(\mu)$ have different shape depending on the type of the phase transition ($0 \to 1$ or $0 \to 2$). We also found that the real part of the susceptibility for finite chain follows the structure of the Majorana energy splitting and shows the

change of the period of the oscillations depending weather there is one or two Majorana fermions at each end of the chain. As for the spectroscopic features, the susceptibility can show four peaks at $\omega = \pm\epsilon_{M_1} \pm \epsilon_{M_2}$ depending on the parity of the Majorana state. As an outlook, it would be interesting to apply the same approach to study the emergence of fractional fermions in the Su-Schrieffer-Heeger (SSH) model [100] and the transition from the latter to Majorana fermions.

7

JOSEPHSON EFFECT IN TOPOLOGICAL SUPERCONDUCTING RINGS COUPLED TO A MICROWAVE CAVITY

In this chapter, we study a one dimensional p-wave superconducting mesoscopic ring interrupted by a weak link and coupled inductively to a microwave cavity. We establish an input-output description for the cavity field in the presence of the ring, and identify the electronic contributions to the cavity response and their dependence on various parameters, such as the magnetic flux, chemical potential, and cavity frequency. We show that the cavity response is 4π periodic as a function of the magnetic flux in the topological region, stemming from the so called fractional Josephson current carried by the Majorana fermions, while it is 2π periodic in the non-topological phase, consistent with the normal Josephson effect. We find a strong dependence of the signal on the cavity frequency, as well as on the parity of the ground state. Our model takes into account fully the interplay between the low-energy Majorana modes and the gaped bulks states, which we show is crucial for visualizing the evolution of the Josephson effect during the transition from the topological to the trivial phase.

7.1 THE SYSTEM AND MODEL HAMILTONIAN

In Fig. 7.1, we present a sketch of the system under consideration: a topological superconducting ring which contains a weak link at some position coupled to a superconducting microwave cavity [35]. The ring is subject to both a dc magnetic flux, and an ac (quantum) flux from the cavity, which gives rise to a coupling between the two systems, the ring (electrons) and cavity (photons). We consider the Kitaev model Hamiltonian as describing the electronic p-wave superconductor. Such a model could be implemented experimentally utilizing a semiconducting nanowire with spin-orbit coupling in the proximity of s-wave

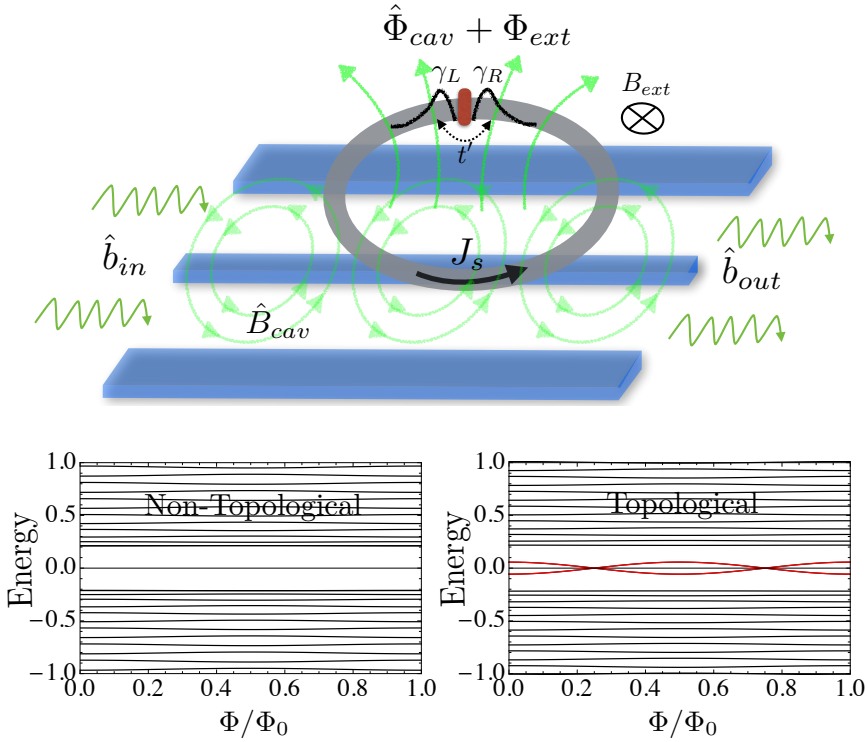

Figure 7.1: Top: A sketch of the combined topological superconducting ring inserted in a microwave cavity. The magnetic field of the cavity $\hat{B}_{cav}$ pierces the ring and gives rise to a fluctuating magnetic flux. A perpendicular, external magnetic field B_{ext} is also applied, so that the total flux felt by the electrons in the ring is $\Phi_{tot} = \Phi_{ext} + \hat{\Phi}_{cav}$. The ring is interrupted by a weak link, that pertains to the hopping strength $t' \ll t$ (t is the hopping strength within the ring, see the text). In the topological region, there are Majorana fermions on the left (γ_L) and on the right (γ_R), and Josephson current I_J is flowing within the ring. The cavity is probed in the input-output method, and the output signal $\hat{b}_{out}$ is to be compared with the input one $\hat{b}_{in}$. Bottom: Spectrum of the ring as a function of the flux Φ_{ext} in the non-topological (left) and topological (right) regions, respectively. In red are depicted the Majorana energy levels that show oscillations with a period Φ_0.

superconductor and subject to a magnetic field [59, 71]. We assume the ring is interrupted at some point by a weak link that emulates the Josephson effect in a SIS junction. The external magnetic flux allows for a continuous phase change across the weak link, which controls the Josephson current. On the other hand, the fluctuating cavity flux couples to the flux-biased system and monitors its dynamics.

The general form of the combined Hamiltonian reads:

$$H_{sys} = H_{el} + H_{ph} + H_T\,, \tag{7.1}$$

$$H_{el} = -\sum_{j=1}^{N-1}(te^{i\Phi_{jj+1}}c_j^\dagger c_{j+1} + \Delta e^{i\phi_{jj+1}}c_j c_{j+1} + \text{h.c.}) - \mu\sum_{j=1}^{N} c_j^\dagger c_j\,, \tag{7.2}$$

$$H_T = -t'e^{i\Phi_{N1}}c_N^\dagger c_1 + \text{h.c.}\,, \tag{7.3}$$

where H_{el} is the Hamiltonian of the p-wave superconductor (Kitaev model), H_T is the tunneling Hamiltonian between the ends in the presence of the magnetic flux, and $H_{ph} = \omega_c a^\dagger a$ is the Hamiltonian of a single mode cavity, where ω_c is the cavity frequency and $a^\dagger(a)$ is the photon creation (annihilation) operators, respectively. Also, t is the hopping parameter, Δ is the p-wave superconducting pairing potential, μ is the chemical potential, and N is the total number of sites. $c_j^\dagger(c_j)$ is the electron creation (annihilation) operators, respectively, at the site j. Moreover, Φ_{jj+1} and ϕ_{jj+1} are the phases on the tunneling matrix elements t and the superconducting pairing Δ at positions j caused by the external fluxes. They read:

$$\Phi_{jj+1} = \frac{e}{\hbar}\int_j^{j+1} dx A(x) \equiv \frac{2\pi\Phi_{tot}}{N\Phi_0}\,, \tag{7.4}$$

$$\phi_{jj+1} = \frac{4\pi\Phi_{tot}j}{N\Phi_0}\,. \tag{7.5}$$

The form of the second term (the phase on the pairing Δ) can be found from utilizing the following assumption: the p-wave pairing in the Kitaev chain is assumed to be induced by an s-wave superconductor underneath the wire that is interrupted at the link. In such a case, we can consider that the instantaneous supercurrent flowing through the superconductor vanishes, namely:

$$J_s = \frac{2e}{m}|\psi|^2(\hbar\nabla\phi - 2eA) \equiv 0\,, \tag{7.6}$$

where m, $|\psi|^2$, and ϕ are the electronic mass, the density of superconducting electrons in the s-wave superconductor, and its phase, respectively. The latter is directly imprinted into

the wire by means of proximity effect. We can easily solve this differential equation, which then gives the phase on the p-wave superconductor [74] $\phi(j) \equiv \phi_{jj+1} = 4\pi\Phi_{tot}j/N\Phi_0$.

We note that the system is in topological (non-topological) phase when $|\mu| < 2t$ ($|\mu| > 2t$), and it supports Majorana zero energy end modes (no Majorana end modes).

The magnetic flux contains both the dc flux Φ_{dc}, as well as a time-dependent component $\hat{\Phi}_{ac}(t)$, or $\Phi = \Phi_{dc} + \hat{\Phi}_{ac}(t)$. We assume that the ac flux is due to the cavity photons, and it is given by $\hat{\Phi}_{ac} = i\lambda(a - a^\dagger)$, with λ being the coupling constant between the ring and the cavity. Following Ref. [26], we could find that $\lambda^2 = M^2/L$, where M is the coupling inductance between the ring and the resonator and L is the geometrical inductance of the resonator.

We can rewrite the full Hamiltonian in a simpler form by performing a unitary transformation $U = \exp\left[-2\pi i \sum_{j=1}^{N}(j - 1/2)n_j\Phi_{dc}/N\Phi_0\right]$ so that the entire dependence on the dc flux Φ_{dc} is transferred to the weak link tunneling Hamiltonian H_T, or:

$$H_T \to U^\dagger H_T U = -t' e^{i2\pi\Phi_{dc}/\Phi_0} e^{i2\pi\hat{\Phi}_{cav}/N\Phi_0} c_N^\dagger c_1 + \text{h.c.} \tag{7.7}$$

We mention that such a transformation can only gauge away the dc flux (i.e. transfer it entirely to t'), while the ac (or cavity component) cannot be gauged away in a simple way because such a transformation would not commute with the photonic Hamiltonian H_{ph}. However, we assume that $\hat{\Phi}_{ac} \ll \Phi_0$, so that we can expand the exponentials in $\hat{\Phi}_{ac}$ up to second order in this quantity. With these approximations, the final Hamiltonian can be

written as the sum of the electrons (in the presence of the dc flux), the photons, and their mutual interaction:

$$H_{sys} \approx H_{el} + H_T + H_{ph} - \hat{\Phi}_{ac} I + \frac{1}{2}(\hat{\Phi}_{ac})^2 D\,, \tag{7.8}$$

$$I = \frac{2\pi i}{N\Phi_0} \sum_{j=1}^{N-1} \Big[t c_j^\dagger c_{j+1} + 2j\Delta c_j c_{j+1} + t' e^{i2\pi\Phi_{dc}/\Phi_0} c_N^\dagger c_1 - h.c. \Big]\,, \tag{7.9}$$

$$D = -\left(\frac{2\pi i}{N\Phi_0}\right)^2 \sum_{j=1}^{N-1} \Big[t c_j^\dagger c_{j+1} + (2j)^2 \Delta c_j c_{j+1} + t' e^{i2\pi\Phi_{dc}/\Phi_0} c_N^\dagger c_1 + h.c. \Big]\,. \tag{7.10}$$

This is the Hamiltonian that we will be utilizing in the following to describe the response of the cavity, up to second order in the electron-cavity coupling.

Such configuration (ring geometry) have been studied in the past in the context of persistent currents in *normal* rings, and it was shown to be physically equivalent to a SNS junction, where the low-energy system is described by the so called Andreev levels [17]. In both cases, the spectrum is quantized due to the finite size of the ring (N system), or the finite size of the N part (SNS junction). We mention that for the SNS junction, if the length of the normal part $L \ll \xi$ (ξ is the coherence length), the spectrum shows a gap that is modulated by the external flux, and can even vanish. This gap, or mini gap, is usually much smaller than the bulk superconducting gap, and these levels are responsible for all the low-energy transport properties of the junction. The Andreev levels in the presence of the flux give rise to Josephson current which, for the state n with energy ϵ_n reads:

$$i_n = -\frac{\partial \epsilon_n}{\partial \Phi_{dc}}\,. \tag{7.11}$$

The Josephson current carried by these states is then given by $I_J = \sum_n f_n i_n$, where f_n are the occupations (Fermi-Dirac) of the level n.

7.2 ELECTRONIC SUSCEPTIBILITY AND CAVITY RESPONSE

7.2.1 *Theoretical approach to susceptibility*

In this section, we discuss the cavity response in the presence of the p-wave superconductor, and the dependence on various electronic parameters, such as the chemical potential and the applied magnetic flux Φ_{dc}.

There are two ways to approach the problem: utilizing a quantum description, namely treating the photons as quantum objects, or assuming the ac component of the flux is a classical oscillating quantity, of the form $\Phi_{ac} = \Phi_{ac}(0)\sin(\omega t)$. We employ the first method, but compare with the expected results utilizing a classical description. The reason for doing so is that the first method is suited to also enter the quantum regime, where the coupling between the photons and the electronic system is strong and one needs to employ a polaritonic-like description. While such a case is left for a future study, we believe that the formalism developed in this chapter will be of great usefulness.

In chapter 2, we derived explicitly the response of the cavity due to its coupling to an electronic system. Here we give a brief summary of the derivation, and depict the results for the particular type of couplings found here.

The second order contribution to the electron-photon coupling can be written as $(a^\dagger)^2 + a^2 + 2n_{ph} + 1$, with $n_{ph} \equiv a^\dagger a$, and we see that the third and fourth terms renormalize the cavity frequency and the weak tunneling amplitude, respectively. The first two terms correspond to creation or annihilation of two photons, and we can disregard them in the weak coupling limit. With this approximation, we can insert this expression into the equation of motion for the photonic operator, switch to the frequency domain, and solve these equations iteratively up to second order in λ. By taking the average over the unperturbed (or uncoupled to the cavity) electronic Hamiltonian, we obtain:

$$\begin{aligned} -i\omega a = &-i(\omega_c + \lambda^2\langle D\rangle)a - \frac{\kappa}{2}a - \sqrt{\kappa}b_{in} \\ &- i\lambda^2\Pi(\omega_c)a + \lambda\langle I\rangle\,, \end{aligned} \tag{7.12}$$

where $\Pi(\omega) = \int dt \exp(i\omega t)\Pi(t)$ with

$$\Pi(t) = -i\theta(t)\langle[I(t), I(0)]\rangle\,. \tag{7.13}$$

Note that all the expectation values are taken over the electronic system in the absence of the cavity. Let us discuss briefly the resulting equation of motion and further approximations. We assume the input field b_{in} contains a large number of photons, and thus we can neglect the last term that acts as an extra input source (and which is entirely due to the current flowing through the weak link). The opposite limit, when the input field is only due to vacuum fluctuations, can in principle lead to emission of photons due to current fluctuations in the ring.

With this, we see that the coupling to the superconductor affects the cavity in two ways: by changing its frequency, and by changing its quality factor (or the escape rate κ). More precisely, we have:

$$\delta\omega = \lambda^2\left[\langle D\rangle + \mathcal{R}e\Pi(\omega_c)\right]\,, \tag{7.14}$$

$$\kappa' = \kappa - \lambda^2\mathcal{I}m\Pi(\omega_c)\,. \tag{7.15}$$

In Ref. [34, 36] we showed explicitly that the transmission τ of the cavity can be written as follows:

$$\tau \equiv \frac{b_{out}}{b_{in}} = \frac{\kappa}{-i(\omega-\omega_c)+\kappa+i\lambda^2\Pi_{tot}(\omega_c)}\,, \tag{7.16}$$

where $\Pi_{tot}(\omega_c) = \Pi(\omega_c) + \langle D\rangle$. It is instructive to rewrite the two terms in more explicit forms:

$$\langle D\rangle = \sum_n f_n\langle n|D|n\rangle\,, \tag{7.17}$$

$$\Pi(\omega) = \sum_{n\neq m}|\langle n|I|m\rangle|^2\frac{f_n - f_m}{-(\epsilon_n-\epsilon_m)+\omega+i\eta}\,, \tag{7.18}$$

where f_n is the occupation of the electronic energy state ϵ_n, and η is a small number that account for the dissipation. We can rewrite $\Pi_{tot}(\omega)$ in a more transparent form by utilizing the following sum rule [37, 97]:

$$\langle n|D|n\rangle + \sum_{m\neq n} \frac{|\langle n|I|m\rangle|^2}{\epsilon_n - \epsilon_m} = \frac{1}{2}\frac{\partial^2 \epsilon_n}{\partial \Phi^2}\,, \tag{7.19}$$

so that we obtain

$$\begin{aligned}\Pi_{tot}(\omega) = \frac{\partial I_J}{\partial \Phi} + \sum_n \frac{\partial f_n}{\partial \Phi}\frac{\partial \epsilon_n}{\partial \Phi} \\ - \omega \sum_{n\neq m} \frac{f_n - f_m}{\epsilon_n - \epsilon_m}\frac{|\langle n|I|m\rangle|^2}{(\epsilon_n - \epsilon_m) - \omega - i\eta}\,,\end{aligned} \tag{7.20}$$

where I_J is the Josephson current flowing through the ring in the presence of a dc flux. In this form, the expression for the susceptibility that is measured by the cavity (via its transmission) has the same form as the one derived previously for normal [97] and for superconducting rings [26, 37]. However, in those previous works they utilized a classical description of the ac perturbation. Moreover, they assumed the electronic system is not closed, but coupled to an external bath which leads to a finite width of the electronic levels. To make correspondence between their results and ours in such a case, we can write:

$$\begin{aligned}\Pi_{tot}(\omega) = \frac{\partial I_J}{\partial \Phi} + \frac{\omega}{\omega + i\gamma}\sum_n \frac{\partial f_n}{\partial \Phi}\frac{\partial \epsilon_n}{\partial \Phi} \\ - \omega \sum_{n\neq m} \frac{f_n - f_m}{\epsilon_n - \epsilon_m}\frac{|\langle n|I|m\rangle|^2}{(\epsilon_n - \epsilon_m) - \omega - i\gamma}\,,\end{aligned} \tag{7.21}$$

where γ is the relaxation rate of the levels (assumed, for simplicity, to be the same for all levels). We see that, in principle, there are three contributions to the cavity response: the Josephson current or non-dissipative, the diagonal or the decay of the levels, and the non-diagonal stemming from the usual Kubo contribution, respectively. In the following, we assume the zero temperature limit ($T = 0$), which in turn implies that the second term

vanishes. The first term is independent on the frequency ω, and thus any dependence on this parameter will be due to the last term.

For the classical derivation of the response we refer the reader to Refs. [37, 92, 97]. A few comments are in order. In the case of a SNS junction, the entire contribution to the cavity signal is coming from the sub gap Andreev states in the normal region, while any bulk effects can be neglected since the bulk gap is much larger than the minigap. That need not be the case for a p-wave superconductor, as this system can suffer a topological transition and close its bulk gap, which in turn should affect strongly the cavity response as a function of the magnetic flux. Thus, the energy levels in the expression for the susceptibility are the ones that correspond to the entire bulk spectrum, and not only the mini gap states.

7.2.2 *Flux dependence of the cavity response*

In Fig. 7.2, we plot separately the different contributions to the susceptibility measured by the cavity, as a function of the external flux: the Josephson current contribution (top), the real (middle) and the imaginary (bottom) non-diagonal contributions both in the topological (left column) and the non-topological phases (right column). We see that in the topological regime, all susceptibilities are Φ_0 periodic, with large amplitudes variations. The amplitude of the Φ_0 oscillations, however, diminishes as the system approaches the topological transition, and disappear after this transition, with only the $\Phi_0/2$ becoming manifest. Such $\Phi_0/2$ oscillations pertain to the normal Josephson effect, and are much smaller in amplitude, as can be seen from the top plot on the right column. We note that such oscillations exist also for the non-diagonal terms, but they are too small to be depicted (of the order 10^{-6}).

Let us now discuss the various terms contributing to the total susceptibility, as well as the effect of Majorana fermions on these quantities. As mentioned already, in the topological regime, there are Majorana fermions emerging at the edge of the ring, and which are coupled via the weak link. In a low-energy description, these Majoranas are responsible for the so called fractional Josephson effect, one of the hallmarks of the Majorana

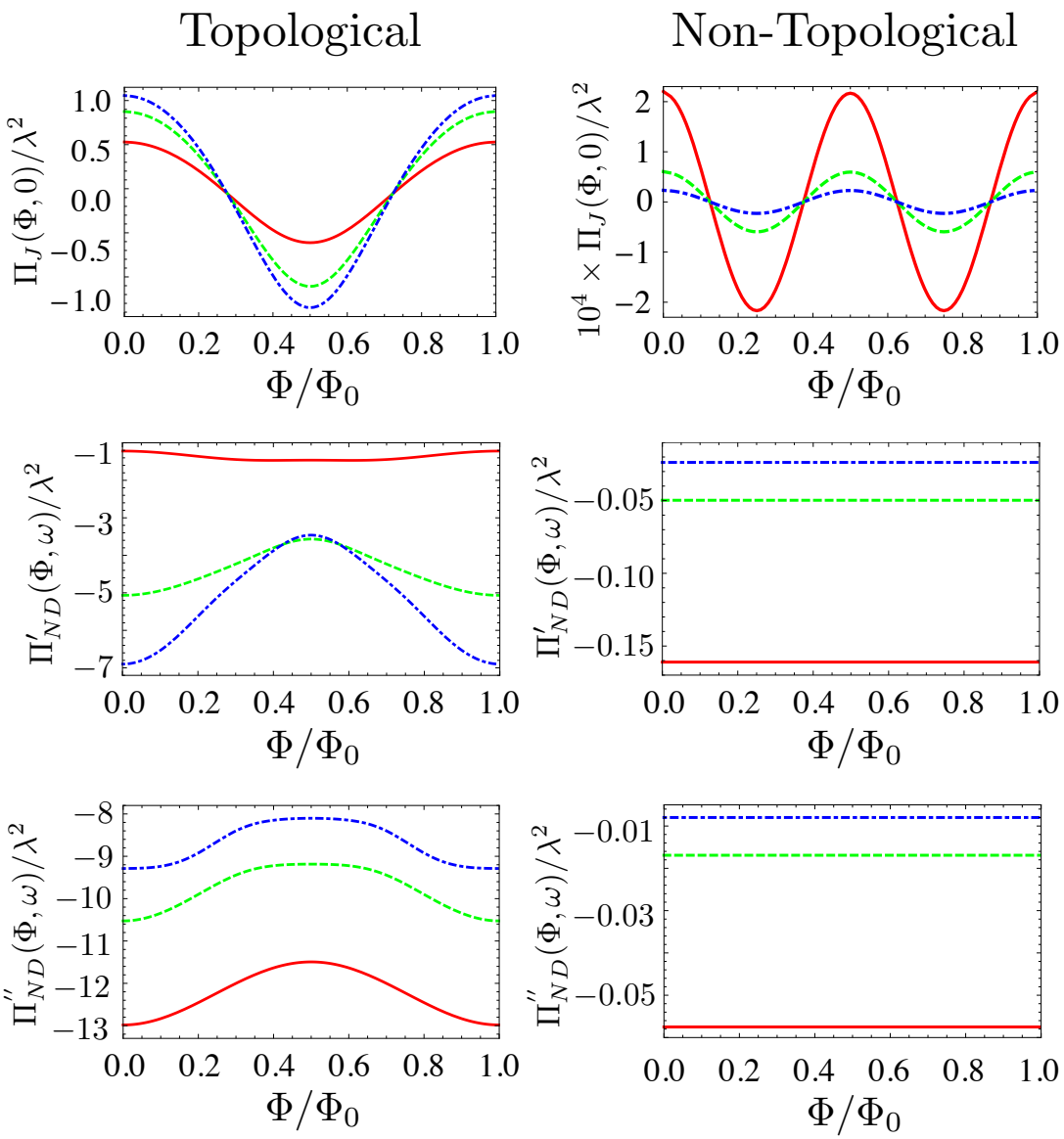

Figure 7.2: Left row (right row), from top to bottom: Dependence of the Josephson, non-diagonal real, non-diagonal imaginary susceptibilities respectively, in the topological (non-topological) region on the magnetic flux Φ/Φ_0 for $f_M = 0$. The red, green, and blue lines correspond to $\mu = -1.5$ ($\mu = -2.5$), $\mu = -1$ ($\mu = -3$), and $\mu = -0.5$ ($\mu = -3.5$), respectively. The phase transition point is at $\mu = -2$. The parameters for the plots are $\Delta = 0.1$, $t' = 0.2$, $N = 50$, and all energies are expressed in terms of $t = 1$.

fermions physics. However, the response of the cavity is sensitive not only to the presence of Majoranas, but also to the interplay between these excitations and the bulk states of the superconductor, in particular close to the topological phase transition. The first term is insensitive to such transitions, as it is given by the derivative of the persistent current with respect to the applied flux. The second term instead contains the matrix elements between the Majorana and the bulk states, it has both a real and imaginary parts, and depends on the cavity frequency ω_c. We can thus decompose it as follows:

$$\Pi_{tot}(\omega) = \Pi_{BB}(\omega) + \Pi_{BM}(\omega) + \Pi_{MM}(\omega), \tag{7.22}$$

where Π_{BB} is the part of the susceptibility that comes from the transitions between (different) bulk levels, Π_{BM} corresponds to the transitions between bulk and Majorana levels while Π_{MM} corresponds to the transitions between Majorana levels and $\Pi_{MM}(\omega) \equiv 0$ in the present setup. Note that in the non-topological regime $\Pi_{BM} = 0$, as there are no Majorana states present.

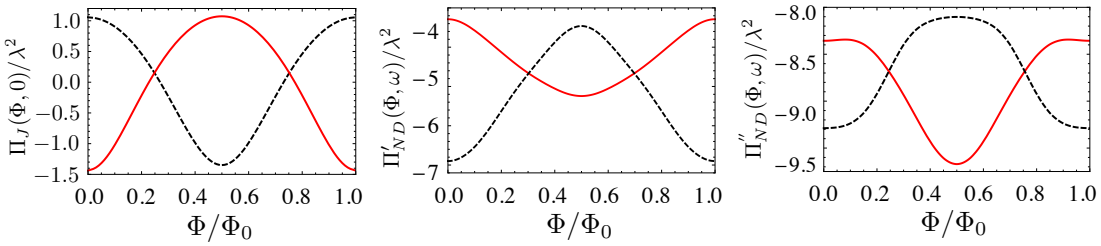

Figure 7.3: Dependence of the Josephson, non-diagonal real, and non-diagonal imaginary susceptibilities, respectively, on the magnetic flux Φ and parity f_M. The dashed-black (full-red) curves correspond to parity $f_M = 0$ ($f_M = 1$). The oscillations of the susceptibilities for the two parties are both shifted by Φ_0, as well as asymmetric in amplitudes (once superimposed). The parameters for the plots are $\mu = -0.5$, $\Delta = 0.1$, $t' = 0.2$, $N = 50$, and all energies are expressed in terms of $t = 1$.

To ascertain for the physical meaning to the oscillations of the susceptibility, it is instructive to cast this quantity in the following form:

$$\Pi_{tot}(\omega, \phi) = \sum_{j=0}^{\infty} a_j \cos\left(2\pi j \Phi/\Phi_0 + \delta\phi_j\right), \tag{7.23}$$

where a_j are (complex) Fourier coefficients of the expansion, and $\delta\phi_j$ are phase shifts, all these quantities being functions of the chemical potential μ and the gap Δ. In the topological phase, the dominant terms are a_0 and a_1, namely those corresponding to constant and Φ_0 oscillations, respectively. In the topologically trivial regime instead, $a_1 = 0$, and thus the usual Josephson effect dominates. Moreover, we find numerically that the coefficients with $j = 2p + 1$, $p = 1, 2, \ldots$ are zero above the topological transition (which does not host any Majoranas), while below such coefficients are in principle non-zero. We stress that the Josephson current has also a similar dependence on the applied flux: for a p-wave superconductor, the current $I_J(\Phi) \propto \sin(4\pi\Phi/\Phi_0)$ in the non-topological region (normal Josephson effect), while this is $I_J(\Phi) \propto \sin(2\pi\Phi/\Phi_0)$ in the topological region (fractional Josephson effect).

7.2.3 *Parity dependence*

In this section, we analyze the parity dependence of the electronic susceptibility, and implicitly of the cavity response. In Fig. 7.3, we plot the various contributions to the susceptibility in the topological regime for the two different parities of the ground state, $f_M = 0, 1$. By inspecting the plots, we can conclude that there are two main features that separate the two parities: first, the oscillations (or maxima) of the susceptibilities are shifted by Φ_0, and second, there is a strong asymmetry between the curves for the two parities, especially in the non-diagonal contribution. The shift by Φ_0 can be explained by means of the fractional Josephson effect, which is due to the presence of Majorana bound states that give rise to coherent transfer of charge e or $-e$, depending on the parity, between the two bound states. That in turn gives rise to dissipationless currents opposite in sign for the two parities, and which coincide for $\Phi = (2n + 1)\Phi_0/4$, as can be seen also from the plots. The asymmetry of the Josephson contribution can be explained by inspecting the expression for the supercurrent flow: $I_J = \sum_{n=bulk} i_n + (-1)^{f_M} i_M$, i.e. the bulk contribution is constant, as its parity is assumed unchanged, while the Majorana contribution depends on the parity of the ground state $f_M = 0, 1$. The non-diagonal susceptibility shows a much stronger asymmetry, and it is due to an interplay between

the occupancy of the Majorana and the matrix elements of the current operator I between the Majorana and the bulk states, or simply by Π_{BM} given by:

$$\Pi_{BM}(\omega) = -\omega \sum_{n \neq M} \frac{f_n - f_M}{\epsilon_n - \epsilon_M} \frac{|\langle n|I|M\rangle|^2}{(\epsilon_n - \epsilon_M) - \omega - i\gamma}, \tag{7.24}$$

where M stands for the Majorana.

7.2.4 *Frequency dependence*

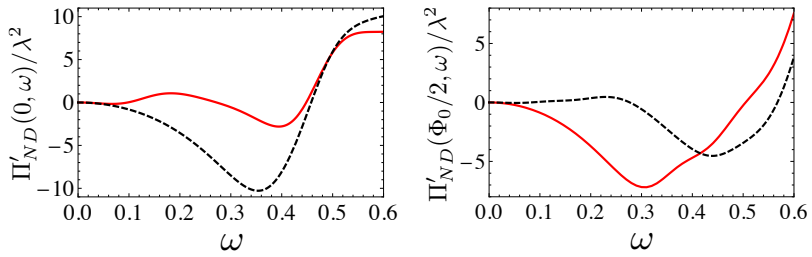

Figure 7.4: Dependence of the real part of the non-diagonal susceptibility on the frequency ω for two values of the external flux, $\Phi = 0$ (left) and $\Phi = \Phi_0/2$ (right), and for the two parity states $f_M = 0$ (dashed-black) and $f_M = 1$ (full-red) lines, respectively. The parameters for the plots are: $\mu = -0.5$, $\Delta = 0.1$, $t' = 0.5$, $N = 50$, and all energies are expressed in terms of $t = 1$.

Finally, we discuss briefly the frequency dependence of the susceptibility (thus of the cavity response) for different parity and flux realizations, respectively. We note that the Josephson contribution is frequency independent, and the only dependence on ω arises from the non-diagonal susceptibility. In Fig. 7.4, we plot the real part of the non-diagonal susceptibility as a function of the frequency in the topological regime, and for the two different parities. The non-monotonic behavior of the curves can be related to the resonance condition when the frequency ω matches the effective p-wave gap and the sign of the susceptibility changes. Interestingly, the dependence on ω is different for different parities $f_M = 0, 1$ and for different values of the magnetic flux Φ. Such features can again be traced back to the dependence of Π_{BM} on both the flux and the parity of the topological

superconductor. We note, however, that the curves become identical (not shown) at flux values $\Phi = (2n+1)\Phi_0/4$, with $n = 0, 1, \ldots$, at which instances the degeneracy of the Majorana energy levels is restored.

7.3 CONCLUSIONS

In this chapter, we studied theoretically a Kitaev ring interrupted by a weak link and pierced by a magnetic flux, and coupled inductively to a microwave cavity. We established an input-output description for the cavity transmission, and show that the cavity response depends strongly on various electronic parameters, such as the chemical potential, the magnetic flux, and the parity of the superconducting ground state. We found a 4π (2π) variation of the cavity response with respect to the external magnetic flux in the topological (trivial) phase, and related such dependence to the fractional (normal) Josephson effect. As opposed to previous works, our theory takes into account, on equal footing, the low-energy Majorana modes, the gaped bulk states, and the interplay between these states in the presence of the cavity. Such a description allows one to describe not only the superconducting ring deep in the topological regime, but also the topological transition, and the crossover from the fractional to the normal Josephson effect in the presence of a magnetic flux.

As an experimental realization of the Kitaev model in the topology of the ring, we propose to use a nanowire with spin-orbit interaction in proximity of s-wave superconductor and subject to magnetic field. We propose to use a nanowire connected to the leads to form a junction, similar to experimental realization in [1]. The implementation of the inductive coupling via a magnetic flux can be done in a SQUID geometry, such as in [76], where the supercurrent in a carbon nanotube was investigated. The main difference between such a spin-orbit coupled nanowire model and the Kitaev chain is the number of states, which is doubled, as one needs to account for the spin degree of freedom. We strongly believe, based on our previous findings in Ref. [34], that our main results on the visualization of the transition from the fractional to the normal Josephson effect by utilizing a microwave cavity are robust.

8

CONCLUSIONS AND PERSPECTIVES

In this thesis, we have studied how the measurement of the cavity microwave field can be used to extract information on the properties of the nanostructures coupled to the cavity. Current experiments allow to implement on-chip mesoscopic circuits coupled to high finesse resonators and to measure extremely small variations of the amplitude of the microwave optical signal. Cavity QED is an experimental technique that allows to study and manipulate atoms, superconducting qubits and quantum dots coupled to a microwave cavity. Using input-output theory [20] in case of weak coupling between the electronic system and the photonic field in the cavity, we have related the transmission coefficient of the cavity to the electronic susceptibility of the nanostructure. The frequency shift is proportional to the real part of the electronic susceptibility while the frequency broadening is proportional to the imaginary part of the susceptibility. In this thesis, this general framework is applied to four specific mesoscopic conductors: a tunnel junction, a quantum dot coupled to the leads, a one-dimensional topological wire and a superconducting ring.

First, we studied a tunnel junction and a quantum dot tunnel coupled to metallic leads embedded in a microwave cavity. For the tunnel junction, the imaginary part of the susceptibility is directly proportional to the differential conductance $\mathrm{d}I/\mathrm{d}V$. We demonstrated that for the quantum dot tunnel coupled to the metallic leads, the phase shift is proportional to the imaginary part of the admittance far from quantum dot resonance. For symmetric lead-cavity coupling, equal tunneling and low-frequency, the phase shift is proportional to the real part of the admittance, or $\mathrm{d}I/\mathrm{d}V$. In the general case, there is no direct relation between optical observables, such as phase shift and frequency broadening, and transport quantities, such as differential conductance. Therefore, the transmission coefficient of the cavity gives access to finite frequency admittance of the quantum dot thus providing new information about the quantum conductor coupled to the cavity.

We have developed a formalism relating the electronic susceptibility to the optical transmission of the cavity. In addition to the mesoscopic conductors studied here in detail, our formalism is applicable to more complicated mesoscopic systems coupled to the cavity. More specifically, further research should focus on a system with two out-of-equilibrium quantum dots coupled to the same microwave cavity. In such system, the cavity can be used to both induce and probe the correlated transport. Our formalism may allow to detail theoretically the behavior of the two quantum dots system, which is a universal gate ubiquitous for quantum computing. In a further perspective, our approach may shed more light on general quantum dot architecture.

Moreover, we propose to use the methods of cavity QED to study topological superconductors that can host Majorana fermions. We considered different theoretical models of topological superconductors with nearest-neighbor and next-nearest-neighbor hoppings that give rise to one or two Majorana fermions at each end of the wire, respectively. Using the photonic field of the cavity, within a single set of measurements, one can determine the topological transition point and the emergence of the Majorana fermions. One can also measure, in the same set, the parity of the ground state, the quantity of crucial interest for quantum computing with Majorana fermions, which is impossible to probe electronically since the transport inherently modifies the number of electrons in the system.

At the same time, cavity QED can be used to probe DC fractional Josephson effect. We continued by studying a superconducting ring with a weak link coupled to a microwave cavity. The ring is subject to both a DC magnetic flux, and an AC flux from the cavity, which gives rise to a coupling between the ring and cavity. We demonstrated that the electronic susceptibility has different periodicity as a function of magnetic flux in topological and non-topological regions. Different periodicity allows to probe the fractional Josephson effect, which is associated with the emergence of the Majorana fermions in the system. As opposed to previous works, our theory takes into account both the low-energy Majorana modes and the bulk states, thus allowing to visualize the transition from the fractional to the normal Josephson effect.

As we demonstrated, cavity QED methods can be used to extensively study 1D topological structures. We propose to generalize these methodology to theoretically investigate

2D systems, such as 2D superconductors or 2D topological insulators that have seen large interest in recent experimental studies [103]. Furthermore, we suggest that a generalization of the input-output theory for a 2D system may allow to characterize theoretically the braiding of Majorana fermions.

In a broader perspective, we propose to manipulate electronic properties with light. The strong coupling between the electronic system and the electric field in the cavity enables such manipulation. Qubits — basic units for quantum computing — can be entangled, controled and measured in the strong-coupling regime. An experimental implementation of a superconducting qubit as a Cooper pair box has been already studied in the strong-coupling regime [101]. A quantum dot can also serve as a physical implementation of the qubit [58] as follows. The quantum dot with a single electron can be constructed by tuning the gate voltage. And the spin of this electron can encode a qubit. Several experiments have implemented the coupling between the spin qubit and photons inside a cavity [72, 99]. Cavity QED architecture allows to construct distant spin qubits that can be entangled thus allowing to implement two-qubit quantum algorithms. In order to obtain information about the spin dynamics and the parameters of the qubits, such as spin dephasing time, we suggest to define the spin susceptibility for spin qubit systems in the strong-coupling regime similarly to the electronic susceptibility.

Finally, cavity QED allows to study various mixed electron-photon states, including new topological states created by the interaction between light and matter. For instance, the Floquet topological insulator, which was constructed by applying a classical AC drive [56] to create topological electronic band structure. Coupling a single photon to an exciton leads to the emergence of a novel topological state, when a topological polariton (topolariton) [48] is formed. The topolariton is a kind of polariton — a quasiparticle formed by photons and electrical dipoles that emerge in the strong light-matter coupling regime [16]. It is characterized by the formation of chiral edge states in the excitation spectrum. Generally, we expect the methods of cavity QED to generalize for probing any polaritons. As a direct extension of the current work, we plan to apply cavity QED to theoretically investigate "Majorana polaritons" which are highly entangled electron-photon degenerate states that may appear under a strong coupling between a single photon and Majorana

fermions in a topological wire [96]. This particular system gives us a pertinent example for tackling the broader problem of theoretically describing the transition from the classical regime to the quantum regime: we can study the creation of Majorana polariton by applying a classical AC field as well as by coupling it to a cavity. Extensively studying both the classical and quantum description as well as the relation between them may help us shed some extra light on the fundamental relation between classical physics and quantum mechanics.

APPENDIX A

In this appendix, we provide more details on the input-output theory. We consider a one-sided cavity ($\kappa_2 = 0$ in Fig. 2.5) with a resonance frequency ω_c [20]. The Hamiltonian that describes the system reads

$$H = H_{sys} + H_{bath} + H_{int}, \tag{A.1}$$

where the bath Hamiltonian is given by

$$H_{bath} = \sum_q \omega_q b_q^\dagger b_q, \tag{A.2}$$

and the coupling Hamiltonian (withing the rotating wave approximation) reads

$$H_{int} = -i \sum_q \left[f_q a^\dagger b_q - f_q^* b_q^\dagger a \right]. \tag{A.3}$$

The Heisenberg equation of motion (EOM) for the cavity mode is

$$\dot{a} = i \left[H, a \right], \tag{A.4}$$

where

$$[H_{int}, a] = i \sum_q f_q b_q. \tag{A.5}$$

Introducing Eq.A.5 into Eq.A.4 we obtain

$$\dot{a} = i\,[H_{sys}, a] - \sum_q f_q b_q. \tag{A.6}$$

The EOM for the bath variables reads

$$\dot{b_q} = i\,[H, b_q] = -i\omega_q b_q + f_q^* a, \tag{A.7}$$

which is the EOM of a harmonic oscillator driven by the motion of the cavity degrees of freedom. For $t_0 < t$ being a time in the distant past, the solution of Eq.A.7 can be written as

$$b_q(t) = e^{-i\omega_q(t-t_0)} b_q(t_0) + \int_{t_0}^{t} d\tau e^{-i\omega_q(t-\tau)} f_q^* a(\tau). \tag{A.8}$$

Introducing Eq.(A.8) into the last term in Eq.(A.6), we obtain

$$\begin{aligned}\sum_q f_q b_q &= \sum_q f_q \left[e^{-i\omega_q(t-t_0)} b_q(t_0) + \int_{t_0}^{t} d\tau e^{-i\omega_q(t-\tau)} f_q^* a(\tau) \right] \\ &= \sum_q f_q e{-}i\omega_q(t-t_0) b_q(t_0) + \sum_q |f_q|^2 \int_{t_0}^{t} d\tau e^{-i(\omega_q-\omega_c)(t-\tau)} e^{i\omega_c(\tau-t)} a(\tau),\end{aligned} \tag{A.9}$$

where the last term in square brackets is a slowly varying function of τ.

$$\kappa(\omega_c) = 2\pi \sum_q |f_q|^2 \, \delta(\omega_c - \omega_q) \tag{A.10}$$

so that

$$\int_{-\infty}^{\infty} \frac{d\nu}{2\pi} \kappa(\omega_c + \nu) e^{-i\nu(t-\tau)} = \sum_q |f_q|^2 \, e^{-i(\omega_q - \omega_c)(t-\tau)}. \tag{A.11}$$

Performing the Markov approximation, Eq.(A.11) reads

$$\sum_q |f_q|^2 \, e^{-i(\omega_q - \omega_c)(t-\tau)} = \kappa\delta(t-\tau) \tag{A.12}$$

and

$$\sum_q f_q b_q = \sum_q f_q e^{-i\omega_q(t-t_0)} b_q(t_0) + \kappa \int_{t_0}^{t} d\tau \delta(t-\tau) e^{i\omega_c(\tau - t)} a(\tau) \tag{A.13}$$

Using

$$\int_{-\infty}^{x_0} dx \delta(x - x_0) = \frac{1}{2} \tag{A.14}$$

we obtain

$$\sum_q f_q b_q = \sum_q f_q e^{-i\omega_q(t-t_0)} b_q(t_0) + \frac{\kappa}{2} a(t). \tag{A.15}$$

The cavity EOM reads

$$\dot{a} = i\,[H_{sys}, a] - \sum_q f_q e^{-i\omega_q(t-t_0)} b_q(t_0) - \frac{\kappa}{2} a, \tag{A.16}$$

where the last term is a linear damping term for the cavity mode. Assuming $f \equiv \sqrt{|f_q|^2}$ being a constant and defining the density of states by $\rho = \sum_q \delta(\omega_c - \omega_q)$, the decay rate becomes

$$\kappa = 2\pi f^2 \rho = 2\pi f^2 \sum_q \delta(\omega_c - \omega_q). \tag{A.17}$$

We can now define the input mode

$$b_{in}(t) = \frac{1}{\sqrt{2\pi\rho}} \sum_q e^{-i\omega_q(t-t_0)} b_q(t_0). \tag{A.18}$$

Finally, the cavity EOM reads

$$\dot{a} = i\,[H_{sys}, a] - \frac{\kappa}{2} a - \sqrt{\kappa} b_{in}. \tag{A.19}$$

Let us define the output mode $b_{out}(t)$ that is radiated into the bath. For $t_1 > t$ being a time in the distant future after the input field $b_{in}(t)$ has interacted with the cavity, the solution of Eq.(A.7) in terms of the final condition of the bath reads

$$b_q(t) = e^{-i\omega_q(t-t_1)} b_q(t_1) - \int_t^{t_1} d\tau e^{-i\omega_q(t-\tau)} f_q^* a(\tau). \tag{A.20}$$

Defining the output mode as

$$b_{out}(t) = \frac{1}{\sqrt{2\pi\rho}} \sum_q e^{-i\omega_q(t-t_1)} b_q(t_1), \tag{A.21}$$

we obtain

$$\dot{a} = i\,[H_{sys}, a] + \frac{\kappa}{2} a - \sqrt{\kappa} b_{out}. \tag{A.22}$$

Subtracting Eq.(A.22) from Eq.(A.19) we obtain that

$$b_{out}(t) = b_{in}(t) + \sqrt{\kappa} a(t), \tag{A.23}$$

a result which holds for any general cavity Hamiltonian.

B

APPENDIX B

B.1 SCATTERING MATRIX APPROACH FOR A NON-INTERACTING QUANTUM CONDUCTOR

In this section, we express the charge susceptibility of a non-interacting quantum conductor in terms of integral over the elements of its S matrix.

The electron number operator in terms of the current operator reads

$$n_\alpha(t) = \frac{i}{2\pi}\int_{-\infty}^{\infty} d\omega \exp(-i\omega t)\frac{1}{\omega}\int_{-\infty}^{\infty} dE \sum_{\gamma\gamma'} A_{\gamma\gamma'}(\alpha, E, E+\omega) a^\dagger_\gamma(E) a_{\gamma'}(E+\omega), \tag{B.1}$$

where $A_{\gamma\gamma'}$ have been defined in Eq. (4.16). We can now calculate $\Pi_{\alpha\beta}(\omega) \equiv F_{\alpha\beta}(\omega) + X_{\alpha\beta}(\omega)$ with

$$F_{\alpha\beta}(t) = -i\theta(t)\langle n_\alpha(t) n_\beta(0)\rangle, \tag{B.2}$$

$$X_{\alpha\beta}(t) = i\theta(t)\langle n_\beta(0) n_\alpha(t)\rangle. \tag{B.3}$$

Let us first start with $F_{\alpha\beta}(\omega) = -i\int_0^\infty dt e^{i\omega t}\langle n_\alpha(t) n_\beta(0)\rangle$. Using Eq. (B.1) and applying Wick's theorem, we obtain

$$F_{\alpha\beta}(\omega) = \left(\frac{1}{2\pi}\right)^2 \int_{-\infty}^{\infty}\int_{-\infty}^{\infty} d\omega_2 dE_2 \Bigg\{ \frac{1}{\omega_2^2}\frac{1}{\omega+\omega_2+i\eta}\times$$
$$\sum_{\gamma_1,\gamma_1'} A_{\gamma_1\gamma_1'}(\alpha, E_2+\omega_2, E_2) A_{\gamma_1'\gamma_1}(\beta, E_2, E_2+\omega_2)\times$$
$$\times f_{\gamma_1}(E_2+\omega_2)\left[1-f_{\gamma_1'}(E_2)\right]\Bigg\}. \tag{B.4}$$

In the same way we can calculate $X_{\alpha\beta}(\omega)$:

$$X_{\alpha\beta}(\omega) = -\left(\frac{1}{2\pi}\right)^2 \int_{-\infty}^{\infty}\int_{-\infty}^{\infty} d\omega_2 dE_2 \Bigg\{ \frac{1}{\omega_2^2}\frac{1}{\omega+\omega_2+i\eta}$$
$$\times \sum_{\gamma_1,\gamma_1'} A_{\gamma_1\gamma_1'}(\alpha, E_2+\omega_2, E_2) A_{\gamma_1'\gamma_1}(\beta, E_2, E_2+\omega_2)\times$$
$$\times f_{\gamma_1'}(E_2)\left[1-f_{\gamma_1}(E_2+\omega_2)\right]\Bigg\}. \tag{B.5}$$

And finally $\Pi_{\alpha\beta}(\omega)$ reads

$$\Pi_{\alpha\beta}(\omega) = \left(\frac{1}{2\pi}\right)^2 \int_{-\infty}^{\infty}\int_{-\infty}^{\infty} d\omega_2 dE_2 \left\{ \frac{1}{\omega_2^2}\frac{1}{\omega+\omega_2+i\eta}\times \right.$$
$$\left. \sum_{\gamma_1,\gamma_1'} F^{\alpha\beta}_{\gamma_1\gamma_1'}(E_2,\omega_2)\left[f_{\gamma_1}(E_2+\omega_2)-f_{\gamma_1'}(E_2)\right]\right\}. \tag{B.6}$$

where we introduced

$$F^{\alpha\beta}_{\gamma\gamma'} = A_{\gamma\gamma'}(\alpha, E+\omega, E) A_{\gamma'\gamma}(\beta, E, E+\omega). \tag{B.7}$$

At zero temperature $T = 0$, we can further simplify Eq. (B.6) and using the identity

$$\frac{1}{\omega+\omega_2+i\eta} = \mathcal{P}\left(\frac{1}{\omega+\omega_2}\right) - i\pi\delta(\omega+\omega_2), \tag{B.8}$$

we obtain Eq. (4.25) and Eq. (4.24).

B.2 CALCULATION OF THE QUANTUM DOT SUSCEPTIBILITY

B.2.1 *Expressions of the intermediate* $F^{\gamma\gamma'}_{\alpha\beta}$ *functions*

In order to calculate the charge susceptibility for the quantum dot, we need the sixteen functions $F^{\gamma\gamma'}_{\alpha\beta}$ which are given by

$$\begin{aligned} F^{LL}_{LL}(E,\omega) &= A_{LL}(L,E+\omega,E)A_{LL}(L,E,E+\omega) \\ &= |g(E)g(E+\omega)|^2\left(\Gamma_L^2\Gamma_R^2+\omega^2\Gamma_L^2\right), \end{aligned} \tag{B.9}$$

$$\begin{aligned} F^{RR}_{LL}(E,\omega) &= A_{LL}(R,E+\omega,E)A_{LL}(R,E,E+\omega) \\ &= |g(E)g(E+\omega)|^2\,\Gamma_L^2\Gamma_R^2, \end{aligned} \tag{B.10}$$

$$\begin{aligned} F^{LR}_{LL}(E,\omega) &= A_{LL}(L,E+\omega,E)A_{LL}(R,E,E+\omega) \\ &= -|g(E)g(E+\omega)|^2\left(\Gamma_L^2\Gamma_R^2+i\omega\Gamma_L^2\Gamma_R\right), \end{aligned} \tag{B.11}$$

$$\begin{aligned} F^{RL}_{LL}(E,\omega) &= A_{LL}(R,E+\omega,E)A_{LL}(L,E,E+\omega) \\ &= -|g(E)g(E+\omega)|^2\left(\Gamma_L^2\Gamma_R^2-i\omega\Gamma_L^2\Gamma_R\right), \end{aligned} \tag{B.12}$$

$$\begin{aligned} F^{LL}_{RR}(E,\omega) &= A_{RR}(L,E+\omega,E)A_{RR}(L,E,E+\omega) \\ &= |g(E)g(E+\omega)|^2\,\Gamma_L^2\Gamma_R^2, \end{aligned} \tag{B.13}$$

$$\begin{aligned} F^{RR}_{RR}(E,\omega) &= A_{RR}(R,E+\omega,E)A_{RR}(R,E,E+\omega) \\ &= |g(E)g(E+\omega)|^2\left(\Gamma_L^2\Gamma_R^2+\omega^2\Gamma_R^2\right), \end{aligned} \tag{B.14}$$

$$\begin{aligned} F^{LR}_{RR}(E,\omega) &= A_{RR}(L,E+\omega,E)A_{RR}(R,E,E+\omega) \\ &= -|g(E)g(E+\omega)|^2\left(\Gamma_L^2\Gamma_R^2-i\omega\Gamma_R^2\Gamma_L\right), \end{aligned} \tag{B.15}$$

$$\begin{aligned} F^{RL}_{RR}(E,\omega) &= A_{RR}(R,E+\omega,E)A_{RR}(L,E,E+\omega) \\ &= -|g(E)g(E+\omega)|^2\left(\Gamma_L^2\Gamma_R^2+i\omega\Gamma_R^2\Gamma_L\right), \end{aligned} \tag{B.16}$$

$$\begin{aligned} F^{LL}_{LR}(E,\omega) &= A_{LR}(L,E+\omega,E)A_{RL}(L,E,E+\omega) \\ &= -|g(E)g(E+\omega)|^2\,\Gamma_L^2\Gamma_R^2+|g(E)|^2\,\Gamma_L\Gamma_R, \end{aligned} \tag{B.17}$$

$$\begin{aligned} F^{RR}_{LR}(E,\omega) &= A_{LR}(R,E+\omega,E)A_{RL}(R,E,E+\omega) \\ &= -|g(E)g(E+\omega)|^2\,\Gamma_L^2\Gamma_R^2+|g(E+\omega)|^2\,\Gamma_L\Gamma_R, \end{aligned} \tag{B.18}$$

$$
\begin{aligned}
F^{LR}_{LR}(E,\omega) &= A_{LR}(L,E+\omega,E)A_{RL}(R,E,E+\omega)\\
&= |g(E)g(E+\omega)|^2\,\Gamma_L^2\Gamma_R^2 - g(E)g(E+\omega)\Gamma_L\Gamma_R\\
&- i\Gamma_L\Gamma_R\,|g(E)g(E+\omega)|^2\left(\frac{\Gamma_R}{g^*(E+\omega)}+\frac{\Gamma_L}{g^*(E)}\right)\\
&= |g(E)g(E+\omega)|^2\left[\Gamma_L^2\Gamma_R^2 - \Gamma_L\Gamma_R\Big(E^2+E\omega-2E\epsilon_d\right.\\
&\left.- \epsilon_d\omega+\epsilon_d^2+\Gamma^2/4-i\Gamma_L\omega/2+i\Gamma_R\omega/2\Big)\right]\\
&= |g(E)g(E+\omega)|^2\left[\Gamma_L^2\Gamma_R^2 - \Gamma_L\Gamma_R\Big((E-\epsilon_d)\right.\\
&\left.\times(E+\omega-\epsilon_d)+\Gamma^2/4-i\Gamma_L\omega/2+i\Gamma_R\omega/2\Big)\right],
\end{aligned}
\tag{B.19}
$$

$$
\begin{aligned}
F^{RL}_{LR}(E,\omega) &= A_{LR}(R,E+\omega,E)A_{RL}(L,E,E+\omega)\\
&= |g(E)g(E+\omega)|^2\,\Gamma_L^2\Gamma_R^2 - g^*(E)g^*(E+\omega)\Gamma_L\Gamma_R\\
&+ i\Gamma_L\Gamma_R\,|g(E)g(E+\omega)|^2\left(\frac{\Gamma_R}{g(E+\omega)}+\frac{\Gamma_L}{g(E)}\right)\\
&= |g(E)g(E+\omega)|^2\left[\Gamma_L^2\Gamma_R^2 - \Gamma_L\Gamma_R\Big(E^2+E\omega-2E\epsilon_d\right.\\
&\left.- \epsilon_d\omega+\epsilon_d^2+\Gamma^2/4+i\Gamma_L\omega/2-i\Gamma_R\omega/2\Big)\right]\\
&= |g(E)g(E+\omega)|^2\left[\Gamma_L^2\Gamma_R^2 - \Gamma_L\Gamma_R\Big((E-\epsilon_d)\right.\\
&\left.\times(E+\omega-\epsilon_d)+\Gamma^2/4+i\Gamma_L\omega/2-i\Gamma_R\omega/2\Big)\right],
\end{aligned}
\tag{B.20}
$$

$$
\begin{aligned}
F^{LL}_{RL}(E,\omega) &= A_{RL}(L,E+\omega,E)A_{LR}(L,E,E+\omega)\\
&= -|g(E)g(E+\omega)|^2\,\Gamma_L^2\Gamma_R^2 + |g(E+\omega)|^2\,\Gamma_L\Gamma_R,
\end{aligned}
\tag{B.21}
$$

$$
\begin{aligned}
F^{RR}_{RL}(E,\omega) &= A_{RL}(R,E+\omega,E)A_{LR}(R,E,E+\omega)\\
&= -|g(E)g(E+\omega)|^2\,\Gamma_L^2\Gamma_R^2 + |g(E)|^2\,\Gamma_L\Gamma_R,
\end{aligned}
\tag{B.22}
$$

$$
\begin{aligned}
F^{LR}_{RL}(E,\omega) &= A_{RL}(L,E+\omega,E)A_{LR}(R,E,E+\omega)\\
&= |g(E)g(E+\omega)|^2\,\Gamma_L^2\Gamma_R^2 - g^*(E)g^*(E+\omega)\Gamma_L\Gamma_R\\
&+ i\Gamma_L\Gamma_R\,|g(E)g(E+\omega)|^2\left(\frac{\Gamma_R}{g(E)}+\frac{\Gamma_L}{g(E+\omega)}\right)\\
&= |g(E)g(E+\omega)|^2\left[\Gamma_L^2\Gamma_R^2 - \Gamma_L\Gamma_R\Big(E^2+E\omega-2E\epsilon_d\right.\\
&\left.- \epsilon_d\omega+\epsilon_d^2+\Gamma^2/4-i\Gamma_L\omega/2+i\Gamma_R\omega/2\Big)\right]\\
&= |g(E)g(E+\omega)|^2\left[\Gamma_L^2\Gamma_R^2 - \Gamma_L\Gamma_R\Big((E-\epsilon_d)\right.\\
&\left.\times(E+\omega-\epsilon_d)+\Gamma^2/4-i\Gamma_L\omega/2+i\Gamma_R\omega/2\Big)\right],
\end{aligned}
\tag{B.23}
$$

$$
\begin{aligned}
F^{RL}_{RL}(E,\omega) &= A_{RL}(R,E+\omega,E)A_{LR}(L,E,E+\omega)\\
&= |g(E)g(E+\omega)|^2\,\Gamma_L^2\Gamma_R^2 - g(E)g(E+\omega)\Gamma_L\Gamma_R\\
&- i\Gamma_L\Gamma_R\,|g(E)g(E+\omega)|^2\left(\frac{\Gamma_R}{g^*(E)}+\frac{\Gamma_L}{g^*(E+\omega)}\right)\\
&= |g(E)g(E+\omega)|^2\left[\Gamma_L^2\Gamma_R^2 - \Gamma_L\Gamma_R\Big(E^2+E\omega-2E\epsilon_d\right.\\
&\left.- \epsilon_d\omega+\epsilon_d^2+\Gamma^2/4+i\Gamma_L\omega/2-i\Gamma_R\omega/2\Big)\right]\\
&= |g(E)g(E+\omega)|^2\left[\Gamma_L^2\Gamma_R^2 - \Gamma_L\Gamma_R\Big((E-\epsilon_d)\right.\\
&\left.\times(E+\omega-\epsilon_d)+\Gamma^2/4+i\Gamma_L\omega/2-i\Gamma_R\omega/2\Big)\right].
\end{aligned}
\tag{B.24}
$$

B.2.2 *Expressions of the intermediate $K_{\alpha\beta}$ functions*

Let us introduce the following dimensionless variables

$$a = \frac{eV - 2\epsilon_d}{\Gamma}, \quad b = \frac{2\epsilon_d + eV}{\Gamma}, \quad x = \frac{2\omega_2}{\Gamma} \text{ and } y = \frac{2\omega}{\Gamma}. \tag{B.25}$$

The functions $K_{\alpha\beta}$ take the following form:

$$K_{LL}(x) = -\frac{2\Gamma_L}{\Gamma\left(x^2+4\right)}\Bigg(\left(x^2\Gamma + 4\Gamma_R\right)\left[\arctan\left(a+x\right) - \arctan\left(a-x\right)\right] + \Gamma_L x\left[-2\log\left(1+a^2\right) + \log\left[1+\left(a+x\right)^2\right] + \log\left[1+\left(a-x\right)^2\right]\right]\Bigg), \tag{B.26}$$

$$K_{RR}(x) = -\frac{2\Gamma_R}{\Gamma\left(x^2+4\right)}\Bigg(\left(x^2\Gamma + 4\Gamma_L\right)\left[\arctan\left(b+x\right) - \arctan\left(b-x\right)\right] + \Gamma_R x\left[-2\log\left(1+b^2\right) + \log\left[1+\left(b+x\right)^2\right] + \log\left[1+\left(b-x\right)^2\right]\right]\Bigg), \tag{B.27}$$

$$\begin{aligned} K_{LR}(x) = -\frac{\Gamma_L\Gamma_R}{\Gamma\left(x^2+4\right)}\Bigg(& -2i(x-2i)\left[\arctan\left(a+x\right) - \arctan\left(a-x\right)\right] \\ & + 2i(x+2i)\left[\arctan\left(b+x\right) - \arctan\left(b-x\right)\right] \\ & + (x-2i)\left[-2\log\left(1+a^2\right) + \log\left[1+\left(a+x\right)^2\right] + \log\left[1+\left(a-x\right)^2\right]\right] \\ & + (x+2i)\left[-2\log\left(1+b^2\right) + \log\left[1+\left(b+x\right)^2\right] + \log\left[1+\left(b-x\right)^2\right]\right]\Bigg), \end{aligned} \tag{B.28}$$

$$
\begin{aligned}
K_{RL}(x) = -\frac{\Gamma_L \Gamma_R}{\Gamma\left(x^2+4\right)}\Bigg(& -2i(x-2i)\left[\arctan\left(b+x\right)-\arctan\left(b-x\right)\right] \\
& +2i(x+2i)\left[\arctan\left(a+x\right)-\arctan\left(a-x\right)\right] \\
& +(x-2i)\left[-2\log\left(1+b^2\right)+\log\left[1+(b+x)^2\right]+\log\left[1+(b-x)^2\right]\right] \\
& +(x+2i)\left[-2\log\left(1+a^2\right)+\log\left[1+(a+x)^2\right]+\log\left[1+(a-x)^2\right]\right]\Bigg),
\end{aligned}
\tag{B.29}
$$

The functions $K_{\alpha\beta}$ directly provide $\Pi''_{\alpha\beta}$.

B.2.3 *Calculation of the real part of the susceptibility*

We give technical details on how to compute the real part of the charge susceptibility. Let us compute one of the integrals

$$
L(y) = 2i\mathcal{P}\int_{-\infty}^{\infty} \frac{dx}{x^2(x+y)(x^2+4)} f(x), \tag{B.30}
$$

where

$$
f(x) = \arctan(a+x) - \arctan(a-x). \tag{B.31}
$$

Using the decomposition

$$
\arctan(\alpha+x) = \frac{1}{2i}\left(\log[1+i(\alpha+x)] - \log[1-i(\alpha+x)]\right), \tag{B.32}
$$

the function $f(x)$ can be given the following alternative form

$$
\begin{aligned}
f(x) = & \frac{1}{2i}\left[\log\left(1+\frac{ix}{1+ia}\right)+\log\left(1+\frac{ix}{1-ia}\right)\right. \\
& \left.-\log\left(1-\frac{ix}{1+ia}\right)-\log\left(1-\frac{ix}{1-ia}\right)\right].
\end{aligned}
\tag{B.33}
$$

Therefore, $L(y)$ can be written as a sum over four integrals. Let us detail the calculation of one of them. We consider the following principal part integral

$$L_1(y) = \mathcal{P}\int_{-\infty}^{\infty} \frac{dx}{x^2(x+y)(x+2i)(x-2i)} \times \log\left(1+\frac{ix}{1+ia}\right). \tag{B.34}$$

$L_1(y)$ can be computed with standard complex plane integration techniques. The integrand has five singularities in the complex plane: poles at $z = 0$, $z = -y$, $z = -2i$, $z = 2i$ and a branch point at $z = i - a$. A semi-circle is added around $z = 0$ and $z = -y$. The contour is closed in the lower half-plane, avoiding both the pole at $z = 2i$ and the branch cut [Fig. B.1].

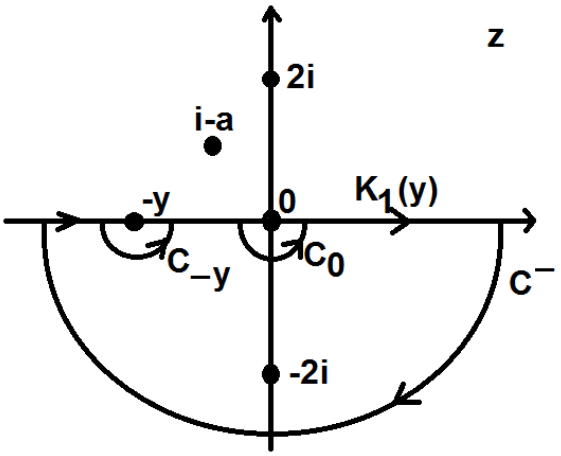

Figure B.1: Complex plane z with poles of the integrand, Eq.(B.34).

Using Cauchy's residue theorem, we obtain eventually:

$$-2\pi i \mathrm{Res}[-2i] = \int_{C^-} = L_1(y) + \int_{C_{-y}} + \int_{C_0} + \int_{C_R} \tag{B.35}$$

where

$$L_1(y) = -\pi i \left(2\mathrm{Res}[-2i] + \mathrm{Res}[-y] + \mathrm{Res}^{(2)}[0]\right), \tag{B.36}$$

and

$$\mathrm{Res}[-y] = \frac{1}{y^2(y^2+4)} \log\left(1 - \frac{iy}{1+ia}\right), \tag{B.37}$$

$$\mathrm{Res}[-2i] = \frac{1}{16i(y-2i)} \log\left(1 + \frac{2}{1+ia}\right), \tag{B.38}$$

$$\mathrm{Res}^{(2)}[0] = \frac{i}{4y(1+ia)}. \tag{B.39}$$

Above, $\mathrm{Res}[a] \equiv \mathrm{Res}(f, a) = \lim_{x\to a}(z-a)f(z)$ and $\mathrm{Res}^{(2)}[a] \equiv \mathrm{Res}^{(2)}(f, a) = \lim_{x\to a} d/dz[(z-a)^2 f(z)]$ are the residues of the function $f(z)$ at the pole a of the first and second order, respectively. Summing everything, we finally obtain

$$\begin{aligned} L_1(y) = -\pi i \Bigg[& \frac{1}{8i(y-2i)} \log\left(1 + \frac{2}{1+ia}\right) \\ & + \frac{1}{y^2(y^2+4)} \log\left(1 - \frac{iy}{1+ia}\right) + \frac{i}{4y(1+ia)} \Bigg]. \end{aligned} \tag{B.40}$$

The other terms appearing in $L(y)$ can be calculated using a similar approach.

B.2.4 *General expression for the quantum dot susceptibility*

Gathering all terms, the real and imaginary parts of the susceptibility read

$$
\begin{aligned}
&\Pi'_{LL}(\omega) \\
&= -\frac{4\Gamma_L^2}{\pi\Gamma^3 y\left(y^2+4\right)}\left[\arctan\left(a+y\right)-\arctan\left(a-y\right)\right] \\
&+\frac{\Gamma_L}{\pi\Gamma^2\left(y^2+4\right)}\left(1+\frac{4\Gamma_R}{y^2\Gamma}\right)\Big[-2\log\left(1+a^2\right) \\
&+\log\left[1+(a+y)^2\right]+\log\left[1+(a-y)^2\right]\Big],
\end{aligned}
\tag{B.41}
$$

$$
\begin{aligned}
&\Pi''_{LL}(\omega) \\
&= -\frac{2\Gamma_L}{\pi\Gamma^2\left(y^2+4\right)}\left(1+\frac{4\Gamma_R}{y^2\Gamma}\right)\left[\arctan\left(a+y\right)-\arctan\left(a-y\right)\right] \\
&-\frac{2\Gamma_L^2}{\pi\Gamma^3 y\left(y^2+4\right)}\Big[-2\log\left(1+a^2\right) \\
&+\log\left[1+(a+y)^2\right]+\log\left[1+(a-y)^2\right]\Big],
\end{aligned}
\tag{B.42}
$$

$$
\begin{aligned}
&\Pi'_{RR}(\omega) \\
&= -\frac{4\Gamma_R^2}{\pi\Gamma^3 y\left(y^2+4\right)}\left[\arctan\left(b+y\right)-\arctan\left(b-y\right)\right] \\
&+\frac{\Gamma_R}{\pi\Gamma^2\left(y^2+4\right)}\left(1+\frac{4\Gamma_L}{y^2\Gamma}\right)\Big[-2\log\left(1+b^2\right) \\
&+\log\left[1+(b+y)^2\right]+\log\left[1+(b-y)^2\right]\Big],
\end{aligned}
\tag{B.43}
$$

$$
\begin{aligned}
&\Pi''_{RR}(\omega) \\
&= -\frac{2\Gamma_R}{\pi\Gamma^2\left(y^2+4\right)}\left(1+\frac{4\Gamma_L}{y^2\Gamma}\right)\left[\arctan\left(b+y\right)-\arctan\left(b-y\right)\right] \\
&-\frac{2\Gamma_R^2}{\pi\Gamma^3 y\left(y^2+4\right)}\Big[-2\log\left(1+b^2\right) \\
&+\log\left[1+(b+y)^2\right]+\log\left[1+(b-y)^2\right]\Big],
\end{aligned}
\tag{B.44}
$$

$$
\begin{aligned}
&\Pi'_{LR}(\omega)+\Pi'_{RL}(\omega) \\
&= -\frac{4\Gamma_L\Gamma_R}{\pi\Gamma^3 y\left(y^2+4\right)}\left[\arctan\left(a+y\right)-\arctan\left(a-y\right)\right] \\
&-\frac{4\Gamma_L\Gamma_R}{\pi\Gamma^3 y^2\left(y^2+4\right)}\Big[-2\log\left(1+a^2\right) \\
&+\log\left[1+(a+y)^2\right]+\log\left[1+(a-y)^2\right]\Big] \\
&-\frac{4\Gamma_L\Gamma_R}{\pi\Gamma^3 y\left(y^2+4\right)}\left[\arctan\left(b+y\right)-\arctan\left(b-y\right)\right] \\
&-\frac{4\Gamma_L\Gamma_R}{\pi\Gamma^3 y^2\left(y^2+4\right)}\Big[-2\log\left(1+b^2\right) \\
&+\log\left[1+(b+y)^2\right]+\log\left[1+(b-y)^2\right]\Big],
\end{aligned}
\tag{B.45}
$$

$$
\begin{aligned}
&\Pi''_{LR}(\omega) + \Pi''_{RL}(\omega) \\
&= \frac{8\Gamma_L\Gamma_R}{\pi\Gamma^3 y^2\left(y^2+4\right)}\left[\arctan\left(a+y\right) - \arctan\left(a-y\right)\right] \\
&- \frac{2\Gamma_L\Gamma_R}{\pi\Gamma^3 y\left(y^2+4\right)}\Big[-2\log\left(1+a^2\right) \\
&+ \log\left[1+\left(a+y\right)^2\right] + \log\left[1+\left(a-y\right)^2\right]\Big] \\
&+ \frac{8\Gamma_L\Gamma_R}{\pi\Gamma^3 y^2\left(y^2+4\right)}\left[\arctan\left(b+y\right) - \arctan\left(b-y\right)\right] \\
&- \frac{2\Gamma_L\Gamma_R}{\pi\Gamma^3 y\left(y^2+4\right)}\Big[-2\log\left(1+b^2\right) \\
&+ \log\left[1+\left(b+y\right)^2\right] + \log\left[1+\left(b-y\right)^2\right]\Big].
\end{aligned}
\tag{B.46}
$$

Using

$$
\begin{aligned}
\Pi(\omega) = &\left(\beta_L-\lambda\right)^2\Pi_{LL}(\omega) + \left(\beta_R-\lambda\right)^2\Pi_{RR}(\omega) \\
&+ \left(\beta_L-\lambda\right)\left(\beta_R-\lambda\right)\left[\Pi_{LR}(\omega)+\Pi_{RL}(\omega)\right],
\end{aligned}
\tag{B.47}
$$

we obtain the final result for $\Pi(\omega)$:

$$
\begin{aligned}
\Pi'(\omega) = &-\frac{4\Gamma_L}{\pi\Gamma^3 y\left(y^2+4\right)}\left[\arctan\left(a+y\right)-\arctan\left(a-y\right)\right]\\
&\times\left(\left(\beta_L-\lambda\right)^2\Gamma_L+\left(\beta_L-\lambda\right)\left(\beta_R-\lambda\right)\Gamma_R\right)\\
&+\frac{\Gamma_L}{\pi\Gamma^2\left(y^2+4\right)}\Big[-2\log\left(1+a^2\right)\\
&+\log\left[1+\left(a+y\right)^2\right]+\log\left[1+\left(a-y\right)^2\right]\Big]\\
&\times\left(\left(\beta_L-\lambda\right)^2\left(1+\frac{4\Gamma_R}{y^2\Gamma}\right)-\left(\beta_L-\lambda\right)\left(\beta_R-\lambda\right)\frac{4\Gamma_R}{y^2\Gamma}\right)\\
&-\frac{4\Gamma_R}{\pi\Gamma^3 y\left(y^2+4\right)}\left[\arctan\left(b+y\right)-\arctan\left(b-y\right)\right]\\
&\times\left(\left(\beta_L-\lambda\right)^2\Gamma_R+\left(\beta_L-\lambda\right)\left(\beta_R-\lambda\right)\Gamma_L\right)\\
&+\frac{\Gamma_R}{\pi\Gamma^2\left(y^2+4\right)}\Big[-2\log\left(1+b^2\right)\\
&+\log\left[1+\left(b+y\right)^2\right]+\log\left[1+\left(b-y\right)^2\right]\Big]\\
&\times\left(\left(\beta_L-\lambda\right)^2\left(1+\frac{4\Gamma_L}{y^2\Gamma}\right)-\left(\beta_L-\lambda\right)\left(\beta_R-\lambda\right)\frac{4\Gamma_L}{y^2\Gamma}\right).
\end{aligned}
\tag{B.48}
$$

and the imaginary part of the total charge susceptibility reads

$$\begin{aligned}
\Pi''(\omega) = &-\frac{2\Gamma_L}{\pi\Gamma^2\left(y^2+4\right)}\left[\arctan\left(a+y\right)-\arctan\left(a-y\right)\right]\\
&\times\left(\left(\beta_L-\lambda\right)^2\left(1+\frac{4\Gamma_R}{y^2\Gamma}\right)-\left(\beta_L-\lambda\right)\left(\beta_R-\lambda\right)\frac{4\Gamma_R}{y^2\Gamma}\right)\\
&-\frac{2\Gamma_L}{\pi\Gamma^3 y\left(y^2+4\right)}\Big[-2\log\left(1+a^2\right)\\
&+\log\left[1+\left(a+y\right)^2\right]+\log\left[1+\left(a-y\right)^2\right]\Big]\\
&\times\left(\left(\beta_L-\lambda\right)^2\Gamma_L+\left(\beta_L-\lambda\right)\left(\beta_R-\lambda\right)\Gamma_R\right)\\
&-\frac{2\Gamma_R}{\pi\Gamma^2\left(y^2+4\right)}\left[\arctan\left(b+y\right)-\arctan\left(b-y\right)\right]\\
&\times\left(\left(\beta_L-\lambda\right)^2\left(1+\frac{4\Gamma_L}{y^2\Gamma}\right)-\left(\beta_L-\lambda\right)\left(\beta_R-\lambda\right)\frac{4\Gamma_L}{y^2\Gamma}\right)\\
&-\frac{2\Gamma_R}{\pi\Gamma^3 y\left(y^2+4\right)}\Big[-2\log\left(1+b^2\right)\\
&+\log\left[1+\left(b+y\right)^2\right]+\log\left[1+\left(b-y\right)^2\right]\Big]\\
&\left(\left(\beta_L-\lambda\right)^2\Gamma_R+\left(\beta_L-\lambda\right)\left(\beta_R-\lambda\right)\Gamma_L\right).
\end{aligned}\tag{B.49}$$

C

APPENDIX C

C.1 DERIVATION OF THE EFFECTIVE KITAEV HAMILTONIAN IN THE PRESENCE OF THE CAVITY FIELD

In this section, we provide theoretical arguments for the wire Hamiltonian utilized in Eq. (5.4), and the effective electron-cavity Hamiltonian used. In a continuum description, the natural way to account for the interaction between the electrons and the electromagnetic field is via the minimal coupling, i.e. $\mathbf{p} \to \mathbf{p} - (e/c)\mathbf{A}$ in the electronic Hamiltonian, with $\mathbf{A}$ being the electromagnetic field vector potential and $\mathbf{p}$ being the momentum of the electrons in the material. In a tight-binding picture instead, one accounts for the coupling between light and matter by performing the Peierls substitution to the hopping parameters t_{ii+1} between neighboring sites i and $i+1$, namely

$$t_{ii+1} \to t_{ii+1} e^{i \int_i^{i+1} \mathbf{A}(\mathbf{r}) \cdot d\mathbf{r}}, \tag{C.1}$$

with $\mathbf{A}(\mathbf{r})$ being the electromagnetic field vector potential at position $\mathbf{r}$, and the integration is performed between the sites i and $i+1$. We will focus on the derivation of the effective Kitaev model in the tight-binding picture, as the microscopic, continuum model was described in great detail very recently in [23]. We thus refer the reader to that paper for a detailed calculation of the cavity effects, as well as the derivation of the capacitive coupling starting from the minimal coupling.

Here we give some details on the derivation of Eq. (5.4) starting from a non-superconducting nanowire coupled to a bulk p-wave superconductor with such a coupling being assisted by the cavity field. For simplicity, we assume the bulk to be not s, but p-wave paired, thus the presence of spin-orbit coupling in the wire is not a necessary ingredient. However, the

present calculations can be straightforwardly generalized to more realistic system, such as nanowires with SOI. The total Hamiltonian of the system reads:

$$H_{sys} = H_b + H_w + H_T + H_c \,, \tag{C.2}$$

where

$$\begin{aligned} H_p = -\mu_p \sum_j c^\dagger_{j,p} c_{j,p} + \sum_j \Big(& t_p c^\dagger_{j,p} c_{j+1,p} \\ & + \Delta_p c^\dagger_{j,p} c^\dagger_{j+1,p} + \text{h.c.} \Big) \end{aligned} \tag{C.3}$$

with $p = b(bulk), w(wire)$, and $\Delta_w = 0$ (no intrinsic superconductivity in the wire), and $\Delta_b \equiv \Delta$ the p-wave pairing in the bulk superconductor. Here, $c_{j,p}$ ($c^\dagger_{j,p}$) and t_p are the electronic annihilation (creation) operator at position j and the hopping parameter in system $p = b, w$, respectively. The tunneling Hamiltonian in the presence of the cavity reads:

$$H_T = \sum_j \left(t_{int} e^{-i\hat{\phi}_j} c^\dagger_{j,w} c_{j,b} + \text{h.c.} \right), \tag{C.4}$$

where $\hat{\phi}_j = \hat{A}_j d_j$, with $\hat{A}_j = i(\alpha_j/\omega_c)(a^\dagger - a)$, d_j, α_j, ω_c, and a ($a^\dagger$), being the cavity vector potential, the coupling strength, the cavity frequency, and the cavity photon annihilation (creation) operators, respectively. Note that we assumed that the cavity field points perpendicularly to the wire, and it has no component along it. If instead such components would exists, we should have modified the wire Hamiltonian too in order to account for the cavity induced phase factors. In the following, we will assume that $\alpha_j d_j \equiv \alpha_j = \alpha$, namely it is constant along the entire wire. Finally, the Hamiltonian of the cavity reads:

$$H_c = \omega_c a^\dagger a \,, \tag{C.5}$$

with ω_c being the (fundamental) frequency of the cavity. Before deriving an effective wire Hamiltonian, it is instructive to switch to the Fourier space, for both the bulk and wire Hamiltonians. We get:

$$H_b = \sum_k \xi_{k,b} c^\dagger_{k,b} c_{k,b} - \sum_{k>0} i\Delta \sin k \left(c_{-k,b} c_{k,b} - c^\dagger_{k,b} c^\dagger_{-k,b} \right) , \tag{C.6}$$

$$H_w = \sum_k \xi_{k,w} c^\dagger_{k,w} c_{k,w} , \tag{C.7}$$

$$H_T = t_{int} \sum_k \left(e^{i\hat{\phi}} c^\dagger_{k,w} c_{k,b} + e^{-i\hat{\phi}} c^\dagger_{k,b} c_{k,w} \right) , \tag{C.8}$$

where $\xi_{k,p} = t_p \cos k - \mu_p$, with μ_α the chemical potential in the $p = w, b$ system.

Next we perform the so called Lang-Firsov transformation on the system Hamiltonian, which means $\widetilde{H}_{sys} = \exp(S) H_{sys} \exp(-S)$ with S chosen as follows:

$$S = \frac{\alpha}{\omega_c} (a - a^\dagger) \sum_q c^\dagger_{q,w} c_{q,w} . \tag{C.9}$$

After some lengthy, but straightforward calculation we obtain the system Hamiltonian as follows:

$$\begin{aligned} \widetilde{H}_{sys} = H_w + H_b + \underbrace{\alpha \sum_q c^\dagger_{q,w} c_{q,w} (a + a^\dagger)}_{H_{c-w}} \\ + \frac{\alpha^2}{\omega_c} \underbrace{\left(\sum_q c^\dagger_{q,w} c_{q,w} \right)^2}_{\hat{N}^2} + \underbrace{t_{int} \sum_k (c^\dagger_{q,w} c_{k,b} + \text{h.c.})}_{H_T} + H_c , \end{aligned} \tag{C.10}$$

which implies we excluded the photonic field from the tunneling term at the expense of adding photon-dependent chemical potential shift in the wire (third term) as well as an interaction term (fourth term). Note that for $t_{int} = 0$, the transformation does not affect the spectrum, as it can be simply undone. However, as will see in the following, in the

presence of the tunneling term the photonic field in the form of the capacitive coupling can lead to real effects.

In the following, we aim at finding an effective Hamiltonian describing the wire only by integrating the bulk superconductor degrees of freedom up to second order in the tunneling t_{int}. We choose to do so by employing the Schrieffer-Wolff transformation formalism, which means, as before, that we unitary rotate the system Hamiltonian as

$$\begin{aligned} H_{sys}^{eff} &= e^{S_{SW}} \widetilde{H}_{sys} e^{-S_{SW}} = H_w + H_b + H_{w-c} + H_T + H_c \\ &\quad + [S_{SW}, H_w + H_b + H_{w-c} + H_T + H_c] + \dots , \end{aligned} \tag{C.11}$$

and choose

$$[S_{SW}, H_w + H_b] = -H_T , \tag{C.12}$$

or $S_{SW} = (\mathcal{L}_w + \mathcal{L}_b)^{-1} H_T$, with $\mathcal{L}_\alpha$ being a superoperator whose action is defined as $\mathcal{L}_\alpha A = [H_\alpha, A]$, $\forall A$. This is equivalent to the following identity:

$$S_{SW} = i \lim_{\eta \to 0} \int_0^{+\infty} dt e^{-\eta t} e^{i(H_w + H_b)t} H_T e^{-i(H_w + H_b)t}. \tag{C.13}$$

This term excludes the tunneling Hamiltonian H_T in leading order (assuming there is no diagonal contribution caused by such a term). Then, we neglect the contributions of the higher order terms on the wire spectrum by averaging over the bulk ground state $|0_b\rangle$ in order to derive a purely (renormalized) wire Hamiltonian:

$$\begin{aligned} H_w^{eff} &\approx \langle 0_b | H_b + H_w + H_c + H_{w-c} + \frac{1}{2} [S_{SW}, H_T] \\ &\quad + [S_{SW}, H_{w-c}] + \dots | 0_b \rangle , \end{aligned} \tag{C.14}$$

In order to find S_{SW} from Eq. (C.13) explicitly, let us perform Bogoliubov transformation for the bulk p-wave superconductor defined as

$$c_{k,b} = u_k^* \gamma_{k,b} + v_k \gamma_{-k,b}^\dagger \,, \tag{C.15}$$

$$c_{-k,b}^\dagger = -v_k^* \gamma_{k,b} + u_k \gamma_{-k,b}^\dagger \,, \tag{C.16}$$

where $k > 0$ and

$$\begin{aligned} u_k &= \sqrt{1/2\,(1 + \xi_k/E_{kb})} \\ v_k &= \sqrt{1/2\,(1 - \xi_k/E_{kb})} e^{-i\phi_b} \end{aligned} \tag{C.17}$$

with ϕ_b the phase of the superconducting condensate (that we choose $= 0$ from now on) and $E_{kb} = \sqrt{\xi_k^2 + \Delta^2 \sin^2 k}$ the spectrum. We can then express the bulk Hamiltonian in terms of the γ_k and γ_{-k} operators:

$$H_b = \sum_{k>0} E_{kb} \left(\gamma_{k,b}^\dagger \gamma_{k,b} + \gamma_{-k,b}^\dagger \gamma_{-k,b} \right) . \tag{C.18}$$

Utilizing the fact that:

$$c_{k,w}(t) = c_{k,w}(0) \exp(-i\xi_{k,w} t) \,, \tag{C.19}$$

and

$$\gamma_{k,b}(t) = \gamma_{k,b}(0) \exp(-iE_{k,b} t) \,, \tag{C.20}$$

we can readily find the transformation matrix S_{SW} as follows (assuming also that $\xi_{k,w} \ll E_{k,b}$, since we are interested in the energies well inside the band gap of the bulk superconductor):

$$\begin{aligned} S_{SW} = \sum_k \frac{t_{int}}{E_{kb}} \Big[& \left(|u_k|^2 - |v_k|^2 \right) \left(c_{k,w}^\dagger c_{k,b} - c_{k,b}^\dagger c_{k,w} \right) \\ & - 2 u_k v_k (c_{k,w}^\dagger c_{-k,b}^\dagger - c_{-k,b} c_{k,w}) \Big] . \end{aligned} \tag{C.21}$$

Utilizing this expression for S_{SW}, we can calculate the expectation values for the different commutators in Eq. (C.14). We obtain:

$$H_{ind,w} \equiv \frac{1}{2}\langle 0_b| \left[S_{SW}, H_T + 2H_{c-w}\right] |0_b\rangle \approx -\sum_k \frac{t_{int}^2}{E_{kb}} \times \left[\left(|u_k|^2 - |v_k|^2\right) c_{k,w}^\dagger c_{k,w} - 2u_k v_k c_{-k,w}^\dagger c_{k,w}^\dagger + \text{h.c.}\right], \tag{C.22}$$

which can be interpreted as follows: the first term renormalizes the single particle spectrum in the wire, while the second term is responsible for the induced superconductivity in the wire. The full wire Hamiltonian thus becomes:

$$\begin{aligned} H_w^{\text{eff}} = &\sum_k (\underbrace{\xi_{k,w} + \delta\xi_{k,w}}_{\xi_{k,w}^{\text{eff}}}) c_{k,w}^\dagger c_{k,w} \\ &+ 2\sum_k \left(\Delta_{ind} c_{k,w}^\dagger c_{-k,w}^\dagger + \text{h.c}\right) \\ &+ \alpha \sum_k c_{k,w}^\dagger c_{k,w} \left(a + a^\dagger\right) + \frac{\alpha^2}{\omega_c} \hat{N}_w^2 \end{aligned} \tag{C.23}$$

with

$$\delta\xi_{k,w} = \frac{t_{int}^2}{E_{kb}} \left(|u_k|^2 - |v_k|^2\right) = \frac{t_{int}^2 \xi_{k,b}}{E_{kb}^2}, \tag{C.24}$$

$$\Delta_{ind} = \frac{t_{int}^2}{E_{kb}} u_k v_k = \frac{t_{int}^2}{2E_{kb}^2} \Delta \sin k \tag{C.25}$$

being the renormalization of the single-particle energies and the p-wave induced gap ($\propto \sin k$). Note that the last term in Eq. (C.23) can be seen as a normalization of the single-particle spectrum in the mean-field, and thus finally we recover the same wire Hamiltonian defined in Eq. (5.4).

C.2 THE SUSCEPTIBILITY FOR THE KITAEV MODEL IN CASE OF PERIODIC BOUNDARY CONDITIONS

In this section, we give more details on the derivation of the susceptibility $\Pi(\omega)$ for the case of a ring geometry for which we can apply PBCs. The Kitaev chain Hamiltonian in real space was defined in Eq.(5.4) as:

$$H_{tot} = H_{el} + H_{el-c} + H_{ph}\,, \tag{C.26}$$

$$H_{el} = -\mu \sum_{i=1}^{N} c_i^\dagger c_i - \frac{1}{2}\sum_{i=1}^{N-1}(t c_i^\dagger c_{i+1} + \Delta c_i c_{i+1} + \text{h.c.})\,,$$

$$H_{int} = \alpha \sum_{i=1}^{N} c_i^\dagger c_i (a + a^\dagger)\,, \tag{C.27}$$

and $H_{ph} = \omega_c a^\dagger a$. In this case, we can switch to the Fourier space, which implies we can write the fermionic operators as follows:

$$c_j = \frac{1}{\sqrt{N}} \sum_k c_k e^{ikj}\,. \tag{C.28}$$

where c_k is the fermionic annihilation operator with momentum $k = 2\pi n/N$. We can then rewrite the electronic Hamiltonian in momentum space

$$H_{el} = \sum_{k>0} H_{BdG}^K(k)\,, \tag{C.29}$$

with

$$H_{BdG}^k(k) = \xi_k(c_k^\dagger c_k - c_{-k}c_{-k}^\dagger) - i\Delta \sin k (c_{-k}c_k - c_k^\dagger c_{-k}^\dagger), \tag{C.30}$$

is the Bogoliubov de Gennes Hamiltonian and $\xi_k = -t\cos k - \mu$. The interaction Hamiltonian between the electronic system and the cavity can as well be written in the k-space as

$$H_{el-c} = \sum_{k>0} \alpha(c_k^\dagger c_k - c_{-k} c_{-k}^\dagger)(a + a^\dagger). \tag{C.31}$$

One can simply diagonalize the H_{el} in the k-space and write:

$$H_{el} = \sum_{k>0} E_k \left(\gamma_k^\dagger \gamma_k + \gamma_{-k}^\dagger \gamma_{-k}\right), \tag{C.32}$$

with

$$E_k = \pm\sqrt{(-t\cos k - \mu)^2 + (\Delta \sin k)^2}\,, \tag{C.33}$$

being the eigenenergies, and we used

$$c_k = u_k^* \gamma_k + v_k \gamma_{-k}^\dagger, \tag{C.34}$$

$$c_{-k}^\dagger = -v_k^* \gamma_k + u_k \gamma_{-k}^\dagger\,. \tag{C.35}$$

Here, the functions u_k and v_k are given by

$$|u_k|^2 = \frac{1}{2}\left(1 + \frac{\xi_k}{E_k}\right), \tag{C.36}$$

$$|v_k|^2 = \frac{1}{2}\left(1 - \frac{\xi_k}{E_k}\right). \tag{C.37}$$

We can now calculate the susceptibility $\Pi(\omega)$ defined in the previous section, which quantifies the change in the photonic transmission τ due to the interaction with the electronic system. In the Fourier space, we obtain:

$$\Pi(t) = -i\theta(t)\alpha^2 \sum_{k,q>0} \langle \Big[\left(c_k^\dagger c_k - c_{-k} c_{-k}^\dagger \right)(t), \left(c_q^\dagger c_q - c_{-q} c_{-q}^\dagger \right)(0) \Big] \rangle. \tag{C.38}$$

Using Eq. (C.34) and Eq. (C.35) with Eq. (C.36) and Eq. (C.37) we find:

$$\Pi(\omega) = \alpha^2 \sum_{k>0} \frac{(\Delta \sin k)^2}{E_k^2} \left(\frac{1}{\omega - 2E_k + i\eta} - \frac{1}{\omega + 2E_k + i\eta} \right), \tag{C.39}$$

with the small $\eta > 0$ assuring the convergence of the time-integrals. For large $N \gg 1$, we can transform the sum into integral, and also write $\Pi(\omega) = \Pi'(\omega) + i\Pi''(\omega)$, with:

$$\Pi'(\omega) = \frac{2N\alpha^2}{\pi} \mathcal{P} \int_0^\pi dk \frac{(\Delta \sin k)^2}{E_k} \frac{1}{\omega^2 - 4E_k^2}, \tag{C.40}$$

$$\Pi''(\omega) = \frac{N\alpha^2}{2} \int_0^\pi dk \frac{(\Delta \sin k)^2}{E_k^2} \left[\delta(\omega - 2E_k) - \delta(\omega + 2E_k) \right], \tag{C.41}$$

where $\mathcal{P}\ldots$ means the principal value of the function and we used the fact that:

$$\frac{1}{x - a + i\epsilon} = \mathcal{P} \frac{1}{x - a} - i\pi\delta(x - a). \tag{C.42}$$

We can perform the integral over k for the imaginary part $\Pi''(\omega)$ to obtain the expression Eq.(5.9):

$$\Pi''(\omega) = \frac{\alpha^2 t N}{2\mu\omega} \sqrt{1 - \frac{\left[(\omega/2)^2 - t^2 - \mu^2 \right]^2}{4t^2\mu^2}}, \tag{C.43}$$

for $|t + \mu| < \omega/2 < |t - \mu|$, and being zero otherwise. For the real part $\Pi'(\omega)$ we found no simple solution, and so we chose not to depict it. Note that the susceptibility $\Pi(\omega) \propto N$, i. e. it scales linearly with the number of sites.

C.3 THE SUSCEPTIBILITY OF THE NANOWIRE IN CASE OF PERIODIC BOUNDARY CONDITIONS

The Hamiltonian for a nanowire in the presence of a Zeeman field B, Rashba spin-orbit coupling u and induced superconductivity Δ reads [73]

$$H_{NW} = \left(\frac{p^2}{2m} - \mu\right)\tau_z + up\sigma_z\tau_z + B\sigma_x + \Delta\tau_x. \tag{C.44}$$

Let us diagonalize the Hamiltonian $H_{NW} = H_0 + \Delta\tau_x$ in the absence of the induced pairing Δ and then treat the latter perturbatively

$$H_0 = \left(\frac{p^2}{2m} - \mu\right)\tau_z + up\sigma_z\tau_z + B\sigma_x. \tag{C.45}$$

In order to do so, let us perform the unitary transformation [73]

$$\tilde{H}_0 = UH_0U^\dagger, \tag{C.46}$$

where

$$U = \exp\left(i\alpha\sigma_y\tau_z/2\right) = \cos\left(\alpha/2\right) + i\sigma_y\tau_z\sin\left(\alpha/2\right). \tag{C.47}$$

If we choose α so that

$$\tan\left(\alpha\right) = \frac{B}{up}, \tag{C.48}$$

$\tilde{H}_0$ takes the from

$$\tilde{H}_0 = \left[\frac{p^2}{2m} - \mu + \sqrt{u^2p^2 + B^2}\sigma_z\right]\tau_z. \tag{C.49}$$

Now let us reintroduce the pairing term $\Delta\tau_x$ and apply the transformation U to it. Then $\tilde{H}_{NW}$ reads

$$\tilde{H}_{NW} = \Big[\frac{p^2}{2m} - \mu + \sqrt{u^2p^2 + B^2}\sigma_z\Big]\tau_z + \frac{\Delta up}{\sqrt{u^2p^2 + B^2}}\tau_x - \frac{\Delta B}{\sqrt{u^2p^2 + B^2}}\sigma_y\tau_y. \tag{C.50}$$

Neglecting the last term in Eq.(C.50) the effective Hamiltonian reads

$$\tilde{H}_{eff} = \Big[\frac{p^2}{2m} - \mu + \sqrt{u^2p^2 + B^2}\sigma_z\Big]\tau_z + \frac{\Delta up}{\sqrt{u^2p^2 + B^2}}\tau_x. \tag{C.51}$$

The bulk energy spectrum of $\tilde{H}_{eff}$ for $\sigma_z = -1$ is

$$\epsilon_{p,-1} = \pm\sqrt{\left(\frac{p^2}{2m} - \mu - \sqrt{u^2p^2 + B^2}\right)^2 + \frac{\Delta^2u^2p^2}{u^2p^2 + B^2}} \tag{C.52}$$

and for $\sigma_z = +1$ is

$$\epsilon_{p,+1} = \pm\sqrt{\left(\frac{p^2}{2m} - \mu + \sqrt{u^2p^2 + B^2}\right)^2 + \frac{\Delta^2u^2p^2}{u^2p^2 + B^2}}. \tag{C.53}$$

The electronic susceptibility is defined as

$$\Pi(t) = -i\theta(t)\langle[\tau_z(t), \tau_z(0)]\rangle. \tag{C.54}$$

In order to diagonalize the Hamiltonian in Eq. (C.51), let us perform a transformation

$$H_d = U_1\tilde{H}_{eff}U_1^\dagger = \epsilon_p\tau_z, \tag{C.55}$$

where

$$U_1 = \exp(i\gamma\tau_y/2) = \cos(\gamma/2) + i\tau_y \sin(\gamma/2). \tag{C.56}$$

Then the electronic susceptibility reads

$$\begin{aligned}\Pi(t) = -i\theta(t)\langle\Big[&\cos(\gamma)\tau_z(0) - \sin(\gamma)\tau_x(t),\\ &\cos(\gamma)\tau_z(0) - \sin(\gamma)\tau_x(0)\Big]\rangle.\end{aligned} \tag{C.57}$$

$$\begin{aligned}\tau_x(t) &= e^{i\epsilon_p\tau_z t}\tau_x(0)e^{-i\epsilon_p\tau_z t}\\ &= \cos(2\epsilon_p t)\,\tau_x(0) - \sin(2\epsilon_p t)\,\tau_y(0).\end{aligned} \tag{C.58}$$

Introducing Eq.(C.58) into Eq.(C.57), $\Pi(t)$ reads

$$\Pi(t) = -2\theta(t)\sin^2(\gamma)\sin(2\epsilon_p t). \tag{C.59}$$

Performing the Fourier transform, Eq. (C.59) reads

$$\begin{aligned}\Pi(\omega) &= -2\sum_p \sin^2(\gamma)\int_0^{+\infty} dt e^{i\omega t - \eta t}\sin(2\epsilon_p t)\\ &= -2\sum_p \sin^2(\gamma)\frac{2\epsilon_p}{4\epsilon_p^2 + (\eta - i\omega)^2}\\ &= \sum_p \sin^2(\gamma)\left(\frac{1}{\omega - 2\epsilon_p + i\eta} - \frac{1}{\omega + 2\epsilon_p + i\eta}\right).\end{aligned} \tag{C.60}$$

Sum can be transformed into integral as

$$\sum_p = \frac{N}{2\pi}\int dp = \frac{N}{2\pi}\int d\epsilon\rho(\epsilon). \tag{C.61}$$

Then the imaginary part of the susceptibility $\Pi(\omega) = \Pi'(\omega) + i\Pi''(\omega)$, Eq. (C.60) reads

$$\Pi''(\omega) = -\frac{N}{4}\int d\epsilon \rho(\epsilon)\sin^2(\gamma)(\epsilon)\left[\delta(\epsilon - \omega/2) - \delta(\epsilon + \omega/2)\right]. \tag{C.62}$$

The projection onto the lower band $\sigma_z = -1$

The low-energy subspace at $p = \pm p_F$ is formed by the bands for which $\sigma_z = -1$. $p_F = 2mu$ when $\mu = 0$.

The effective Hamiltonian for $\epsilon_{SO} = mu^2 >> B$, $\mu = 0$ linearized around $\pm p_F$ reads

$$\tilde{H}_{eff} = u(|p| - p_F)\tau_z + sign(p)\Delta\tau_x. \tag{C.63}$$

The bulk energy spectrum reads

$$\epsilon_p = \pm\sqrt{\Delta^2 + u^2(|p| - p_F)^2}. \tag{C.64}$$

In this limit

$$\sin^2(\gamma)(\epsilon) = \frac{\Delta^2}{\epsilon^2} \tag{C.65}$$

and the density of states reads

$$\rho(\epsilon) = \frac{\epsilon}{u\sqrt{\epsilon^2 - \Delta^2}sign(p)}. \tag{C.66}$$

Introducing Eq.(C.65) and Eq.(C.66) into Eq.(C.62) the imaginary part of the electronic susceptibility reads

$$\Pi''(\omega) = -\frac{N\Delta^2}{\omega u\sqrt{\omega^2 - 4\Delta^2}}. \tag{C.67}$$

The projection onto $\sigma_z = +1$

In this case the effective Hamiltonian linearized around $p = 0$ reads

$$\tilde{H}_{eff} = \left(\frac{p^2}{2m^*} - \mu + B \right) \tau_z + \frac{\Delta u p}{B} \tau_x, \tag{C.68}$$

where an effective mass m^* was introduced as

$$\frac{1}{m^*} = \frac{1}{m} + \frac{u^2}{B}. \tag{C.69}$$

The bulk energy spectrum reads

$$\begin{aligned} \epsilon_p &= \pm \sqrt{\left(B - \mu + \frac{p^2}{2m^*} \right)^2 + \frac{\Delta^2 u^2 p^2}{B^2}} \\ &\approx \pm \sqrt{(B-\mu)^2 + cp^2}, \end{aligned} \tag{C.70}$$

where

$$c = \frac{B-\mu}{m^*} + \frac{\Delta^2 u^2}{B^2}. \tag{C.71}$$

The density of state reads

$$\rho(\epsilon) = \frac{\epsilon}{\sqrt{c\left[\epsilon^2 - (B-\mu)^2\right]}}. \tag{C.72}$$

And

$$\sin(\gamma)^2(\epsilon) = \frac{\Delta^2 u^2 \left[\epsilon^2 - (B-\mu)^2\right]}{B^2 \epsilon^2 c}. \tag{C.73}$$

Introducing Eq.(C.72) and Eq.(C.73) into Eq.(C.62) the imaginary part of the electronic susceptibility reads

$$\Pi''(\omega) = -\frac{N\Delta^2 u^2\sqrt{\omega^2 - 4(B-\mu)^2}}{4\omega B^2 c^{3/2}}. \tag{C.74}$$

C.4 THE CORRELATION FUNCTION FOR OPEN BOUNDARY CONDITIONS

In this part, we present details on the calculation of the susceptibility for a finite wire with open boundary conditions. In this case, the excitation spectrum changes compared to the previous case, as in the topological region the zero energy Majorana fermions emerge. The susceptibility reads:

$$\Pi(\omega) = -i\alpha^2 \sum_{i,j=1}^{N} \int_0^\infty dt e^{-i\omega t} \langle |[\hat{n}_i(t), \hat{n}_j(0)]| \rangle \tag{C.75}$$

and which can be written as

$$\Pi(\omega) = \Pi_{BB}(\omega) + \Pi_{BM}(\omega), \tag{C.76}$$

being the sum of a bulk susceptibility, that can be constructed from only the bulk (or gaped) states, and cross terms that involve both bulk and Majorana states, respectively. We use the discrete lattice model to numerically diagonalize the Hamiltonian for an electronic system with N fermionic sites. This can be written in a compact form as follows:

$$H_{el} = \frac{1}{2}\vec{c}^\dagger M \vec{c} \tag{C.77}$$

with

$$\vec{c} = (c_1, c_1^\dagger, c_2, c_2^\dagger, ..., c_N, c_N^\dagger)^T, \tag{C.78}$$

where M is a $2N \times 2N$ matrix. Moreover, assuming all entries in the matrix are real, M is also symmetric, we can write it as follows:

$$M = PWP^{\dagger}, \tag{C.79}$$

where W is a diagonal matrix with eigenvalues on its diagonal and P is a unitary matrix ($PP^{\dagger} = P^{\dagger}P = I$) whose columns are eigenvectors of M. The matrix W is ordered so that

$$W = \begin{pmatrix} \epsilon_1 & 0 & \cdots & 0 & 0 \\ 0 & -\epsilon_1 & \cdots & 0 & 0 \\ \vdots & \vdots & \ddots & \vdots & \vdots \\ 0 & 0 & \cdots & \epsilon_N & 0 \\ 0 & 0 & \cdots & 0 & -\epsilon_N \end{pmatrix}, \tag{C.80}$$

with $\pm\epsilon_n$ being the eigenenergies of the BdG Hamiltonian and $n = 1, \ldots N$. That pertains to the following diagonal Hamiltonian:

$$H_{1D} = \sum_{m=1}^{N} \epsilon_m \left(\tilde{c}_m^{\dagger} \tilde{c}_m - \frac{1}{2} \right), \tag{C.81}$$

where $\tilde{c}_m$ ($\tilde{c}_m^{\dagger}$) are the annihilation (creation) operators for the Bogoliubov quasiparticles, which are defined as follows:

$$\vec{\tilde{c}} = P^{\dagger}\vec{c} \tag{C.82}$$

and

$$\vec{\tilde{c}} = (\tilde{c}_1, \tilde{c}_1^{\dagger}, \tilde{c}_2, \tilde{c}_2^{\dagger}, \ldots, \tilde{c}_N, \tilde{c}_N^{\dagger})^{T}. \tag{C.83}$$

It is instructive to introduce the wavefunctions $\vec{\psi}_k(i) = (u_{k,i}, v_{k,i})^{T}$, where $u_{k,i}$ ($v_{k,i}$) = $p_{2i-1,k}$ ($p_{2i,k}$), and which are describing the state $k = 0, \ldots, 2N$ at position $i = 1, \ldots, N$

in the lattice and accounts for the electron (u) and hole (v) components, respectively. That allows us to write:

$$c_i = \sum_{k=1}^{N} \left[u_{2k-1,i} \tilde{c}_k + u_{2k,i} \tilde{c}_k^\dagger \right], \tag{C.84}$$

$$c_i^\dagger = \sum_{k=1}^{N} \left[v_{2k-1,i} \tilde{c}_k + v_{2k,i} \tilde{c}_k^\dagger \right]. \tag{C.85}$$

so that we can rewrite Eq. (C.75) in terms of $u_{k,i}$ and $v_{k,i}$ as follows:

$$\begin{aligned}
\Pi(\omega) = & \sum_{i,j,k,m=1}^{N} (1-n_k)(1-n_m) v_{2k-1,i} u_{2m-1,i} \\
& \times \left(u_{2k,j} v_{2m,j} - v_{2k,j} u_{2m,j} \right) \\
& \times \left(\frac{1}{\omega + i\eta - \epsilon_{2k-1} - \epsilon_{2m-1}} - \frac{1}{\omega + i\eta + \epsilon_{2k-1} + \epsilon_{2m-1}} \right) \\
& + (1-n_k) n_m v_{2k-1,i} u_{2m,i} \left(u_{2k,j} v_{2m-1,j} - v_{2k,j} u_{2m-1,j} \right) \\
& \times \left(\frac{1}{\omega + i\eta - \epsilon_{2k-1} + \epsilon_{2m-1}} - \frac{1}{\omega + i\eta + \epsilon_{2k-1} - \epsilon_{2m-1}} \right) \\
& + n_k (1-n_m) v_{2k,i} u_{2m-1,i} \left(u_{2k-1,j} v_{2m,j} - v_{2k-1,j} u_{2m,j} \right) \\
& \times \left(\frac{1}{\omega + i\eta + \epsilon_{2k-1} - \epsilon_{2m-1}} - \frac{1}{\omega + i\eta - \epsilon_{2k-1} + \epsilon_{2m-1}} \right) \\
& + n_k n_m v_{2k,i} u_{2m,i} \left(u_{2k-1,j} v_{2m-1,j} - v_{2k-1,j} u_{2m-1,j} \right) \\
& \times \left(\frac{1}{\omega + i\eta + \epsilon_{2k-1} + \epsilon_{2m-1}} - \frac{1}{\omega + i\eta - \epsilon_{2k-1} - \epsilon_{2m-1}} \right).
\end{aligned} \tag{C.86}$$

Next we extract from this expression only the $\Pi_{BM}(\omega)$ component. This reads:

$$\begin{aligned}
\Pi_{BM}(\omega) = &\sum_{i,j=1}^{N}\sum_{k=1}^{N-1}\left(\frac{1}{\omega+i\eta+\epsilon_{2k-1}}+\frac{1}{-\omega-i\eta+\epsilon_{2k-1}}\right)\\
&\times\Bigg[-(1-n_k-n_M)\Big[v_{2k-1,i}u_{2M-1,i}u_{2k,j}v_{2M,j}\\
&-v_{2k-1,i}u_{2M-1,i}v_{2k,j}u_{2M,j}+v_{2M-1,i}u_{2k-1,i}u_{2M,j}v_{2k,j}\\
&-v_{2M-1,i}u_{2k-1,i}v_{2M,j}u_{2k,j}\Big]\\
&-(n_M-n_k)\Big[v_{2k-1,i}u_{2M,i}u_{2k,j}v_{2M-1,j}\\
&-v_{2k-1,i}u_{2M,i}v_{2k,j}u_{2M-1,j}+v_{2M,i}u_{2k-1,i}u_{2M-1,j}v_{2k,j}\\
&-v_{2M,i}u_{2k-1,i}v_{2M-1,j}u_{2k,j}\Big]\Bigg],
\end{aligned}\tag{C.87}$$

and, using that $u_{2k-1,i}=v_{2k,i}$, it can be simplified even further to give:

$$\begin{aligned}
\Pi_{BM}(\omega) = &\sum_{i,j=1}^{N}\sum_{k=1}^{N-1}\left(\frac{1}{\omega+i\eta+\epsilon_{2k-1}}+\frac{1}{-\omega-i\eta+\epsilon_{2k-1}}\right)\\
&\times\Bigg[-(n_M-1+n_k)\Big[-u_{2k,i}v_{2M,i}u_{2k,j}v_{2M,j}\\
&+u_{2k,i}v_{2M,i}v_{2k,j}u_{2M,j}-u_{2M,i}v_{2k,i}u_{2M,j}v_{2k,j}\\
&+u_{2M,i}v_{2k,i}v_{2M,j}u_{2k,j}\Big]\\
&+(n_M-n_k)\Big[-u_{2k,i}u_{2M,i}u_{2k,j}u_{2M,j}\\
&+u_{2k,i}u_{2M,i}v_{2k,j}v_{2M,j}-v_{2M,i}v_{2k,i}v_{2M,j}v_{2k,j}\\
&+v_{2M,i}v_{2k,i}u_{2M,j}u_{2k,j}\Big]\Bigg].
\end{aligned}\tag{C.88}$$

Let us now introduce the coefficients $C^{(s)}$, $s = 1, 2$ defined in Eq.(5.24):

$$C^{(s)} = \sum_{i=1}^{N} (u_{2M,i}\delta_{s,1} + v_{2M,i}\delta_{s,2})u_{2k,i} - (u_{2M,i}\delta_{s,2} + v_{2M,i}\delta_{s,1})v_{2k,i}\,, \tag{C.89}$$

which we can utilize to rewrite $\Pi_{BM}(\omega)$ as follows:

$$\Pi_{BM}(\omega) = \sum_{k=1}^{N-1} \left(\frac{1}{\epsilon_{2k} + \omega + i\eta} + \frac{1}{\epsilon_{2k} - \omega - i\eta} \right) \times \left[(n_M - n_k) \left| C^{(1)} \right|^2 - (n_M - 1 + n_k) \left| C^{(2)} \right|^2 \right], \tag{C.90}$$

and which correspond to the expression Eq. (5.23).

D

APPENDIX D

In this appendix, we will derive the electronic susceptibility for the chain that can host multiple Majorana fermions in case of periodic boundary conditions, $c_{N+1} \equiv c_1$.

$$c_j = \frac{1}{\sqrt{N}} \sum_k c_k e^{ikj}, \tag{D.1}$$

$$c_j^\dagger = \frac{1}{\sqrt{N}} \sum_k c_k^\dagger e^{-ikj}. \tag{D.2}$$

Then Eq.(6.1) in the k-space reads

$$H = \sum_{k>0} H_k(k), \tag{D.3}$$

where

$$H_k(k) = \begin{pmatrix} c_k^\dagger & c_{-k} \end{pmatrix} \begin{pmatrix} -2\mu - 2t_1\cos(k) - 2t_2\cos(2k) & 2i\Delta_1\sin(k) + 2i\Delta_2\sin(2k) \\ -2i\Delta_1\sin(k) - 2i\Delta_2\sin(2k) & 2\mu + 2t_1\cos(k) + 2t_2\cos(2k) \end{pmatrix} \begin{pmatrix} c_k \\ c_{-k}^\dagger \end{pmatrix} \tag{D.4}$$

$$\tau_x = c_{-k}c_k + c_k^\dagger c_{-k}^\dagger, \tag{D.5}$$

$$\tau_y = -i(c_k^\dagger c_{-k}^\dagger + c_k c_{-k}), \tag{D.6}$$

$$\tau_z = c_k^\dagger c_k - c_{-k} c_{-k}^\dagger. \tag{D.7}$$

$$H_k(k) = [-2\mu - 2t_1 \cos(k) - 2t_2 \cos(2k)]\tau_z + [-2\Delta_1 \sin(k) - 2\Delta_2 \sin(2k)]\tau_y. \tag{D.8}$$

Let us diagonalize the Hamiltonian $H_k(k)$ by performing a unitary transformation

$$\tilde{H}_k(k) = U^\dagger H_k(k) U = E_k \tau_z \tag{D.9}$$

with

$$U = \exp(-i\theta_k \tau_x/2) = \cos(\theta_k/2) - i\tau_x \sin(\theta_k/2). \tag{D.10}$$

$$\tan(\theta_k) = -\frac{\Delta_1 \sin(k) + \Delta_2 \sin(2k)}{\mu + t_1 \cos(k) + t_2 \cos(2k)}. \tag{D.11}$$

The winding number that measures the number of Majorana fermions reads

$$w = \int_0^{2\pi} \frac{d\theta_k}{2\pi}. \tag{D.12}$$

Energy is

$$E_{k,\pm} = \pm 2\sqrt{(\mu + t_1\cos(k) + t_2\cos(2k))^2 + (\Delta_1\sin(k) + \Delta_2\sin(2k))^2}. \tag{D.13}$$

The condition for the topological phase transition is closing of the gap, $E_k = 0$.

$$E_k(k = 0) = 2(t_1 + t_2 + \mu) = 0 \Rightarrow t_2 = -\mu - t_1, \tag{D.14}$$

$$E_k(k = \pi) = 2(-t_1 + t_2 + \mu) = 0 \Rightarrow t_2 = -\mu + t_1, \tag{D.15}$$

Electronic susceptibility reads

$$\Pi(t) = -i\theta(t)\sum_{k,q>0}\langle\left[c_k^\dagger(t)c_k(t) - c_{-k}(t)c_{-k}^\dagger(t), c_q^\dagger(0)c_q(0) - c_{-q}(0)c_{-q}^\dagger(0)\right]\rangle, \tag{D.16}$$

or

$$\Pi(t) = -i\theta(t)\sum_{k,q>0}\langle\left[\tau_z(t), \tau_z(0)\right]\rangle. \tag{D.17}$$

Applying unitary transformation Eq.(D.10) to τ_z, electronic susceptibility becomes

$$\Pi(t) = -i\theta(t)\langle\left[\tau_z(t)\cos(\theta_k) + \tau_y(t)\sin(\theta_k), \tau_z(0)\cos(\theta_k) + \tau_y(0)\sin(\theta_k)\right]\rangle. \tag{D.18}$$

Using Eq.(D.9),

$$\tau_z(t) = \tau_z(0), \tag{D.19}$$

$$\tau_y(t) = e^{iE_k\tau_z t}\tau_y(0)e^{-iE_k\tau_z t} = \cos(2E_k t)\tau_y(0) + \sin(2E_k t)\tau_x(0). \tag{D.20}$$

Then assuming that $\langle\tau_z(0)\rangle = -1$, the electronic susceptibility reads

$$\Pi(t) = -2\theta(t)\sin^2(\theta_k)\sin(2E_k t). \tag{D.21}$$

Performing the Fourier transform, the susceptibility $\Pi(\omega)$ becomes

$$\Pi(\omega) = \sum_{k>0}\sin^2(\theta_k)\left(\frac{1}{\omega - 2E_k + i\eta} - \frac{1}{\omega + 2E_k + i\eta}\right). \tag{D.22}$$

Using Eq.(D.11),

$$\sin^2(\theta_k) = \frac{4(\Delta_1\sin(k) + \Delta_2\sin(2k))^2}{E_k^2}. \tag{D.23}$$

Substituting sum with an integral

$$\sum_{k>0} \Rightarrow \frac{N}{2\pi}\int_0^\pi dk, \tag{D.24}$$

electronic susceptibility reads

$$\Pi(\omega) = \frac{N}{2\pi}\int_0^{\pi} dk \frac{4(\Delta_1 \sin(k) + \Delta_2 \sin(2k))^2}{E_k^2}\left(\frac{1}{\omega - 2E_k + i\eta} - \frac{1}{\omega + 2E_k + i\eta}\right). \tag{D.25}$$

E

SYNTHÈSE EN FRANÇAIS

Dans cette thèse, nous avons étudié la façon dont la mesure du champ micro-ondes de la cavité peut être utilisée pour extraire des informations sur les propriétés des nanostructures couplées à la cavité. Les expériences actuelles permettent de mettre en œuvre des circuits mésoscopiques sur puce couplés à un résonateur à haut facteur de qualité et de mesurer de très petites variations de l'amplitude du signal optique micro-ondes. L'électrodynamique quantique (QED) en cavité est une technique expérimentale qui permet d'étudier et de manipuler des atomes qubits supraconducteurs et des boîtes quantiques couplées à une cavité micro-ondes. En utilisant la théorie des entrées-sorties dans le cas d'un couplage faible entre le système électronique et le champ photonique dans la cavité, nous avons relié le coefficient de transmission de la cavité à la susceptibilité électronique de la nanostructure. Le décalage de fréquence est proportionnel à la partie réelle de la susceptibilité électronique alors que l'élargissement de la fréquence est proportionnel à la partie imaginaire de la susceptibilité. Dans cette thèse, cette approche est appliquée à quatre conducteurs mésoscopiques spécifiques : une jonction tunnel, une boîte quantique couplée aux fils, un fil topologique à une dimension et un anneau supraconducteur.

Tout d'abord, nous utilisons la réponse photonique de la cavité pour étudier une jonction tunnel et une boîte quantique couplée par effet tunnel à des fils métalliques. Nous considérons à la fois le couplage capacitif de la boîte quantique à la cavité ainsi que le couplage des fils à la cavité. Nous démontrons que ces deux types de couplages entraînent une réponse de la cavité totalement différente et donc sondent différentes observables associées au conducteur quantique. Nous trouvons des relations entre les observables optiques, tels que la transmission de la cavité, et les quantités liées au transport, telles que la conductance différentielle $\mathrm{d}I/\mathrm{d}V$. Ces relations sont valables jusqu'à des valeurs élevées de la fréquence et de la tension pour les conducteurs quantiques loin de résonance

(donc dans le régime hors équilibre). Et elles sont valables à basse fréquence et basse tension lorsque la boîte quantique est proche de la résonance. Au-delà de ces régimes, des mesures du champ photonique de la cavité fournissent de nouvelles informations sur le conducteur quantique.

De plus, nous appliquons l'approche de la QED en cavité pour trouver des traces de fermions de Majorana dans les fils topologiques. Nous considérons un supraconducteur en onde p couplé capacitivement à une cavité micro-ondes. Le déphasage et l'élargissement en fréquence dû à la présence du supraconducteur en onde p dans la cavité est proportionnel à la susceptibilité électronique du fil. Les observables photoniques peuvent être utilisées pour obtenir des indices de la présence de fermions de Majorana, comme une transition de phase topologique ou des oscillations de la susceptibilité électronique dans la phase topologique. En outre, des expériences de QED en cavité devraient permettre de sonder la parité de l'état Majorana, qui n'est pas accessible dans les expériences de transport.

Ensuite, nous étudions un fil topologique qui peut accueillir plusieurs fermions de Majorana à ses extrémités en le couplant à une cavité micro-ondes. Cette situation est possible quand il y a des couplages à longue portée dans le fil. On démontre que le champ photonique de la cavité permet de sonder la transition de phase topologique entre les phases avec un nombre différent de fermions de Majorana, ainsi que les oscillations de la susceptibilité. La période des oscillations est différente lorsqu'il y a un ou deux fermions de Majorana à chaque extrémité de la chaîne, alors que ces oscillations sont absentes dans la phase triviale.

Enfin, nous appliquons les méthodes de la QED en cavité pour étudier l'effet Josephson fractionnel associé à la physique des fermions de Majorana. Nous considérons un anneau supraconducteur fermé par un couplage faible, traversé par un flux magnétique constant. Un flux magnétique variable créé par la cavité micro-ondes induit le couplage entre l'anneau et le champ photonique de la cavité. Nous étudions l'effet Josephson et la transition vers l'effet Josephson fractionné, qui est associé à l'apparition de fermions de Majorana dans le système, par l'intermédiaire de la réponse de la cavité. Nous prenons pleinement en compte l'interaction entre les modes de Majorana de faible énergie et les

états de volume gappés. Nous démontrons que ceci est crucial pour le suivi de l'évolution de l'effet Josephson au cours de la transition de la phase topologique vers la phase triviale.

Le cadre théorique proposé dans cette thèse permet de sonder de manière non-intrusive un large éventail de nanostructures, des boîtes quantiques aux supraconducteurs topologiques. En outre, il donne de nouvelles informations sur les propriétés de ces conducteurs quantiques, informations non accessibles via des expériences de transport.

BIBLIOGRAPHY

[1] S. M. Albrecht, A. P. Higginbotham, M. Madsen, F. Kuemmeth, T. S. Jespersen, J. Nygård, P. Krogstrup, and C. M. Marcus. "Exponential protection of zero modes in Majorana islands." In: *Nature* 531.7593 (2016), pp. 206–209.

[2] J. Alicea. "Majorana fermions in a tunable semiconductor device." In: *Physical Review B* 81.12 (2010), p. 125318.

[3] J. Alicea. "New directions in the pursuit of Majorana fermions in solid state systems." In: *Reports on Progress in Physics* 75.7 (2012), p. 076501.

[4] J. Alicea, Y. Oreg, G. Refael, F. von Oppen, and M. P. A. Fisher. "Non-Abelian statistics and topological quantum information processing in 1D wire networks." In: *Nature Physics* 7.5 (2011), pp. 412–417.

[5] D. Bagrets and A. Altland. "Class D spectral peak in Majorana quantum wires." In: *Physical Review Letters* 109.22 (2012), p. 227005.

[6] J. Basset, D.-D. Jarausch, A. Stockklauser, T. Frey, C. Reichl, W. Wegscheider, T. M. Ihn, K. Ensslin, and A. Wallraff. "Single-electron double quantum dot dipole-coupled to a single photonic mode." In: *Physical Review B* 88.12 (2013), p. 125312.

[7] C. W. J. Beenakker. "Random-matrix theory of Majorana fermions and topological superconductors." In: *Reviews of Modern Physics* 87.3 (2015), p. 1037.

[8] G. Ben-Shach, A. Haim, I. Appelbaum, Y. Oreg, A. Yacoby, and B. I. Halperin. "Detecting Majorana modes in one-dimensional wires by charge sensing." In: *Physical Review B* 91.4 (2015), p. 045403.

[9] C. Bergenfeldt and P. Samuelsson. "Microwave quantum optics and electron transport through a metallic dot strongly coupled to a transmission line cavity." In: *Physical Review B* 85.4 (2012), p. 045446.

[10] C. Bergenfeldt and P. Samuelsson. "Nonlocal transport properties of nanoscale conductor–microwave cavity systems." In: *Physical Review B* 87.19 (2013), p. 195427.

[11] A. Blais, R.-S. Huang, A. Wallraff, S. M. Girvin, and R. J. Schoelkopf. "Cavity quantum electrodynamics for superconducting electrical circuits: An architecture for quantum computation." In: *Physical Review A* 69.6 (2004), p. 062320.

[12] Ya. M. Blanter and M. Büttiker. "Shot noise in mesoscopic conductors." In: *Physics Reports* 336.1 (2000), pp. 1–166.

[13] L. E. Bruhat, J. J. Viennot, M. C. Dartiailh, M. M. Desjardins, T. Kontos, and A. Cottet. "Cavity Photons as a Probe for Charge Relaxation Resistance and Photon Emission in a Quantum Dot Coupled to Normal and Superconducting Continua." In: *Physical Review X* 6 (2 2016), p. 021014.

[14] L. E. Bruhat, J. J. Viennot, M. C. Dartiailh, M. M. Desjardins, T. Kontos, and A. Cottet. "Cavity photons as a probe for charge relaxation resistance and photon emission in a quantum dot coupled to normal and superconducting continua." In: *Physical Review X* 6.2 (2016), p. 021014.

[15] M. Büttiker, H. Thomas, and A. Prêtre. "Mesoscopic capacitors." In: *Physics Letters A* 180.4-5 (1993), pp. 364–369.

[16] I. Carusotto and C. Ciuti. "Quantum fluids of light." In: *Reviews of Modern Physics* 85.1 (2013), p. 299.

[17] J. Cayssol, T. Kontos, and G. Montambaux. "Isolated hybrid normal/superconducting ring in a magnetic flux: From persistent current to Josephson current." In: *Physical Review B* 67.18 (2003), p. 184508.

[18] L. Childress, A. S. Sørensen, and M. D. Lukin. "Mesoscopic cavity quantum electrodynamics with quantum dots." In: *Physical Review A* 69.4 (2004), p. 042302.

[19] H. O. H. Churchill, V. Fatemi, K. Grove-Rasmussen, M. T. Deng, P. Caroff, H. Q. Xu, and C. M. Marcus. "Superconductor-nanowire devices from tunneling to the multichannel regime: Zero-bias oscillations and magnetoconductance crossover." In: *Physical Review B* 87.24 (2013), p. 241401.

[20] A. A. Clerk, M. H. Devoret, S. M. Girvin, F. Marquardt, and R. J. Schoelkopf. "Introduction to quantum noise, measurement, and amplification." In: *Reviews of Modern Physics* 82.2 (2010), p. 1155.

[21] L. D. Contreras-Pulido, C. Emary, T. Brandes, and R. Aguado. "Non-equilibrium correlations and entanglement in a semiconductor hybrid circuit-QED system." In: *New Journal of Physics* 15.9 (2013), p. 095008.

[22] A. Cottet, T. Kontos, and B. Douçot. "Squeezing light with Majorana fermions." In: *Physical Review B* 88.19 (2013), p. 195415.

[23] A. Cottet, T. Kontos, and B. Douçot. "Electron-photon coupling in mesoscopic quantum electrodynamics." In: *Physical Review B* 91.20 (2015), p. 205417.

[24] A. Cottet, C. Mora, and T. Kontos. "Mesoscopic admittance of a double quantum dot." In: *Physical Review B* 83.12 (2011), p. 121311.

[25] A. Das, Y. Ronen, Y. Most, Y. Oreg, M. Heiblum, and H. Shtrikman. "Zero-bias peaks and splitting in an Al-InAs nanowire topological superconductor as a signature of Majorana fermions." In: *Nature Physics* 8.12 (2012), pp. 887–895.

[26] B. Dassonneville, M. Ferrier, S. Guéron, and H. Bouchiat. "Dissipation and Supercurrent Fluctuations in a Diffusive Normal-Metal–Superconductor Ring." In: *Physical Review Letters* 110.21 (2013), p. 217001.

[27] R. Deblock, R. Bel, B. Reulet, H. Bouchiat, and D. Mailly. "Diamagnetic orbital response of mesoscopic silver rings." In: *Physical Review Letters* 89.20 (2002), p. 206803.

[28] R. Deblock, Y. Noat, B. Reulet, H. Bouchiat, and D. Mailly. "ac electric and magnetic responses of nonconnected Aharonov-Bohm rings." In: *Physical Review B* 65.7 (2002), p. 075301.

[29] M. R. Delbecq, V. Schmitt, F. D. Parmentier, N. Roch, J. J. Viennot, G. Fève, B. Huard, C. Mora, A. Cottet, and T. Kontos. "Coupling a quantum dot, fermionic leads, and a microwave cavity on a chip." In: *Physical Review Letters* 107.25 (2011), p. 256804.

[30] M. R. Delbecq, L. E. Bruhat, J. J. Viennot, S. Datta, A. Cottet, and T. Kontos. "Photon-mediated interaction between distant quantum dot circuits." In: *Nature Communications* 4 (2013), p. 1400.

[31] G.-W. Deng, L. Henriet, D. Wei, S.-X. Li, H.-O. Li, G. Cao, M. Xiao, G.-C. Guo, M. Schiro, K. Le Hur, et al. "A quantum electrodynamics Kondo circuit: probing orbital and spin entanglement." In: *arXiv preprint arXiv:1509.06141* (2015).

[32] G.-W. Deng, D. Wei, S.-X. Li, J. R. Johansson, W.-C. Kong, H.-O. Li, G. Cao, M. Xiao, G.-C. Guo, F. Nori, et al. "Coupling Two Distant Double Quantum Dots with a Microwave Resonator." In: *Nano letters* 15.10 (2015), pp. 6620–6625.

[33] M. T. Deng, C. L. Yu, G. Y. Huang, M. Larsson, P. Caroff, and H. Q. Xu. "Anomalous zero-bias conductance peak in a Nb–InSb nanowire–Nb hybrid device." In: *Nano letters* 12.12 (2012), pp. 6414–6419.

[34] O. Dmytruk, M. Trif, and P. Simon. "Cavity quantum electrodynamics with mesoscopic topological superconductors." In: *Physical Review B* 92.24 (2015), p. 245432.

[35] O. Dmytruk, M. Trif, and P. Simon. "Josephson effect in topological superconducting rings coupled to a microwave cavity." In: *arXiv preprint arXiv:1604.06780* (2016).

[36] O. Dmytruk, M. Trif, C. Mora, and P. Simon. "Out-of-equilibrium quantum dot coupled to a microwave cavity." In: *Physical Review B* 93.7 (2016), p. 075425.

[37] M. Ferrier, B. Dassonneville, S. Guéron, and H. Bouchiat. "Phase-dependent Andreev spectrum in a diffusive SNS junction: Static and dynamic current response." In: *Physical Review B* 88.17 (2013), p. 174505.

[38] G. Fève, A. Mahe, J.-M. Berroir, T. Kontos, B. Placais, D. C. Glattli, A. Cavanna, B. Etienne, and Y. Jin. "An on-demand coherent single-electron source." In: *Science* 316.5828 (2007), pp. 1169–1172.

[39] M. Filippone, K. Le Hur, and C. Mora. "Giant charge relaxation resistance in the Anderson model." In: *Physical Review Letters* 107.17 (2011), p. 176601.

[40] T. Frey, P. J. Leek, M. Beck, A. Blais, T. Ihn, K. Ensslin, and A. Wallraff. "Dipole coupling of a double quantum dot to a microwave resonator." In: *Physical Review Letters* 108.4 (2012), p. 046807.

[41] T. Frey, P. J. Leek, M. Beck, J. Faist, A. Wallraff, K. Ensslin, T. Ihn, and M. Büttiker. "Quantum dot admittance probed at microwave frequencies with an on-chip resonator." In: *Physical Review B* 86.11 (2012), p. 115303.

[42] L. Fu and C. L. Kane. "Superconducting proximity effect and Majorana fermions at the surface of a topological insulator." In: *Physical Review Letters* 100.9 (2008), p. 096407.

[43] L. Fu and C. L. Kane. "Josephson current and noise at a superconductor/quantum-spin-Hall-insulator/superconductor junction." In: *Physical Review B* 79.16 (2009), p. 161408.

[44] J. Gabelli, G. Fève, J.-M. Berroir, B. Plaçais, A. Cavanna, B. Etienne, Y. Jin, and D. C. Glattli. "Violation of Kirchhoff's laws for a coherent RC circuit." In: *Science* 313.5786 (2006), pp. 499–502.

[45] K. Le Hur, L. Henriet, A. Petrescu, K. Plekhanov, G. Roux, and M. Schiró. "Many-Body Quantum Electrodynamics Networks: Non-Equilibrium Condensed Matter Physics with Light." In: *arXiv preprint arXiv:1505.00167* (2015).

[46] D. A. Ivanov. "Non-Abelian statistics of half-quantum vortices in p-wave superconductors." In: *Physical Review Letters* 86.2 (2001), p. 268.

[47] J. Jang, D. G. Ferguson, V. Vakaryuk, R. Budakian, S. B. Chung, P. M. Goldbart, and Y. Maeno. "Observation of half-height magnetization steps in Sr2RuO4." In: *Science* 331.6014 (2011), pp. 186–188.

[48] T. Karzig, C.-E. Bardyn, N. H. Lindner, and G. Refael. "Topological polaritons." In: *Physical Review X* 5.3 (2015), p. 031001.

[49] A. Yu. Kitaev. "Unpaired Majorana fermions in quantum wires." In: *Physics-Uspekhi* 44.10S (2001), p. 131.

[50] H.-J. Kwon, K. Sengupta, and V. M. Yakovenko. "Fractional ac Josephson effect in p-and d-wave superconductors." In: *The European Physical Journal B-Condensed Matter and Complex Systems* 37.3 (2004), pp. 349–361.

[51] N. Lambert, C. Flindt, and F. Nori. "Photon-mediated electron transport in hybrid circuit-QED." In: *EPL (Europhysics Letters)* 103.1 (2013), p. 17005.

[52] E. J. H. Lee, X. Jiang, R. Aguado, G. Katsaros, C. M. Lieber, and S. De Franceschi. "Zero-bias anomaly in a nanowire quantum dot coupled to superconductors." In: *Physical Review Letters* 109.18 (2012), p. 186802.

[53] M. Lee, R. López, M.-S. Choi, T. Jonckheere, and T. Martin. "Effect of many-body correlations on mesoscopic charge relaxation." In: *Physical Review B* 83.20 (2011), p. 201304.

[54] D. Leibfried, R. Blatt, C. Monroe, and D. Wineland. "Quantum dynamics of single trapped ions." In: *Reviews of Modern Physics* 75.1 (2003), p. 281.

[55] L. Li, C. Yang, and S. Chen. "Winding numbers of phase transition points for one-dimensional topological systems." In: *EPL (Europhysics Letters)* 112.1 (2015), p. 10004.

[56] N. H. Lindner, G. Refael, and V. Galitski. "Floquet topological insulator in semiconductor quantum wells." In: *Nature Physics* 7.6 (2011), pp. 490–495.

[57] J. Liu, A. C. Potter, K. T. Law, and P. A. Lee. "Zero-bias peaks in the tunneling conductance of spin-orbit-coupled superconducting wires with and without Majorana end-states." In: *Physical Review Letters* 109.26 (2012), p. 267002.

[58] D. Loss and D. P. DiVincenzo. "Quantum computation with quantum dots." In: *Physical Review A* 57.1 (1998), p. 120.

[59] R. M. Lutchyn, J. D. Sau, and S. Das Sarma. "Majorana fermions and a topological phase transition in semiconductor-superconductor heterostructures." In: *Physical Review Letters* 105.7 (2010), p. 077001.

[60] E. Majorana. "Teoria simmetrica dell'elettrone e del positrone." In: *Il Nuovo Cimento (1924-1942)* 14.4 (1937), pp. 171–184.

[61] U. C. Mendes and C. Mora. "Cavity squeezing by a quantum conductor." In: *New Journal of Physics* 17.11 (2015), p. 113014.

[62] U. C. Mendes and C. Mora. "Electron-photon interaction in a quantum point contact coupled to a microwave resonator." In: *Physical Review B* 93 (23 2016), p. 235450.

[63] C. Mora and K. Le Hur. "Universal resistances of the quantum resistance-capacitance circuit." In: *Nature Physics* 6.9 (2010), pp. 697–701.

[64] V. Mourik, K. Zuo, S. M. Frolov, S. R. Plissard, E. P. A. M. Bakkers, and L. P. Kouwenhoven. "Signatures of Majorana fermions in hybrid superconductor-semiconductor nanowire devices." In: *Science* 336.6084 (2012), pp. 1003–1007.

[65] C. Müller, J. Bourassa, and A. Blais. "Detection and manipulation of Majorana fermions in circuit QED." In: *Physical Review B* 88.23 (2013), p. 235401.

[66] S. Nadj-Perge, I. K. Drozdov, J. Li, H. Chen, S. Jeon, J. Seo, A. H. MacDonald, B. A. Bernevig, and A. Yazdani. "Observation of Majorana fermions in ferromagnetic atomic chains on a superconductor." In: *Science* 346.6209 (2014), pp. 602–607.

[67] S. E. Nigg, R. López, and M. Büttiker. "Mesoscopic charge relaxation." In: *Physical review letters* 97.20 (2006), p. 206804.

[68] Y. Niu, S. B. Chung, C.-H. Hsu, I. Mandal, S. Raghu, and S. Chakravarty. "Majorana zero modes in a quantum Ising chain with longer-ranged interactions." In: *Physical Review B* 85.3 (2012), p. 035110.

[69] C. Ohm and F. Hassler. "Majorana fermions coupled to electromagnetic radiation." In: *New Journal of Physics* 16.1 (2014), p. 015009.

[70] C. Ohm and F. Hassler. "Microwave readout of Majorana qubits." In: *Physical Review B* 91.8 (2015), p. 085406.

[71] Y. Oreg, G. Refael, and F. von Oppen. "Helical liquids and Majorana bound states in quantum wires." In: *Physical Review Letters* 105.17 (2010), p. 177002.

[72] K. D. Petersson, L. W. McFaul, M. D. Schroer, M. Jung, J. M. Taylor, A. A. Houck, and J. R. Petta. "Circuit quantum electrodynamics with a spin qubit." In: *Nature* 490.7420 (2012), pp. 380–383.

[73] F. Pientka, L. Jiang, D. Pekker, J. Alicea, G. Refael, Y. Oreg, and F. von Oppen. "Magneto-Josephson effects and Majorana bound states in quantum wires." In: *New Journal of Physics* 15.11 (2013), p. 115001.

[74] F. Pientka, A. Romito, M. Duckheim, Y. Oreg, and F. von Oppen. "Signatures of topological phase transitions in mesoscopic superconducting rings." In: *New Journal of Physics* 15.2 (2013), p. 025001.

[75] D. I. Pikulin, J. P. Dahlhaus, M. Wimmer, H. Schomerus, and C. W. J. Beenakker. "A zero-voltage conductance peak from weak antilocalization in a Majorana nanowire." In: *New Journal of Physics* 14.12 (2012), p. 125011.

[76] J. D. Pillet, C. H. L. Quay, P. Morfin, C. Bena, A. L. Yeyati, and P. Joyez. "Andreev bound states in supercurrent-carrying carbon nanotubes revealed." In: *Nature Physics* 6.12 (2010), pp. 965–969.

[77] E. Prada, P. San-Jose, and R. Aguado. "Transport spectroscopy of N S nanowire junctions with Majorana fermions." In: *Physical Review B* 86.18 (2012), p. 180503.

[78] J.-M. Raimond, M. Brune, and S. Haroche. "Manipulating quantum entanglement with atoms and photons in a cavity." In: *Reviews of Modern Physics* 73.3 (2001), p. 565.

[79] D. Rainis, L. Trifunovic, J. Klinovaja, and D. Loss. "Towards a realistic transport modeling in a superconducting nanowire with Majorana fermions." In: *Physical Review B* 87.2 (2013), p. 024515.

[80] B. Reulet, M. Ramin, H. Bouchiat, and D. Mailly. "Dynamic response of isolated aharonov-bohm rings coupled to an electromagnetic resonator." In: *Physical Review Letters* 75.1 (1995), p. 124.

[81] L. P. Rokhinson, X. Liu, and J. K. Furdyna. "The fractional ac Josephson effect in a semiconductor-superconductor nanowire as a signature of Majorana particles." In: *Nature Physics* 8.11 (2012), pp. 795–799.

[82] E. A. Rothstein, O. Entin-Wohlman, and A. Aharony. "Noise spectra of a biased quantum dot." In: *Physical Review B* 79.7 (2009), p. 075307.

[83] I. Safi and P. Joyez. "Time-dependent theory of nonlinear response and current fluctuations." In: *Physical Review B* 84.20 (2011), p. 205129.

[84] N. Samkharadze, A. Bruno, P. Scarlino, G. Zheng, D. P. DiVincenzo, L. DiCarlo, and L. M. K. Vandersypen. "High-Kinetic-Inductance Superconducting Nanowire Resonators for Circuit QED in a Magnetic Field." In: *Physical Review Applied* 5.4 (2016), p. 044004.

[85] S. Das Sarma, J. D. Sau, and T. D. Stanescu. "Splitting of the zero-bias conductance peak as smoking gun evidence for the existence of the Majorana mode in a superconductor-semiconductor nanowire." In: *Physical Review B* 86.22 (2012), p. 220506.

[86] J. D. Sau, R. M. Lutchyn, S. Tewari, and S. Das Sarma. "Generic new platform for topological quantum computation using semiconductor heterostructures." In: *Physical Review Letters* 104.4 (2010), p. 040502.

[87] M. Schiró and K. Le Hur. "Tunable hybrid quantum electrodynamics from nonlinear electron transport." In: *Physical Review B* 89.19 (2014), p. 195127.

[88] T. L. Schmidt, A. Nunnenkamp, and C. Bruder. "Majorana qubit rotations in microwave cavities." In: *Physical Review Letters* 110.10 (2013), p. 107006.

[89] T. L. Schmidt, A. Nunnenkamp, and C. Bruder. "Microwave-controlled coupling of Majorana bound states." In: *New Journal of Physics* 15.2 (2013), p. 025043.

[90] M. D. Schroer, M. Jung, K. D. Petersson, and J. R. Petta. "Radio frequency charge parity meter." In: *Physical Review Letters* 109.16 (2012), p. 166804.

[91] D. Sticlet, C. Bena, and P. Simon. "Josephson effect in superconducting wires supporting multiple Majorana edge states." In: *Physical Review B* 87.10 (2013), p. 104509.

[92] D. Sticlet and J. Cayssol. "Dynamical response of dissipative helical edge states." In: *Physical Review B* 90.20 (2014), p. 201303.

[93] A. Stockklauser, V. F. Maisi, J. Basset, K. Cujia, C. Reichl, W. Wegscheider, T. Ihn, A. Wallraff, and K. Ensslin. "Microwave Emission from Hybridized States in a Semiconductor Charge Qubit." In: *Physical Review Letters* 115.4 (2015), p. 046802.

[94] E. M. Stoudenmire, J. Alicea, O. A. Starykh, and M. P. A. Fisher. "Interaction effects in topological superconducting wires supporting Majorana fermions." In: *Physical Review B* 84.1 (2011), p. 014503.

[95] H. Toida, T. Nakajima, and S. Komiyama. "Vacuum Rabi splitting in a semiconductor circuit QED system." In: *Physical Review Letters* 110.6 (2013), p. 066802.

[96] M. Trif and Ya. Tserkovnyak. "Resonantly tunable majorana polariton in a microwave cavity." In: *Physical Review Letters* 109.25 (2012), p. 257002.

[97] N. Trivedi and D. A. Browne. "Mesoscopic ring in a magnetic field: Reactive and dissipative response." In: *Physical Review B* 38.14 (1988), p. 9581.

[98] J. I. Väyrynen, G. Rastelli, W. Belzig, and L. I. Glazman. "Microwave signatures of Majorana states in a topological Josephson junction." In: *Physical Review B* 92.13 (2015), p. 134508.

[99] J. J. Viennot, M. C. Dartiailh, A. Cottet, and T. Kontos. "Coherent coupling of a single spin to microwave cavity photons." In: *Science* 349.6246 (2015), pp. 408–411.

[100] R. Wakatsuki, M. Ezawa, Y. Tanaka, and N. Nagaosa. "Fermion fractionalization to Majorana fermions in a dimerized Kitaev superconductor." In: *Physical Review B* 90.1 (2014), p. 014505.

[101] A. Wallraff, D. I. Schuster, A. Blais, L. Frunzio, R.-S. Huang, J. Majer, S. Kumar, S. M. Girvin, and R. J. Schoelkopf. "Strong coupling of a single photon to a superconducting qubit using circuit quantum electrodynamics." In: *Nature* 431.7005 (2004), pp. 162–167.

[102] K. Wang, C. Payette, Y. Dovzhenko, P. W. Deelman, and J. R. Petta. "Charge relaxation in a single-electron Si/SiGe double quantum dot." In: *Physical Review Letters* 111.4 (2013), p. 046801.

[103] J. Wiedenmann, E. Bocquillon, R. S. Deacon, S. Hartinger, O. Herrmann, T. M. Klapwijk, L. Maier, C. Ames, C. Brüne, C. Gould, et al. "4 [pi]-periodic Josephson supercurrent in HgTe-based topological Josephson junctions." In: *Nature Communications* 7 (2016).

[104] F. Wilczek. "Majorana returns." In: *Nature Physics* 5.9 (2009), pp. 614–618.

[105] K. Yavilberg, E. Ginossar, and E. Grosfeld. "Fermion parity measurement and control in Majorana circuit quantum electrodynamics." In: *Physical Review B* 92.7 (2015), p. 075143.

[106] A. A. Zyuzin, D. Rainis, J. Klinovaja, and D. Loss. "Correlations between Majorana fermions through a superconductor." In: *Physical Review Letters* 111.5 (2013), p. 056802.